

CALIBRATING SLOPE-DEPENDENT ERRORS IN PROFILOMETRY

by

Yue Zhou

A dissertation submitted to the faculty of  
The University of North Carolina at Charlotte  
in partial fulfillment of the requirements  
for the degree of Doctor of Philosophy in  
Optical Science and Engineering

Charlotte

2014

Approved by:

---

Dr. Angela Davies

---

Dr. Faramamarz Farahi

---

Dr. Christopher J. Evans

---

Dr. Edward Morse

---

Dr. Greg Gbur

---

Dr. Todd Steck



## ABSTRACT

YUE ZHOU. Calibrating slope-dependent errors in profilometry.  
(Under the direction of DR. ANGELA DAVIES)

Optical profilometers, such as scanning white light interferometers and confocal microscopes, provide high resolution measurements and are widely utilized in many fields for measuring surface topography. The techniques are capable of high-speed surface measurements with nanometer-scale repeatability, and are used in industries such as data storage, automotive, MEMS, electronics, micro-optics, and bio-medical, to name a few. The instrument works best on flat, stepped structures, and slope-dependent systematic errors can be present in the measurement of steep sloped regions. These errors can be the same order of magnitude as features on the surface to be measured. Researchers have carried out many studies of these errors from first principle analyses; however the errors depend on proprietary details of the optical design and cannot be exactly calculated from first principles. The problem is further complicated by a lack of calibration artifacts to measure the errors directly. We propose a self-calibration technique, the random ball test, for calibrating slope-dependent errors of such instruments. A simulation study validates the approach and shows that the random ball test is effective in practical limits. We demonstrate the calibration on a 50x confocal microscope and a 50x white light interferometer with a specific chosen algorithm, find a surface slope-dependent bias that increases monotonically with the magnitude of the surface slope. The uncertainty of the calibration is smaller than the observed measurement bias and is dominated by residual random noise. Effects such as distortion, drift and ball radius

uncertainty were investigated to understand their contribution to the calibration uncertainty.

## ACKNOWLEDGEMENTS

I am very thankful for all the help and dedication provided by my advisor Dr. Angela Davies. You have offered me a great opportunity to work on the research project of optical profilometry. Along the way, you gave me tremendous help and patience on numerous technical challenges. You also provide me very important career advice, support me in all aspects while I am working at Corning. Angela, your wisdom and personality have very import influence on me. I truly enjoy working at Optical Metrology Group. In addition, I would like to thank for University of North Carolina at Charlotte, the Department of Physics and Optical Science, the Center for Precision Metrology (CPM). I am also thankful for the funding provided by affiliates of CPM. I must acknowledge the calibration advice provided by Dr. Chris Evans, index matching advice from Dr. Faramarz Farahi, ball radius measurement help by Greg Caskey. Thank you also to the members of my labmates, Yue Dong, Benrui Zheng, Ali Pouya Fard, and Michael Uwakwe, I enjoyed the brainstorming with everyone. Special thanks to Corning and Charles Stroup for offering me an opportunity to work on optical metrology extensively. Lastly, I am especially grateful to my wife, family and my parents for their constant support and encouragement. To my daughter, Emma, I am infinitely thankful for the joy and happiness that you bring to my life.

## TABLE OF CONTENTS

LIST OF ABBREVIATIONS	viii
CHAPTER 1: INTRODUCTION	1
1.1 Project Motivation	1
1.2 Theory of Proposed Solution	6
1.3 Dissertation Outline	8
1.4 Surface Metrology Techniques	8
1.5 Self Calibration	14
CHAPTER 2: OVERVIEW OF OPTICAL PROFILOMETRY	16
2.1 Surface Texture	16
2.2 Scanning White Light Interferometer (SWLI)	18
2.2.1 Introduction of SWLI	18
2.2.2 Signal Processing of The White Light Interferogram	22
2.2.3 Systematic Bias of SWLI	28
2.3 Laser Scanning Confocal Microscopy (LSCM)	31
CHAPTER 3: RANDOM BALL TEST (RBT) SIMULATION FOR OPTICAL PROFILER	35
3.1 Simulate A RBT For Profiler Calibration	35
3.1.1 Realistic Ball Generation	38
3.1.2 Random Rotations	40
3.1.3 Robust Best Fit Sphere Algorithm	41

3.1.4 Simulation Speed Improvement	43
3.2 Ball Error Distribution Study	44
3.3 Number of Rotations Study	47
3.4 Ball Positioning Study	50
3.5 Distortion Effect Study	53
3.5.1 Distortion Detection	56
3.5.2 Distortion Effect On RBT	60
3.6 Drift Effect Study	67
CHAPTER 4: RBT EXPERIMENTAL RESULTS	70
4.1 Setup for the Calibration	70
4.2 Ball Radius Measurement	71
4.3 Calibration For Confocal Using RBT	72
4.3.1 Calibration Results For The LSCM	73
4.3.2 Uncertainty Analysis	83
4.3.3 RBT With Different Ball Sizes	99
4.4 Calibration of The SWLI Using The RBT	102
CHAPTER 5: CONCLUSION	108
REFERENCES	112
APPENDIX A: MATLAB CODE FOR RBT SIMULATION	119
APPENDIX B: MATLAB CODE FOR DATA PROCESSING OF RBT CALIBRATION	125

## LIST OF ABBREVIATIONS

RBT	random ball test
PSI	phase shift interferometer
SWLI	scanning white light interferometer
LSCM	laser scanning confocal microscopy
CMM	coordinate measuring machine
SPM	scanning probe microscopy
AFM	atomic force microscopy
SEM	scanning electron microscopy
NA	numerical aperture
FoV	field of view
PV	peak to valley
RMS	root mean square
PSD	power spectrum density
PZT	piezoelectric transducer
MEMS	micro-electro-mechanical systems
AU	airy-disk unit



## CHAPTER 1: INTRODUCTION

### 1.1 Project Motivation

Optical profilometry plays a vital role in surface metrology [1, 2]. Compared with stylus profilometry, which detects the surface profile through the deflection of mechanical stylus, an optical method has its own advantages, such as a noncontact and therefore nondestructive measuring process and a faster surface topography acquisition rate. Two popular instruments based on optical techniques are the scanning white light interferometer (SWLI) and the laser scanning confocal microscope (LSCM). Both are capable of measuring surface topography at the nanometer or even sub-nanometer scale in the height direction.

While very repeatable, these tools often add a systematic error to the measurement that can be the same order of magnitude as features to be measured. The so-called “batwing effect” is a well-known example. It is a measurement artifact (error or bias) that appears at step-edges in SWLI [3]. Thus, calibration of the instrument becomes critical. Instruments are usually calibrated with step height standards and this works well for measurements of terraced, binary or nearly flat surfaces. But many surfaces have appreciable continuous slope variation, slopes reaching the measurement limitation of the instrument. The typical calibration with a step height standard will not capture potential slope-dependent biases. And given the basic operating physical principle of such instruments, slope-dependent errors are expected [4]. For surfaces with continuous slope

variation, slope-dependent errors are not obvious. High quality calibration artifacts are not readily available to quantify and correct these errors, thus, there is a strong need for a rigorous and convenient calibration method.

Many studies have been done on the slope dependent bias in SWLI optical profilometers from a first principle analysis perspective. For example, Mykura and Rhead [5] in 1963 experimentally measured that the fringe spacing, as well as fringe contrast, of an interference microscope with monochromatic illumination decreases as the object tilt angle increases. Dowell et al. [6] later approximated the numerical aperture (NA) change with a tilted flat object, as shown in figure 1. The effective numerical aperture  $NA_{eff}$  is calculated as

$$NA_{eff} = \sin(\alpha_0 - \theta) = \sin \alpha , \quad (1.1)$$

where  $\theta$  is the tilt angle and  $\alpha_0$  is the half cone angle of the numerical aperture of the objective.

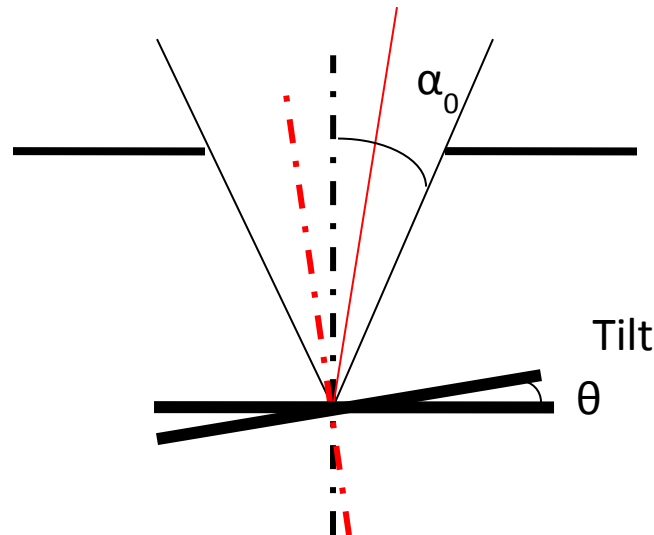


Figure 1: Effective numerical aperture change for a tilted flat surface.

There are various theories that describe the phenomenon of effective NA change [7-10]. However, the effective NA is very difficult to determine in practice from first principles because of the impact of several factors, such as variations in the local slope of the test surface, the coherence of the source, and variations in illumination of the aperture. Creath [11] experimentally calibrated the effective NA whose nominal NA ranges from 0.1 to 0.95, and confirmed the scaling factor relationship between the two proposed by Ingelstam and Lohmann [8]. Whereas, later on Schulz [12] found that this scaling factor relationship only works well for low NA. For a high NA, there is a more complicated relationship between nominal and effective NA.

Besides the effective NA, several other factors in SWLI were also studied from first principles to explore slope dependent systematic bias. Schmit [13] found that the effective wavelength of illumination light becomes smaller with tilt for SWLI. Further, a larger spectral bandwidth of the illumination source will cause a larger effective wavelength with tilt, as shown in figure 2. Pfürtner and Schwider [14] proposed that dispersion is the cause for the bias - when the paths of interferometer's two arms in glass are not equal within the field of view, tilt-dependent dispersion is often the cause of  $2\pi$  errors in SWLI measurements. Many more slope dependent error correction methods based on first principle analyses have been investigated [3, 15-19].

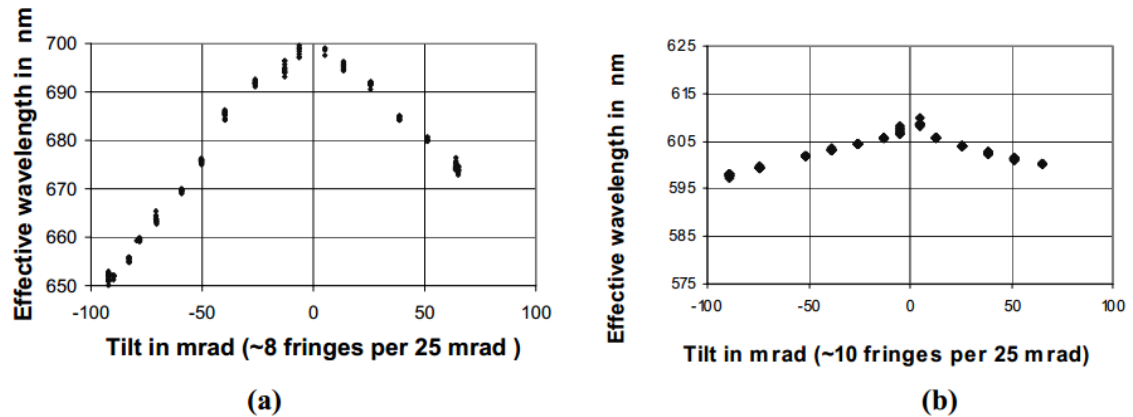


Figure 2: Effective wavelength change in 50x, NA = 0.55, objective with tilt with two different spectral bandwidth illumination conditions: a) 300nm bandwidth; b) 80nm bandwidth.

In general, the slope-dependent error depends on the location in the field of view, the local surface slope, and the configuration of the instrument. The magnitude depends on proprietary details of the optical design and therefore cannot be calculated from first principles for every case. So, a methodology is needed whereby these errors can be directly measured, characterized and mapped out using a self-calibration strategy that avoids the need for a first principle calculation. This dissertation proposes and demonstrates a method to experimentally measure the bias and a means of incorporating this information into the data analysis for error compensation.

Error compensation includes two steps, a calibration step and a correction step. Deck and Evans [20] used this idea to calibrate a SWLI by using a reference flat at a large number of tilt orientations and fitting the surface deviations to low order Zernike polynomials. However, this approach which uses a large reference flat will not work for calibrating errors over the full measurable slope range for high magnification objectives. This is because the working distance is small for these objectives and tilting a large flat over the full measurable slope range is not mechanically feasible, e.g. the Olympus

LEXT 4000 LSCM's 50X objective has a working distance of 0.35mm and measurable slope range up to 85 degrees [21].

Recently, Leach et al. [22, 23] proposed a way for characterizing the point spread function and transfer function of a SWLI that can be used to estimate slope-dependent errors. The method uses a spherical reference artifact whose radius of curvature is comparable to the field of view, the measurement of which yields information about the optical transfer function. The authors point out that the method requires knowledge of the form of the artifact and this is a limitation. The method proposed here exploits averaging to ease the requirements on needed information about the artifact, and it is applicable to all profilometry-based measurements (SWLI or otherwise). But, our method does not yield a calibration of the complete optical transfer function. It is an important complement, providing direct characterization of the slope-dependent errors in the low-spatial frequency limit where the instrument transfer function is typically close to flat with a value of one [24].

In mechanical profilometry, a razor blade with a sharp edge is often used as an artifact to estimate the radius of curvature of the stylus [25]. Spherical artifacts can also be used to measure the stylus size by measuring the wavefront difference between reference and object in an interferometry setup. They have not been used with an averaging approach as proposed here to eliminate the contribution of the form errors on the ball and specifically to evaluate slope-dependent errors.

This dissertation discusses the application of the random ball test (RBT) for slope-dependent error calibration. The process can be viewed as simulating the measurement of a perfect spherical artifact with a known (independently measured) radius. The height

scale in these instruments is calibrated with a step height standard, so errors observed with the RBT, departure from the correct perfect sphere, are *not* due to an error in the z calibration - rather errors are the result of a slope-dependent bias that is not captured by the step-height standard calibration. In this way, this technique is capturing slope-dependent errors - a ball has a natural range of slopes over the field of view.

## 1.2 Theory of Proposed Solution

The RBT has been proposed and validated for calibrating biases in phase shifting interferometry (PSI) by Parks and Evans et al. [26]. By measuring a collection of random patches on the surface of a ball and then averaging, ball imperfections are averaged out, leaving only the systematic biases from the instrument. For example, each measurement of a ball profile  $W_i$  is a combination of ball error and the systematic error from the instrument, given by

$$W_i = W_{ballerror} + \epsilon_{bias}, \quad (1.2)$$

where  $W_{ballerror}$  is the form error of the measured patch and  $\epsilon_{bias}$  represents the bias from the system itself. By measuring a collection of random patches and averaging, the ball imperfections will be averaged out as follows [27],

$$\frac{\sum W_i}{N} = \frac{\sum W_{ballerror}}{N} + \frac{\sum \epsilon_{bias}}{N}, \quad (1.3)$$

where  $N$  is the number of measurements. The uncertainty decreases as the inverse of the square root of the number of patches averaged, given by [28]:

$$u = \frac{\epsilon_{bias}}{\sqrt{N}}. \quad (1.4)$$

Therefore, the systematic bias can be estimated and then used to compensate future measurements. As shown in figure 3, the RBT can be viewed as though an instrument is measuring a perfect ball patch, thereby providing a direct characterization of the slope-dependent errors in the low-spatial frequency limit where the instrument transfer function is typically close to flat with a value of one [24].

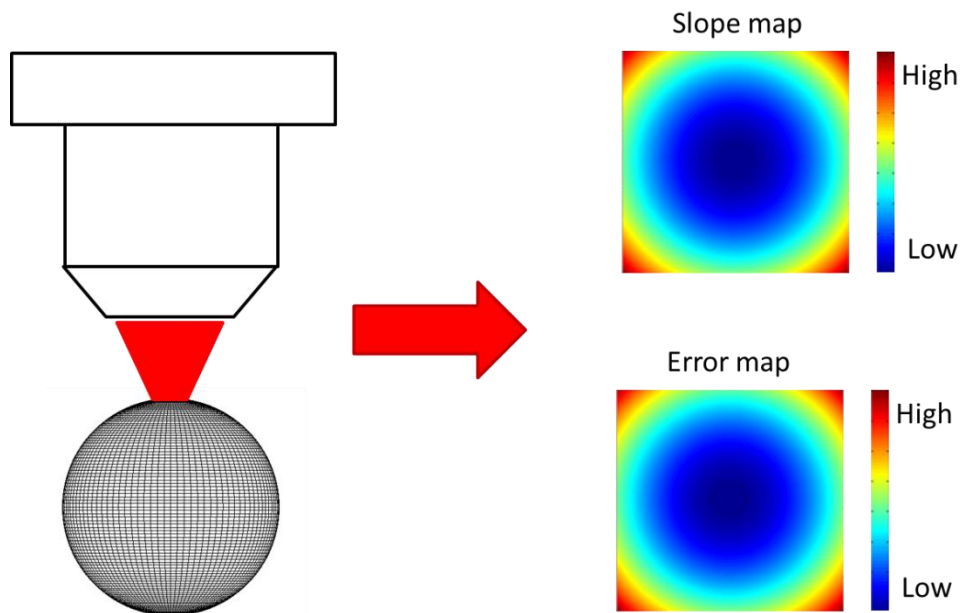


Figure 3: Steps of a RBT calibration: By averaging out ball errors, a perfect ball is assumed to be measured(left); Slope map over a ball patch is calculated(upper right); Systematic error map is obtained by subtracting a perfect ball patch(lower right).

The major difference between profilometry and PSI calibration is that the curvature should be removed in the PSI application since curvature (power) is tied to misalignment and therefore not uniquely measurable. Thus, PSI measurements focus on the departure from a sphere. However, surface curvature over the field of view may be an important geometry to capture in profilometry. The need and ability to retain the curvature in the RBT applied to profilometry deserves careful consideration. Moreover, several

uncertainties during calibration have a direct impact on the accuracy of calibration result, detailed study for each factor is needed.

### 1.3 Dissertation Outline

The remainder of Chapter 1 provides an overview of different optical metrology techniques that are used for measuring surface topography. The pros and cons of each are discussed and compared. Self-calibration is introduced at the end of Chapter 1, which is an important aspect of our proposed calibration method. Chapter 2 provides a more detailed overview of two common types of optical profilometers: the scanning white light interferometer (SWLI) and the laser scanning confocal microscope (LSCM). The configuration, working principle, capabilities and the potential measurement errors for each are discussed, respectively. This provides insight into the potential causes of slope-dependent errors in these instruments.

We have simulated our proposed calibration measurement in detail and used simulation to explore uncertainty contributions. These studies are presented in Chapter 3. We demonstrate the calibration process on two optical profilometers, a SWLI and a LSCM available through research centers on campus. The first half part of Chapter 4 discusses the calibration results of the LSCM available through the Center for Optoelectronics and Optical Communications, and the second part of Chapter 4 discusses the results for the SWLI available through the Center for Precision Metrology. The uncertainty sources that contribute to the calibration are discussed extensively for the LSCM calibration process. We describe practical ways for assessing the calibration uncertainty due to factors such as imaging distortion, stage drift, and ball radius uncertainty.



In the final chapter, Chapter 5, we conclude with a summary of the major achievements of this project and summarize the suggested procedure for an effective calibration for any optical profilometer.

The document also contains appendixes for all the Matlab<sup>TM</sup> source code used to simulate optical profilometer calibration by using the RBT and the way to process measurement data from the instruments.

#### 1.4 Surface Metrology Techniques

Surface texture has been recognized as an important factor in determining the functionality and performance of the workpiece [29]. A number of methods have been developed for line profiling and areal topography. As shown in table 1, these methods can be classified into two categories: contact and non-contact.

Table 1: Surface metrology techniques summary.

Category	Techniques	Merits	Limitation
<b>Contact</b>	Stylus profilometry (e.g. CMM)	Large range (XYZ)	Tip geometry
	SPM(e.g. AFM)	High resolution	Slow, tip geometry, potential surface damage
<b>Non-contact</b>	Interferometry	Fast ,high vertical resolution	Limited lateral resolution, limited slope range
	Confocal	High aspect ratio structures Max. detectable slope up to 85°	Limited lateral resolution, systematic bias for large sloped surface
	Photogrammetry	Low cost, fast	Limited capability for resolution
	Deflectometry	Fast, capable to measure specular surface	Limited capability for transparent samples
	SEM	nm resolution	Vacuum required, potential for sample charging

In the contact category, stylus profilometry is a mechanical measuring technique to measure surface topography by drawing a stylus over the surface at a constant speed, and an electric signal of displacement is produced by the transducer. Stylus profilometry often can cover a vertical scan range up to several millimeters. Compared to optical surface metrology measurements, it is more independent of the non-geometrical properties of the surface, thus stylus profilometry is widely used in industrial applications [30]. The spatial resolution of such instruments is typically constrained by the diamond tip geometry, generally it ranges from 2  $\mu\text{m}$  to 20  $\mu\text{m}$  [31]. Due to its mechanical contact nature, this method cannot be used for measurements of delicate

surfaces [32]. Another technique in this category is atomic force microscopy (AFM), a contact version of the general category of scanning probe microscopy (SPM). As shown in figure 4, a probe with radius of curvature on the order of 10s – 100s of nanometers is used to scan across the specimen, a reflected optical signal is captured by the detector, providing feedback on the probe location. Atomic force microscopy is capable of sub-nm topography data acquisition, reaching nm lateral resolution. However, in addition to the contact nature of the measurement, limited scanning speed and measurement area size are two additional disadvantages.

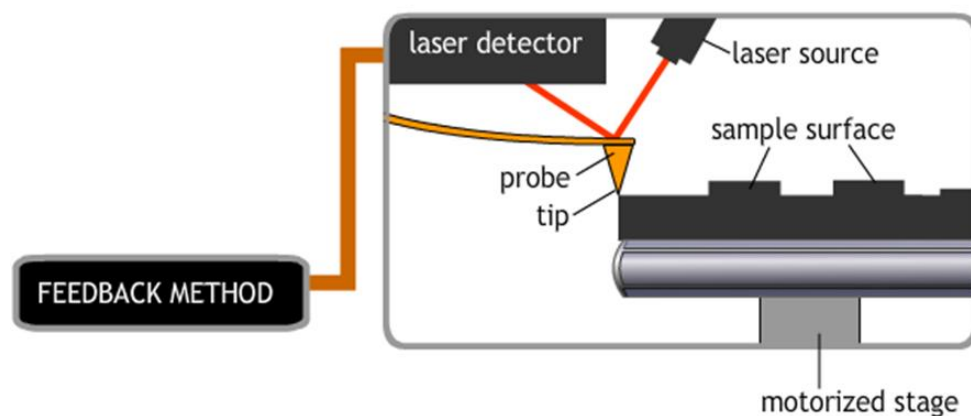


Figure 4: Schematic of atomic force microscopy (AFM) [33].

In contrast, many techniques fall onto the non-contact category and most of them are optical methods. Because of the absence of surface damage and the parallel nature of the measurement process (fast measurement times), non-contact surface metrology techniques have been widely used in many fields. For example, interferometry and confocal microscopy are often used for micro optics, biological sample, and semiconductor sample characterization because the measurements do not scratch the

delicate surfaces and provide high resolution images at the same time. Photogrammetry and deflectometry are two techniques that are capable of quickly measuring large scale parts. As shown in figure 5 (left), a typical photogrammetry system consists of two or more cameras for taking object images from different locations, and the positions of points of interest on the object are calculated via geometrical triangulation. A deflectometry setup is shown on the right of figure 5, where a camera captures the reflected image of a pattern after reflection from a surface to be measured. The topography of the surface gives rise to distortion of the observed pattern, thus a measurement of the pattern distortion contains the information about the height profile of the surface [34]. There are some other methods for surface metrology, such as digital holography which is still an active research area where 3D information of an object can be reconstructed by recorded hologram [35]. Scanning electron microscopy (SEM) is a powerful 2D structure imaging tool. The third dimension information can be realized by incorporating the ideas of photogrammetry and triangulation from stereo pairs or triplets of SEM image scans [31, 36].

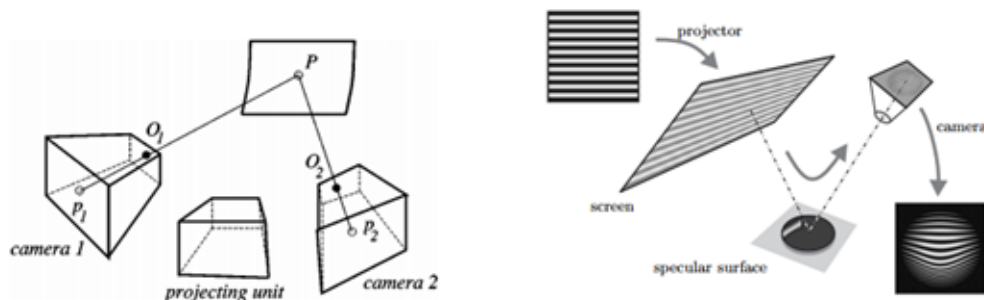


Figure 5: Schematic setup of photogrammetry [37] (left) and deflectometry [38] (right).

There are also disadvantages of optical-related surface metrology techniques. Normally they have limited lateral resolution due to diffraction and imaging resolution limits, such as in interferometry. Moreover, as mentioned before, optical measurements can depend on the geometrical and optical properties of the surface. For example, a sloped or rough surface leads to a different reflected optical signal than a smooth and/or flat surface, thus the measurement may behave differently with these surface characteristics and systematic biases in the measurement can result. As shown in figure 6, a flat surface with tilt angle,  $\alpha$ , has a reflection cone that is changed from the solid red lines to the dash red lines. The reduced signal (reflected light filling the hashed region in the figure) will lead to errors in the height calculation for that local area. The detailed description of this slope-dependent systematic bias will be discussed in a subsequent chapter.

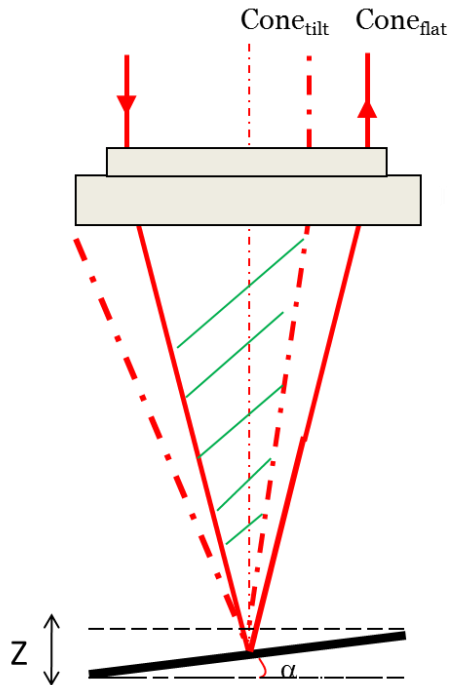


Figure 6: Schematic of how a tilted surface causes a change in the reflection signal.

### 1.5 Self Calibration

In surface metrology, it is often the case that systematic bias can be the same order of magnitude as features on the surface to be measured. Unlike random noise which could be eliminated by averaging, systematic error is a repeatable quantity associated with every single measurand. Thus calibration for this type of bias becomes critical. A high quality artifact is often deployed to estimate or calibrate systematic error. For example, a step height standard is common to see for optical profilometer calibration. Cross-hair is often used for calibrating system drift. However, in some cases a high quality artifact is just not available. An alternative technique for accomplishing this task is self-calibration.

Self calibration is not new to surface metrology, Evans et al.[39] listed self calibration techniques into four categories: reversal, redundancy, error separation, and absolute testing. Two famous examples are three flat test and the random ball test. The three flat

test is used to separate the error of a reference flat from the error in the wavefront reflected by a test flat in a Fizeau interferometer [40]. The random ball test (RBT) is a self-calibration method to estimate the error contribution from the transmission sphere of a phase shift interferometer. The principle is to measure a collection of random patches on the surface of a ball with the interferometer, then average all the measurements. The ball imperfections average out, approximately leaving only the systematic biases from the instrument.

## CHAPTER 2: OVERVIEW OF OPTICAL PROFILOMETRY

### 2.1 Surface Texture

As the technology shifts from macro to micro-nano scale, surface topography plays a more important role due to its impacts on the functionality of the work piece. Surface texture describes the geometric attributes of a surface. It is standardized and widely accepted by industries. ISO 10110 states that “surface texture is the characteristic of a surface that can be effectively described with statistical methods” [41]. Based on the spatial frequency regimes, surface texture consists of three elements, as shown in figure 7: roughness, waviness and form (also called “figure” in some cases).

Roughness has the highest spatial frequencies and can be captured by applying a high pass filter to the surface profile. The wavelength of roughness is usually in the submicron range, and it often appears as the process mark of the surface fabrication procedure. If the surface is on an optical component, the roughness impacts the performance by leading to large angle scattering of the light. Waviness is in the middle frequency regime, its range is normally wavelength dependent. In precision optical fabrication, Deck et al. [42] describes the range as from  $0.5 \text{ mm}^{-1}$  to  $1000 \text{ mm}^{-1}$ . It can be mathematically extracted from the surface profile with a band pass filter. These mid-frequency errors are typically produced by the instability in the fabrication process and can cause small angle scattering. In practice, a Fizeau interferometer along with an interferometric microscope is capable of covering the whole spectrum of waviness. Form is defined as the low



frequency deviation from ideal surface geometry, with spatial wavelengths beyond 1mm. Form error has a big impact on the functionality of a workpiece. For example, form error on a lens's surface will limit its imaging capability in terms of optical aberration. Long wavelength error can be caused by things such as over clamping and excessive handling in manufacturing process.

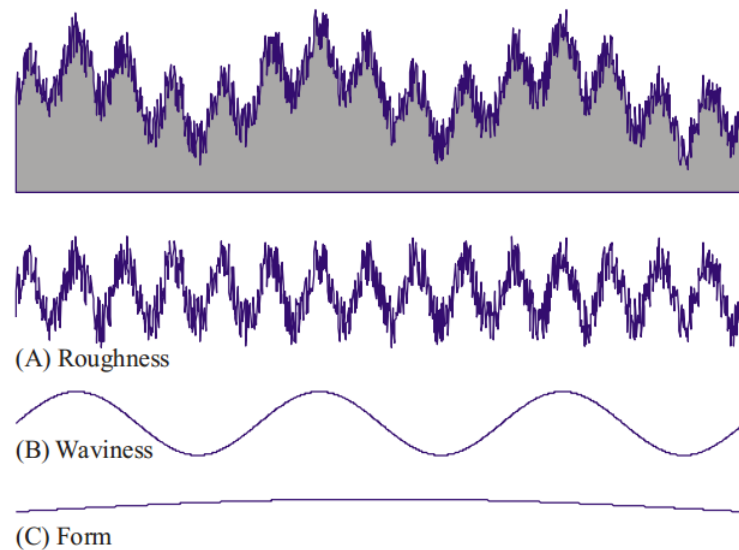


Figure 7: Components of a surface profile [43].

There are several different parameters for quantitatively describing a surface. Peak to valley (PV) is the most common and is used for specifying the distance from the highest point to lowest point of a surface. Because it is based on only 2 points in the surface profile, PV is easily biased by measurement noise. The root mean square (RMS) is another common parameter. Unlike PV, RMS is a single value that is a statistical description that represents the overall quality of a surface and is therefore less sensitive to noise. A drawback of RMS is the lack of spatial frequency distinction, it is meaningless unless bandwidth information is specified.

The power spectral density (PSD) is a quantitative measure of the spatial frequency characteristics of a surface and is commonly used to extract this information from a surface profile [44]. The PSD has units of length cubed and is often plotted as a function of spatial frequency. The PSD is sensitive to details of the calculation, however, and this limits its practical widespread use. In addition, the PSD normally provides no information on surface anisotropy. The area structure function (SF) has been recently proposed as an alternative way of quantifying the spatial frequency content of a surface [45], It is mathematically described as the expectation of the squared height difference as a function of separation. An area (2D) SF analysis can be used for describing the anisotropic characteristics of the spatial frequency content [46].

## 2.2 Scanning White Light Interferometer (SWLI)

### 2.2.1 Introduction of SWLI

Interferometers take advantage of electromagnetic wave superposition to diagnose surface characteristics. A typical interferometer separates light source as two independent optical paths, one of which includes a reference surface and the other the object surface. The separated light beams then recombine and interference fringes are observed at a digital camera due to the phase difference between the two beams. The signal of light irradiance over the field of view is captured simultaneously. The resulting irradiance of a single pixel is described by

$$I(x, y, z) = I_1 + I_2 + 2\sqrt{I_1 I_2} \cos[\Delta\phi(x, y, z)], \quad (2.1)$$

where  $I_1$  and  $I_2$  are the irradiances due to the object beam and the reference beam, individually. The parameter  $\Delta\Phi$  is the phase difference. The detected irradiance varies sinusoidally with the phase difference between the two waves as shown in figure 8.

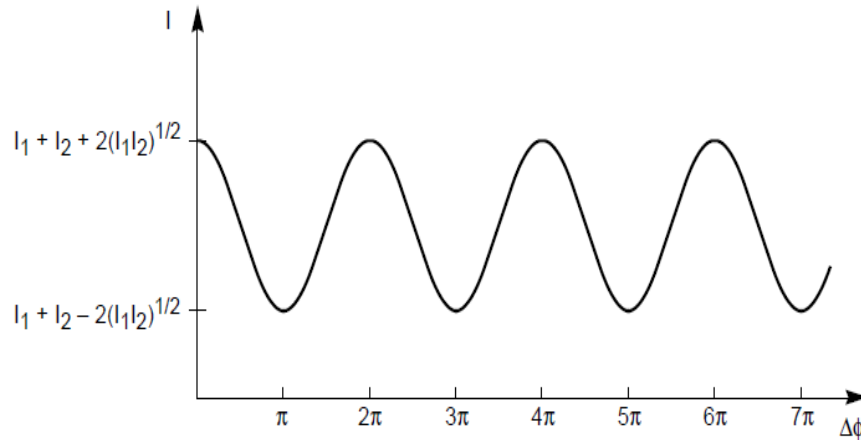


Figure 8: Interference irradiance variation as a function of phase difference.

Based on the working principle, interferometers can be divided into two categories: wavefront splitting and amplitude splitting. As shown in figure 9, Young's famous double slit interference experiment belongs to the wavefront splitting category. An emerging wavefront from a point source is divided into two wavefronts, and these two wavefronts travel different paths to the observation point where the superposition (interference) between the waves is observed. Other interferometers in this category include the Fresnel bi-prism, Lloyd's mirror and the Rayleigh interferometer. The second category of interferometers is based on amplitude splitting, as shown in figure 9. A Fizeau interferometer as an example, where the energy of a beam from a light source is separated by a beam splitter into two beams which later recombine and interference. Common interferometers in this category are the Michelson, the Twyman-Green, the Fizeau, the Mach-Zehnder and the Fabry P érot interferometers.

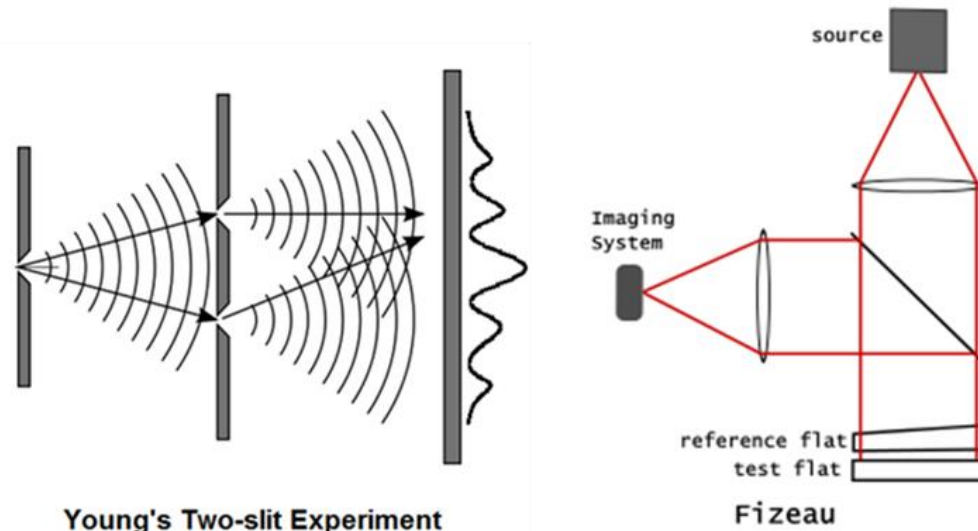


Figure 9: Wavefront splitting and amplitude splitting interferometry.

The scanning white light interferometer (SWLI) is a non-contact optical method for surface height measurements with surface profiles varying between a few micrometers to a few centimeters [47]. A typical SWLI setup is shown in figure 10. Often a broadband white light source is used for illumination with wavelengths spanning 400 nm to 800 nm. With the short coherent length of such a source, interference fringes are observed only if the measurement beam (reflected from the surface under test) and the reference beam have very similar optical path lengths. A piezoelectric transducer (PZT) is used to vertically move the objective with a typical scan range between 10  $\mu\text{m}$  and 200  $\mu\text{m}$ . Because the contrast of the fringes exhibit high sensitivity to the difference in optical path length, the fringe contrast at each pixel can be used to effectively provide a comparison between the object height at each pixel relative to the reference surface with nanometer resolution [2]. Different types of interferometric objectives are available. The Michelson, the Mirau, and the Linnik objectives are three most commonly used objectives on a SWLI. Generally, a long working distance and large field of view can be expected from

a Michelson objective. In contrast, Mirau and Linnik objectives usually offer a high magnification for imaging [2].

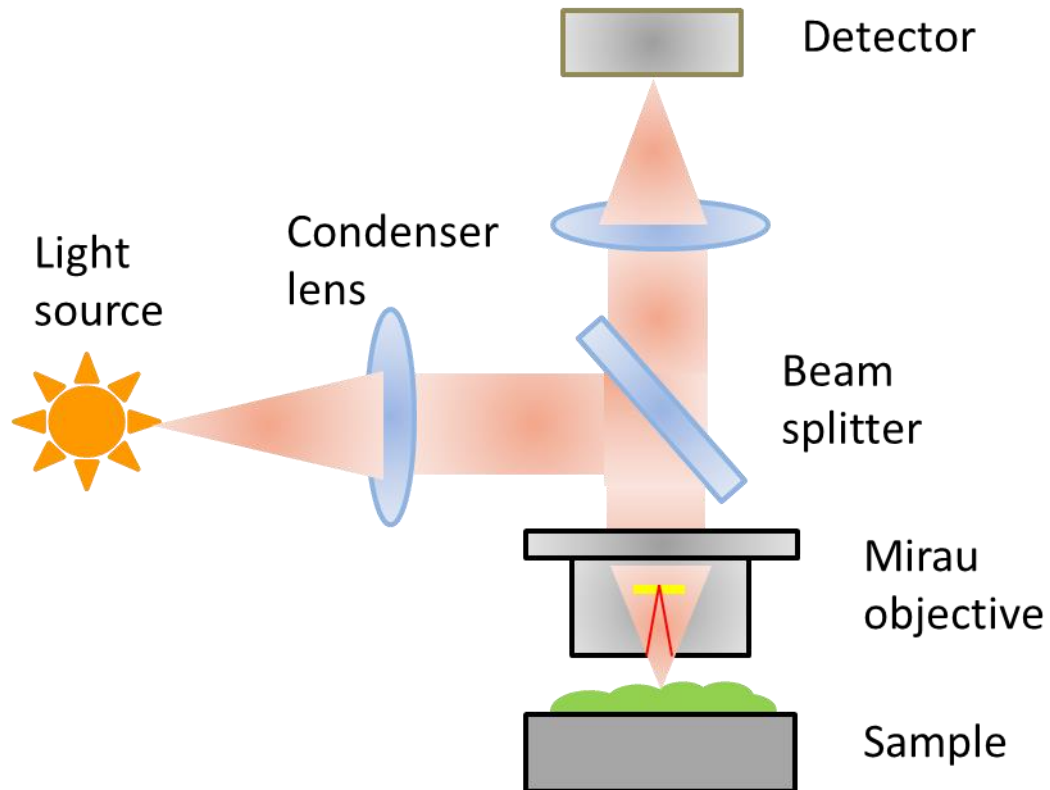


Figure 10: Schematic setup of a SWLI.

By scanning the objective along the vertical direction of a surface, an interferogram (as shown in figure 11) is produced at each pixel, representing the variation in flux as a function of scan position. The interference signal has maximum modulation when the optical path length of the reference matches the optical path length of the measurement arm. The maximum signal or best contrast fringe position therefore indicates the  $z$ -value of the surface at this pixel. A matrix with the height values of the surface can be determined from the  $z$ -values of the objective where the modulation is greatest for every

pixel. Depending on the surface property, various algorithms can be chosen for detecting the peak of modulation, detailed discussion is presented in next section.

The advantage of an interferometer over other optical measuring methods is that the resolution in height does not depend on the size of the field of view. The SWLI has many positive characteristics such as its non-contact nature, high resolution in the height direction, and fast data acquisition and processing times. Consequently, it is widely used in both industry and research institutes for surface area measurements.

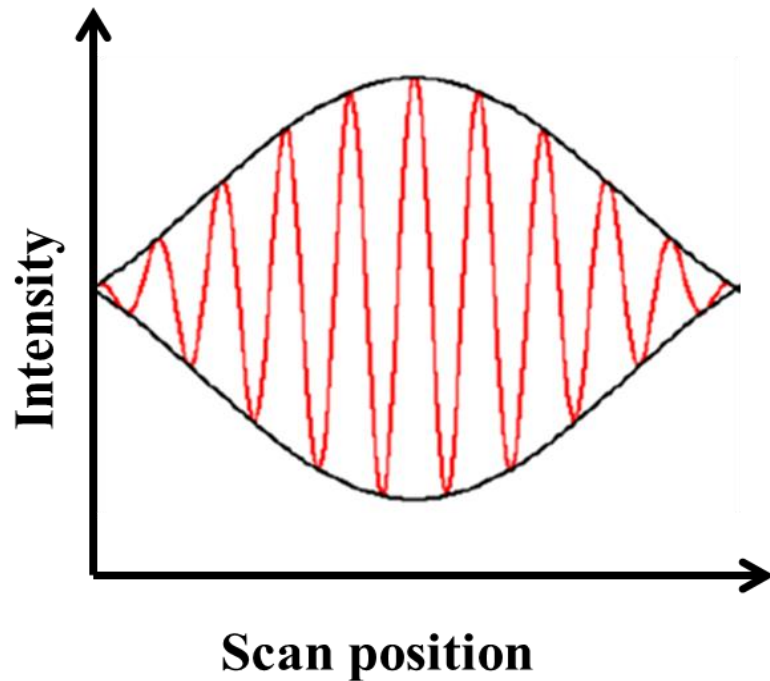


Figure 11: SWLI signal at a single pixel showing the modulation envelop.

### 2.2.2 Signal Processing of The White Light Interferogram

The white light interferogram is generated by recording the interference pattern at each pixel during the entire vertical scanning of the objective. The height information can

therefore be extracted pixel by pixel from the irradiance signal of interferogram. A variety of signal processing algorithms can be used to accomplish this task.

The easiest approach is to look for the peak in the modulation envelope by calculating the fringe contrast envelop point for point by digital demodulation [48] or by fitting the envelope near the peak to find the maximum contrast position. However, this approach can include a bias due to a phase separation between two adjacent frames. Additionally, dispersion causes a distortion of the envelope and makes the peak detection depend on the choice of the contrast phase reference feature [49].

P. de Groot and L. Deck [49, 50] proposed a powerful way of processing white light interferograms in the frequency domain. Frequency domain analysis (FDA) allows the separation of the phase information for each wavelength. Thus, the white light interferogram can be represented as a sum of various fringe frequencies, as show in figure 12. The optical path difference  $L$  is given by

$$L = \frac{d\phi}{dk}, \quad (2.2)$$

where  $\phi$  is the phase and  $k$  is the wave number. In the absence of chromatic dispersion, when  $L$  equals to zero, the phases will be the same for all frequencies.

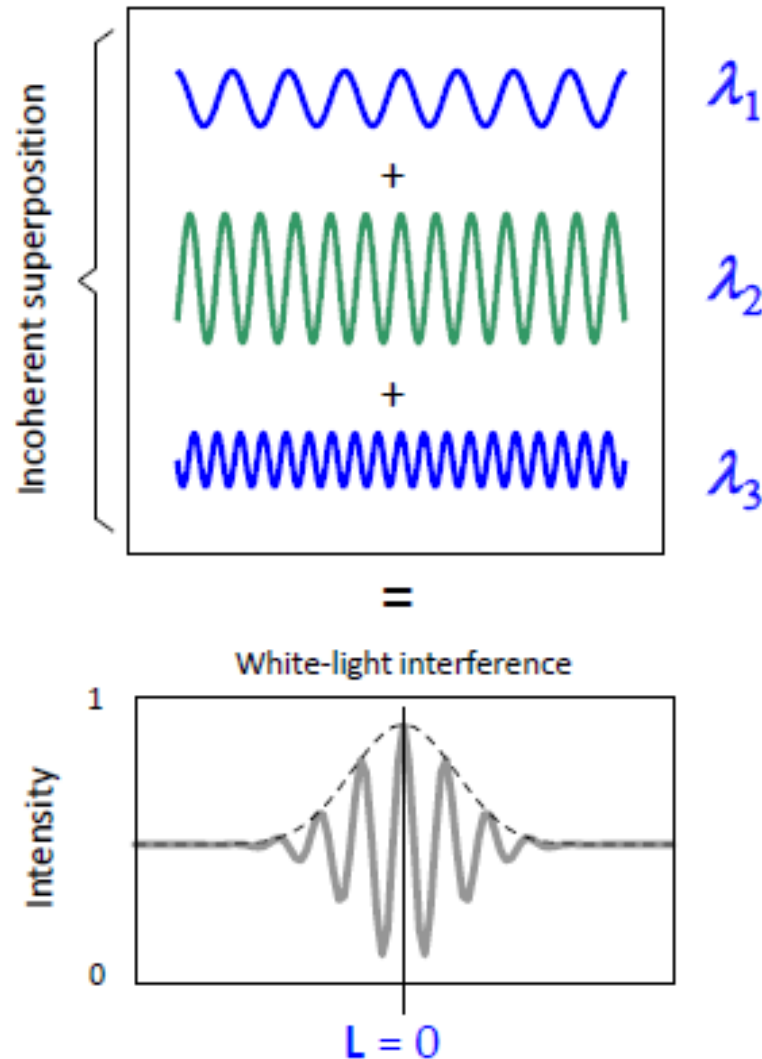


Figure 12: Monochromatic interference patterns for a white light interferogram [2].

Envelop peak detection works well for rough surface topography measurements, however it has some drawbacks when looking at certain kinds of surface features. For example, when it is used for a step-like discontinuity that has a height less than the coherence length of the light source, a bat-wing effect will be observed, as shown in figure 13. The bat-wing effect can be explained as the consequence of diffraction at the discontinuity that modify the coherence envelope more than the phase of the interferogram [15].



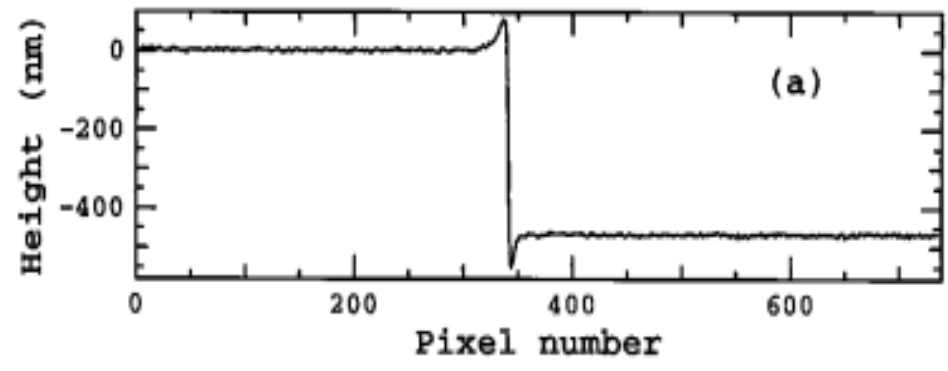


Figure 13: Surface profiles of the 460-nm height standard [15].

An improved algorithm that includes the phase information, measuring from the best-focus frame position, is capable of eliminating the spikes or wings at the edge of step [15, 51, 52]. The idea is to find the peak of modulation envelope first, then extract the fractional phase between fringe peak and envelop peak as shown in figure 14 to correct height errors.

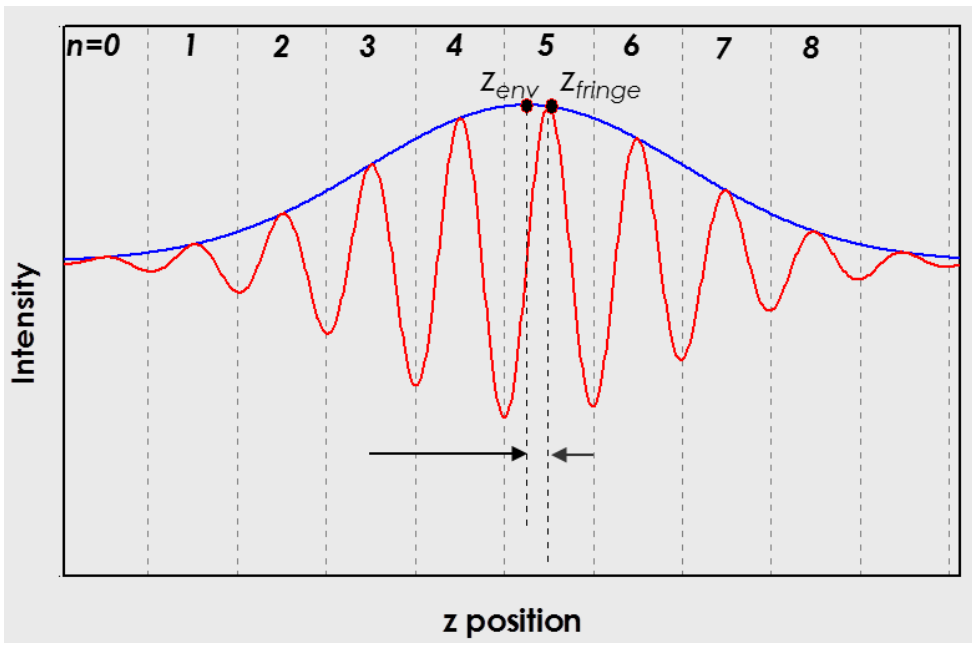


Figure 14: Envelope peak and phase peak of a white light interferogram.

To process a SWLI interferogram, as shown in figure 15, the envelope peak detection method helps to eliminate fringe order ambiguity, and the phase information provides the high resolution height values for the surface.

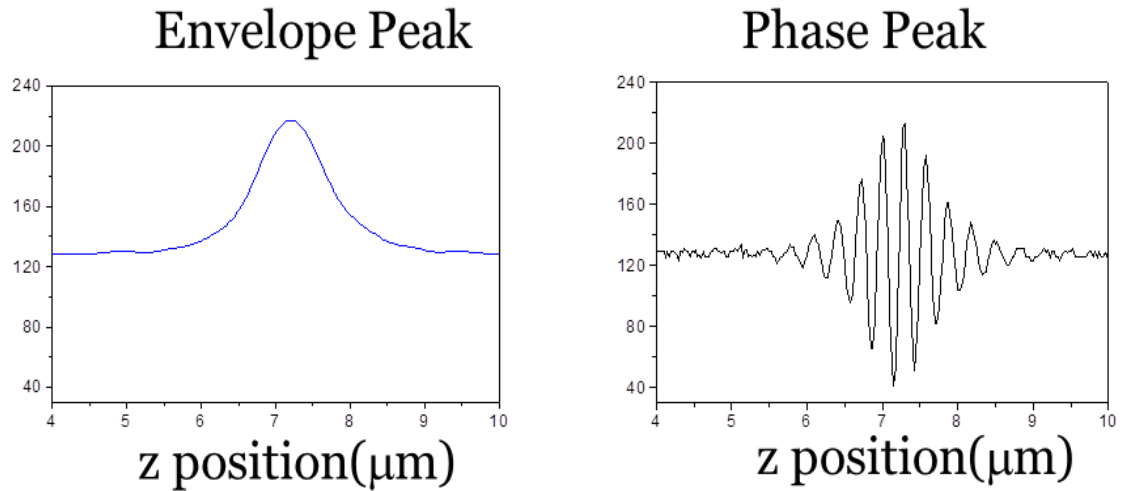









Figure 15: SWLI signal processing algorithms: envelope peak (left) and phase peak (right).

However, in practice many factors contribute to the measurement such as the complexity of surface features, chromatic aberration [14], scan-dependent distortion, etc., and the combined effect often leads to the misidentification of the fringe order. Phase gap analysis was proposed to determine the fringe order by data filtering, surface fitting and other procedures in frequency domain [53]. Much research has been done and is continuing to address this problem to further improve SWLI measurements. For example, Niehues et al. [17] proposed a way to eliminate  $2\pi$  phase jumps in the measured surface by using a second LED with a different wavelength band to obtain additional phase information. Ghim and Davies [54] use a similar idea to solve the phase jump errors by extracting the signal at two wavelengths, a method that does not require a physical modification of the SWLI. Figure 16 summarizes the applicable evaluation methods for different surface profiles, along with problems and possible solutions.

Case No.	Real Profile (two-dim.)		Preferred Evaluation Mode	Occurring Problem	Possible Solution
1.		specular flat surface, no tilt	phase evaluation <sup>(*)</sup>	–	–
2.		specular surface, overall tilt	phase evaluation <sup>(*)</sup>	dispersion / lateral color errors → changing difference between position of coherence peak and phase evaluation → phase jumps (ghost steps)	conventional phase unwrapping, dual-wavelength phase unwrapping
3.		curved specular surface	phase evaluation <sup>(*)</sup>		
4.		specular surface with height steps	phase evaluation <sup>(*)</sup>	batwing effect → erroneous fringe order determination → phase jumps (spikes) at edges	conventional phase unwrapping if maximum height difference $\Delta h < \lambda/4$ ;
5.		specular surface with height steps and tilt / curvature	phase evaluation <sup>(*)</sup>	combination of case no.: 2. and 4. 3. and 4. or 2., 3., and 4.	dual-wavelength phase unwrapping
6.		rough surface of a flat, curved, or tilted object with or without height steps	coherence peak (envelope) evaluation	–	–
7.		specular surface of different materials	phase evaluation <sup>(*)</sup>	phase jumps due to different complex refractive indices	dual-/multiple-wavelength technique for material identification

(\*) a specular surface phase evaluation is generally necessary in order to achieve an optimum measuring uncertainty

Figure 16: Different types of profile and preferred interferogram processing algorithms for each case with occurring problems and possible solutions [17].

### 2.2.3 Systematic Bias of SWLI

Scanning white light interferometry has become a firmly established optical technique for 3D surface measurements over the past few decades [49, 50, 55]. The most advanced SWLI is capable of measuring a large slope range of surface [56]. It is widely used in many fields such as data storage, automotive, MEMS, electronics, micro-optics, and biomedical. However in some circumstances, these tools can add a systematic bias to the measurement that can be the same order of magnitude as features to be measured.

Vorburger et al. [57] provided a comparison between stylus and optical profilers with different types of surfaces. The results show that there are significant deviations between SWLI and stylus measurements in some cases.

The “Batwing” effect, as shown in figure 13, is a well-known example of a SWLI bias when measuring a discontinuity in a surface such as a step height that is less than the coherence length. The reason for this is widely accepted, and is due to diffraction at the step edge and the interference of reflected light, causing the coherence envelope to skew and the peak to shift [3, 15]. The envelope peak detection combined with the phase information algorithm discussed in section 2.2.2 corrects this error. For highly curved surfaces, noise can cause phase jumps that result in the ghost step effect, as shown in figure 17. This is caused by an inconsistency between the phase peak and the envelope peak, in part due to field dependent dispersion [14, 58]. Although it was proposed this type of error can be corrected by compensating chromatic aberration in the testing arm of the interferometer, it is not easy to do and/or practical for a commercial SWLI.

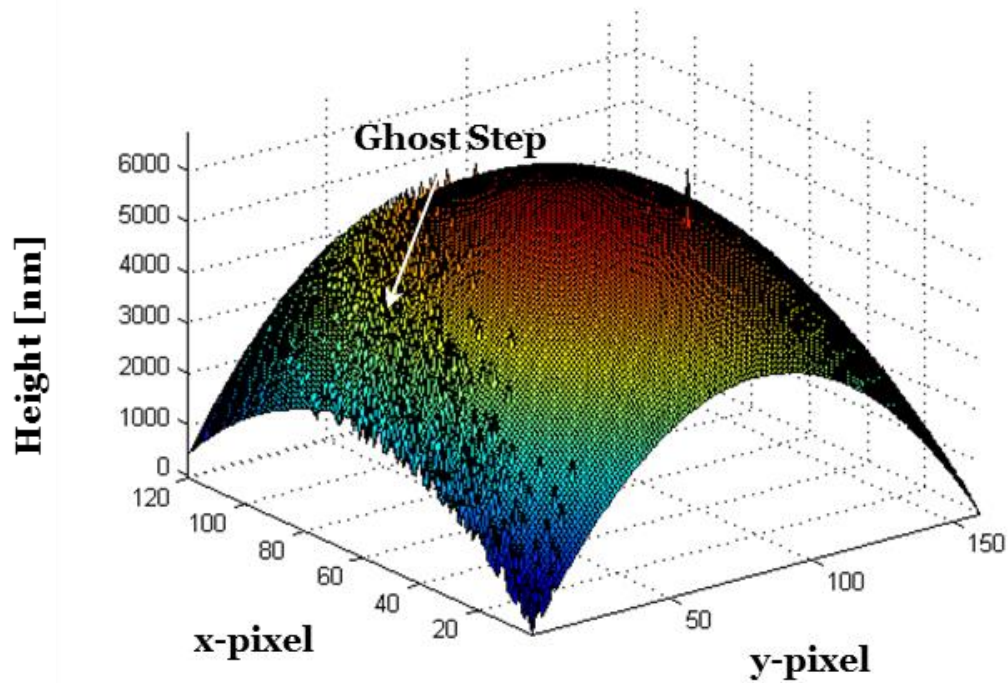


Figure 17: SWLI Ghost step example on a spherical surface due to phase jump [54].

Nominally the SWLI is limited to the surface slope that can be measured by the NA of the objective used. Sometimes a measurement signal is observed under conditions that violate this condition. An example is shown in figure 18, which is a SWLI measurement of a silicon V-groove with an internal angle of 70 degrees. A peak with its apex at the bottom of profile is observed [4], which is believed to be a spurious signal due to multiple scatterings or reflection between side walls. Considerable errors can be expected in these measurements [59, 60].

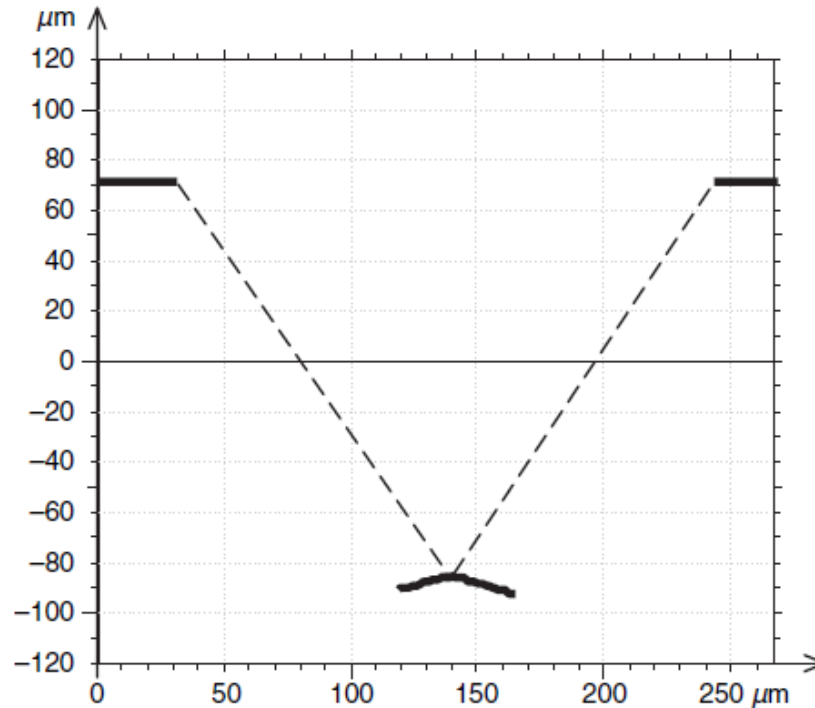


Figure 18: Measurement of a silicon V-groove [60].

SWLI is typically calibrated with step height standards but this calibration will not account for slope-dependent systematic errors. Many surfaces have appreciable continuous slope variation, slopes reaching the measurement limitation of the instrument. Slope-dependent errors can be significant and are expected [61]. Beyond the measurement biases discussed above, a bias is also expected if the surface under test is composed of different materials, particularly with metallic surfaces. The optical properties from materials vary and a phase change upon reflection is present for metals. Thus the phase of the reflected beam does not only carry path length information. The accuracy of a SWLI measurement is highly dependent on the data processing algorithm used and this is usually a proprietary aspect of the instrument and therefore unknown. Thus there has a strong need for a rigorous and convenient calibration method to allow the user to independently validate instrument performance.

### 2.3 Laser Scanning Confocal Microscopy (LSCM)

Besides SWLI, another high resolution surface topography instrument is the laser scanning confocal microscope (LSCM). It is a widely used tool in many fields such as biology, material science and even circuit inspection for the semiconductor industry. Unlike conventional wide field optical microscopy whose data points of the image are collected from the object simultaneously, a LSCM forms an image in a point by point fashion. The idea of confocal microscopy was proposed and patented by Minsky back in the 1950s [62]. Tremendous development and began later in the late 1970s after the expiration of the patent and the availability of intense laser light sources and powerful computers [63, 64].

A typical LSCM setup is shown in figure 19. A laser beam is redirected by a beam splitter and focused onto the surface of the specimen. The reflected light is then collected by the objective. A pinhole in front of the detector reduces the signal from out of focus regions of the surface. As the sample (or objective) is scanned along the optical (z) axis, a photo detector captures the light signal information at each pixel over the field of view. The signal at a pixel is a maximum when the z-height corresponds to the condition where the surface is in focus. Thus, the three dimensional surface height profile is generated by processing the signal intensity at each pixel and extracting the array of peak z-scan positions.

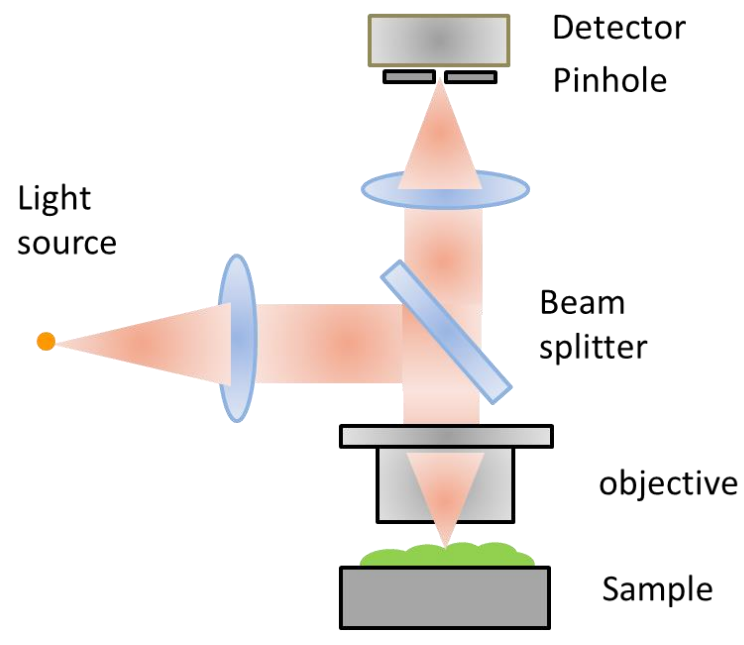


Figure 19: Schematic setup of a LSCM.

Similar to SWLI, the LSCM also owns the advantage of producing reduced-blur images (figure 20) by optical sectioning, that is using the maximum response of the z stacked signals for each pixel giving the axial position of a surface point. The beam is scanned in X and Y direction as well in order to generate a full confocal image. Conceptually its scanning imaging process is similar to SEM.

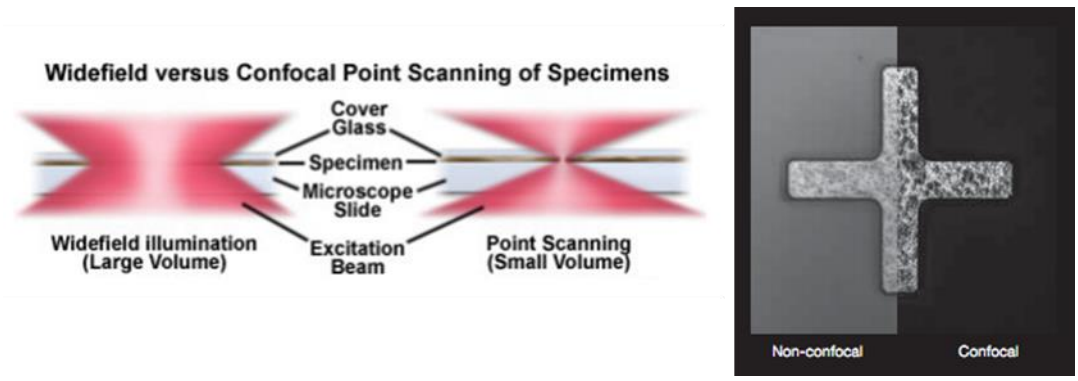


Figure 20 Comparison of wide field microscopy and confocal microscopy.



The resolution of an optical microscope is typically diffraction limited, depending on the numerical aperture and wavelength. For a LSCM, the pinhole size plays an important role in determining the resolution. It is intuitive to think that a broaden signal distribution could be expected with a larger pinhole size, thus a lower resolution would be expected - wide field microscopy is an example with infinite pinhole size. The pinhole size is normally smaller than the diameter of the Airy disk (AU). The point spread function of an LSCM shows that a good pinhole size is 0.5 AU to keep good confocality and to maximize the detector signal [2]. When the pinhole size goes down below 0.25 AU, diffraction effects appear. The lateral resolution of LSCM is determined by the wave-optical confocality given by the equation

$$d = \frac{0.37\lambda}{NA}, \quad (2.3)$$

where  $\lambda$  is the wavelength of light source and NA is the numerical aperture [2]. On the other hand, for a pinhole size larger than 0.25 AU, the lateral resolution is determined by the geometrical-optical confocality given by

$$d = \frac{0.61\lambda}{NA}. \quad (2.4)$$

The quality of the image generated in a LSCM is not only influenced by the optics and pinhole, but also by noise such as laser noise and the signal processing algorithm chosen. To minimize noise, signal processing as well as optoelectronic and electronic devices need to be optimized. Current commercial LSCMs are capable of obtaining nanometer resolution in the vertical direction and can measure up to several millimeters in the vertical direction. LSCM has ability to measure a large surface slope range – reportedly up to 85 degrees as shown in figure 21.

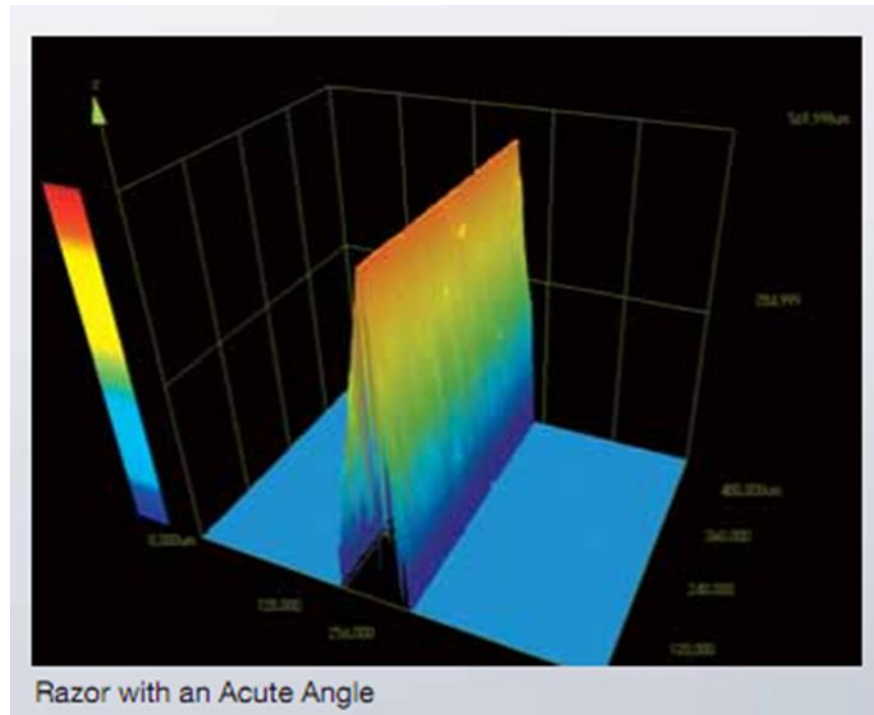


Figure 21: An example of a steep sloped surface measurement with LSCM [21].

As LSCM becomes a mainstreamed tool for dedicate surface measurements, knowledge of the accuracy of the measurement is critical more than ever. This type of height measuring instrument is typically calibrated with step height standards, but again this calibration will not account for slope-dependent systematic errors. Thus, careful calibration is needed for such an instrument.

## CHAPTER 3: RANDOM BALL TEST (RBT) SIMULATION FOR OPTICAL PROFILER

### 3.1 Simulate A RBT For Profiler Calibration

The RBT was first introduced as a self-calibration technique for spherical part measurements in phase shifting interferometry (PSI), where the measurement goal is the surface departure from a sphere [26]. For this calibration, as shown in figure 22, surface measurements are taken of a collection of random patches on the surface of a ball. These measurements are averaged and the imperfections in the ball are approximately removed from the average – that is the ball imperfections average out. The average then shows the systematic errors added to each measurement from the instrument. The process simulates having measured a perfect spherical artifact.

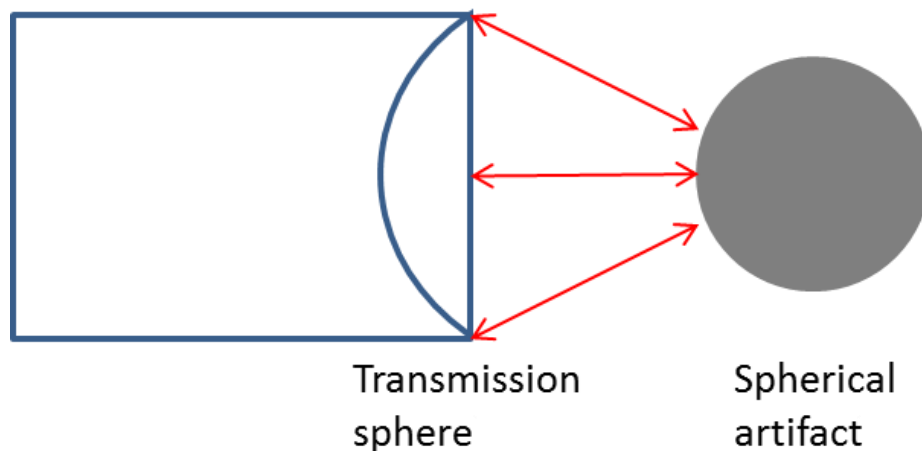


Figure 22: RBT calibration for a transmission sphere of a phase shifting interferometer.

The RBT is an absolute test technique based on averaging a series of ball surface patch measurements for the purpose of calculating the systematic bias that the instrument itself adds to the measurement. The RBT technique has been well established in several papers for calibrating transmission spheres in phase shifting interferometry [26, 65, 66]. The application of the RBT to a profilometry measurement begins with the assertion that a profile measurement of a patch on a ball in a profilometer can be written as

$$W = W_{ball} + \varepsilon_{noise} + \varepsilon_{bias} , \quad (3.1)$$

where  $W_{ball}$  represents the ball geometry contribution to the measurement,  $\varepsilon_{noise}$  is the random noise during the profile capturing process, and  $\varepsilon_{bias}$  is the systematic bias from instrument. Furthermore,  $W_{ball}$  can be written as the combination of a perfect ball profile  $W_{base}$  and the ball error on that patch  $W_{ballerror}$ . So, the measurement result will become

$$W = W_{base} + W_{ballerror} + \varepsilon_{noise} + \varepsilon_{bias} . \quad (3.2)$$

If the ball is randomly rotated under the field of view, a collection of patch measurements can be obtained, as shown in figure 23. We assert that with infinite measurements and averaging, terms  $W_{ballerror}$  and  $\varepsilon_{noise}$  converge to zero, leaving only a perfect sphere contribution and the systematic bias from the instrument,

$$\langle W_i \rangle = W_{base} + \varepsilon_{bias} . \quad (3.3)$$

In PSI, tip, tilt and power in the measurement are removed and the average  $\langle W_i \rangle$  contains only the last term, becoming a direct measure of the system bias. However, profilometry is a direct height capturing process, so the curvature is retained and should be representative of true geometry. For profilometry, an estimate of the first term on the right is needed to solve for the last term,  $\varepsilon_{noise}$ . The perfect ball height profile,  $W_{base}$ ,

can be estimated from an independent measurement of the base radius of the ball used for the calibration. Of course, the uncertainty in the calibration depends on how well the radius can be measured. Another consideration is that the height measurement in PSI is in the radial direction whereas profilometry is a direct height (sag) measurement (see inset in figure 23). A spherical harmonic description of ball geometry in the radial direction shows that the departures from the base sphere in the radial direction are identically zero on average [26, 65, 66]. It does not directly follow that the departures in the sag direction from the base sphere are identically zero on average. Thus, the application to profilometry deserves careful consideration, and this was investigated with a numerical simulation in Matlab™.

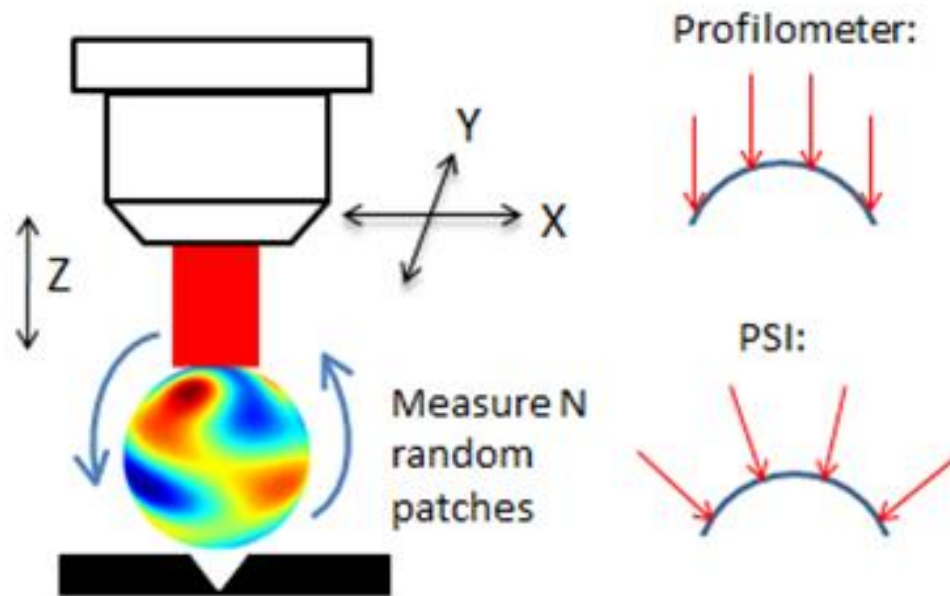


Figure 23: Schematic of the RBT calibration configuration. Upper right: profilometer. Lower right: phase shifting interferometer (PSI).

### 3.1.1 Realistic Ball Generation

A realistic ball with surface form errors can be described by a set of spherical harmonic terms,

$$A(\theta, \phi) = \sum_{l,m} a_l^m Y_l^m(\theta, \phi) = \sum_{l,m} a_l^m \sqrt{\frac{2l+1}{4\pi} \frac{(l-m)!}{(l+m)!}} P_l^m(\cos \theta) e^{im\phi}, \quad (3.4)$$

where  $a_l^m$  are the multiplication constants and  $Y_l^m$  are the spherical harmonics which are a function of  $\theta$  and  $\phi$ . The variable  $\theta$  is taken as the polar (colatitudinal) coordinate with  $\theta \in [0, \pi]$ , and  $\phi$  is taken as the azimuthal (longitudinal) coordinate with  $\phi \in [0, 2\pi]$ .

The parameters  $P_l^m$  are the associated Legendre polynomials [67]. In the RBT, the ball is rotated and measured many times and each region on the surface is captured in the average in the limit that the number of measurements  $N$  equals infinity. This means that every angle of  $\theta$  and  $\phi$  will be included. Since the integration of spherical harmonics in the radial direction over all angles is 0, ball imperfections will be averaged out. Table 2 below is a list of a few spherical harmonic functions in mathematic form. It is clear that for a series of spherical harmonics  $Y_l^m$ , the zero order ( $m$ ) and zero degree ( $l$ ) term represents a constant and therefore is the only term left after integration. This term describes the base sphere with a particular radius.

Table 2: Mathematic expressions of some low order spherical harmonic functions.

l	m	Spherical harmonics
0	0	$(1/4\pi)^{1/2}$
1	0	$(3/4\pi)^{1/2} \cos\theta$
1	$\pm 1$	$\mp (3/8\pi)^{1/2} \sin\theta e^{\pm i\phi}$
2	0	$(5/16\pi)^{1/2} (3\cos^2\theta - 1)$
2	$\pm 1$	$\mp (15/8\pi)^{1/2} \sin\theta \cos\theta e^{\pm i\phi}$
2	$\pm 2$	$(15/32\pi)^{1/2} \sin^2\theta e^{\pm 2i\phi}$

In the simulation, we use equation 3.4 to generate a realistic geometry for a ball by choosing a set of low order spherical harmonic functions, as shown in figure 24. We chose parameters to match approximate experimental values, in particular coefficients are chosen so the overall root mean square (RMS) for the ball is  $\sim 100$  nm and the base radius value matches that of balls used for actual calibrations.

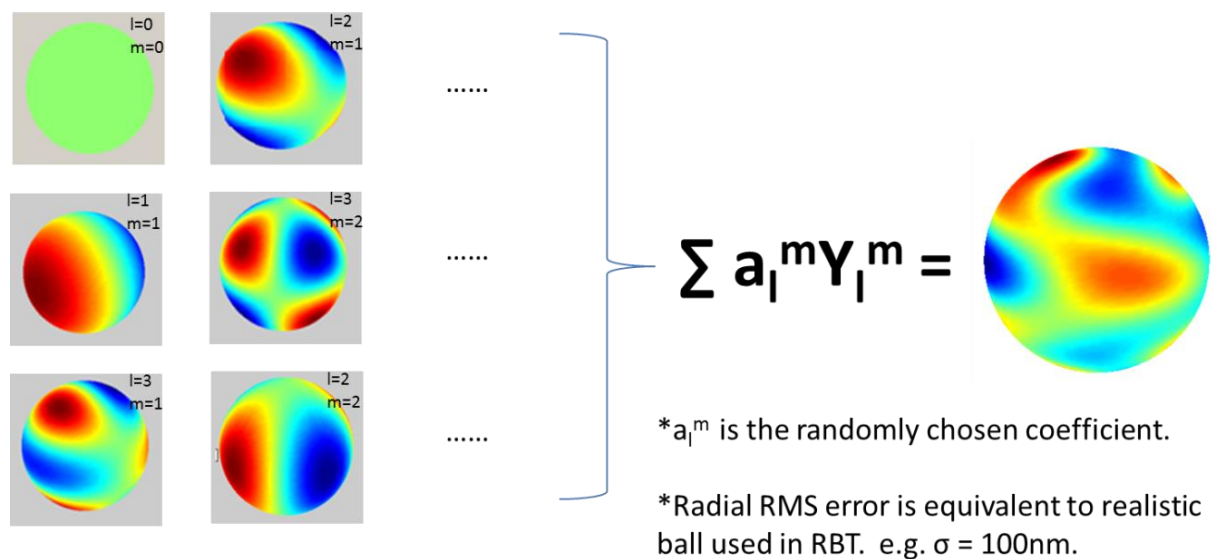


Figure 24: A realistic ball with RMS=100 nm was generated by a set of low order spherical harmonics.

### 3.1.2 Random Rotations

After generating a realistic ball, we allow for the ball orientation to be randomly varied  $N$  times by choosing the polar and azimuthal angles from uniform distributions. Each simulated measurement will then correspond to a randomly chosen polar and azimuthal angle at the center of the field of view. For mathematical simplicity, we choose a Cartesian coordinate system to carry out the rotations. To complete this task in XYZ coordinates, we first rotate a random angle  $\alpha \in [0, 2\pi]$  along the  $Z$  axis with the rotation matrix

$$R_z(\alpha) = \begin{pmatrix} \cos \alpha & -\sin \alpha & 0 \\ \sin \alpha & \cos \alpha & 0 \\ 0 & 0 & 1 \end{pmatrix}. \quad (3.5)$$

Then we rotate by another random angle  $\beta \in [0, \pi]$  along the  $Y$  axis,

$$R_y(\beta) = \begin{pmatrix} \cos \beta & 0 & \sin \beta \\ 0 & 1 & 0 \\ -\sin \beta & 0 & \cos \beta \end{pmatrix}. \quad (3.6)$$

At last, similar to the first step, we rotate by a random angle  $\gamma \in [0, 2\pi]$  along the  $Z$  axis again.[67] Sample distributions of  $\theta$  and  $\phi$  values for a collection of  $N=10,000$  rotations is shown in figure 25. After the rotation, the new random patch on the ball is oriented up along the  $z$ -axis. The profilometry measurement of this top cap of the ball is then simulated by generating a matrix of the  $z$  sag values over a uniform grid of  $xy$  coordinates. The grid size is taken to be 128 by 128 and the  $xy$  spacing is chosen to match a particular measurement magnification.



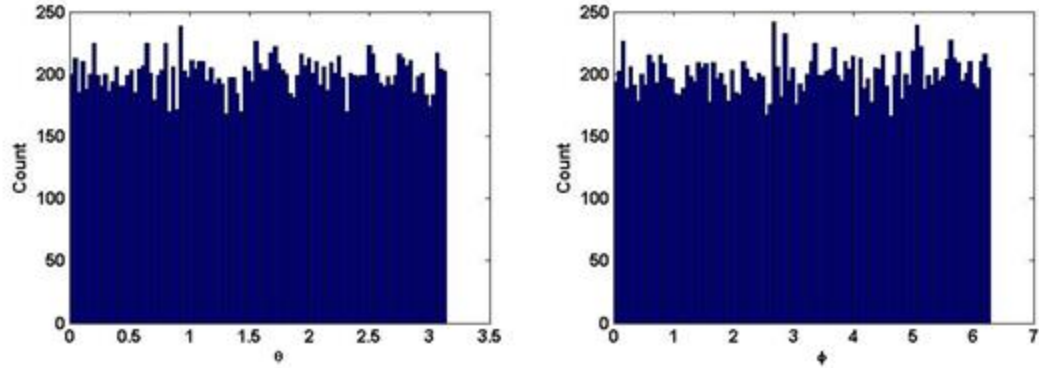


Figure 25: An example of the polar angle  $\theta$  and azimuthal angle  $\phi$  distributions for a simulation with  $N=10,000$ . The rotation is done by rotating through angles  $\alpha, \beta, \gamma$  along the XYZ Cartesian axes.

### 3.1.3 Robust Best Fit Sphere Algorithm

Our RBT simulation goal is to see if the average of many measurements of randomly chosen patches on the surface of the ball converges to a measurement of a perfect sphere. This would mean the average converges to a perfect spherical cap with a radius equal to that of the base sphere used in the spherical harmonic generation of the ball (the  $a_{0,0}$  term in equation 3.4). If the RBT result does not converge to a perfect sphere with the correct best-fit sphere radius, we cannot be assured that curvature in the final result is due entirely to an instrument bias. Thus, we fit the resulting average of our simulated measurements (the result of the simulated RBT) to a sphere to determine the best-fit radius. The best-fit radius is then compared to the base radius which is the value of the  $a_{0,0}$  coefficient in equation 3.4. If the best fit radius of the final average  $\langle W_i \rangle$ , is the same as the base radius, we would then conclude that the RBT provides a valid calibration.

Consideration of the range of surface slopes that can be measured leads to a ball choice whose radius is much larger than the field of view of the measurement, as shown

in figure 26. This means the measurement represents a small cap on top of a large sphere. A least-square fit to such a geometry to determine a best-fit radius can be difficult.

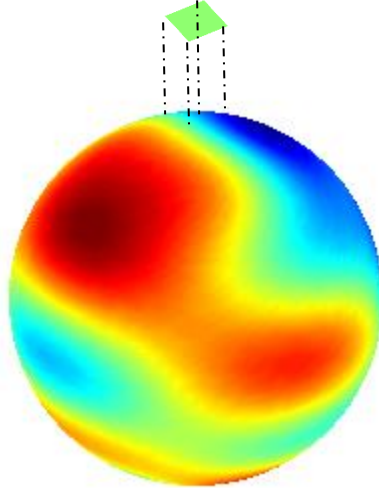


Figure 26: Example of the size scales involved when applying the RBT to the calibration of a confocal microscope (Olympus LEXT 4000) with a 50x field of view (0.256 mm x 0.256 mm). This simulated ball has a radius and surface error comparable to the real ball used for the demonstration calibration:  $R=0.595$  mm and  $RMS=100$ nm.

The common least square fit to a sphere would involve 4 free fit parameters (center coordinates (a, b, c) and radius R), and this is not robust for a small cap that can have an arbitrary tip/tilt orientation. The general equation of such a spherical cap in Cartesian coordinates can be written as

$$A(x^2 + y^2 + z^2) + Bx + Cy + Dz + E = 0 . \quad (3.7)$$

A more robust best-fit sphere can be found by constraining the number of parameters A, B, C, D and E in this equation [68]. Since the cap is very small, it is nearly planar, and we first fit the data to a plane to obtain initial parameter values and the centroid. The cap is then rotated so the normal to the best-fit plane points along the positive Z axis. This sets the parameter  $D = 1$ . Now that the overall tip/tilt has been removed, the last step is to do the least square fit to find the parameter values in the original global coordinate

system,  $a$ ,  $b$ ,  $c$  and  $R$ . These are related to the parameters in equation. 3.7 through the following relationships:

$$a = \frac{-B}{2A} \quad (3.8)$$

$$b = \frac{-C}{2A} \quad (3.9)$$

$$c = \frac{-D}{2A} \quad (3.10)$$

$$R = \frac{-\sqrt{B^2 + C^2 + D^2 - 4AE}}{2A}. \quad (3.11)$$

#### 3.1.4 Simulation Speed Improvement

A single ball patch measurement from optical profiler often consists of more than a million pixels to ensure its high resolution. In order to validate the RBT application on profilometer, a large collection of patches should be carried out by simulation. As a result, a single RBT might exceed hundreds of million data points (e.g. each patch has a grid 201x201 for N=10000 times.) The uncertainty study of RBT requires a series of RBTs, and the number of data points in this case can easily exceed tens of billion. Each point is calculated by spherical harmonic function of equation 3.4 to determine the ball error. Thus, high speed data processing is necessary for validating the RBT in simulation.

Several ways can speed up data processing in Matlab, for example, matrix manipulations generally are faster than ‘for’ loops, the ‘parfor’ function can increase

speed loops by utilizing multiple cores at a time. A major improvement for the simulation is that, instead of solving equation 3.4 for each point, we use a defined cap grid (e.g. 201x201 pixels) and then randomly rotate it on the ball surface to obtain the angular information  $(\theta, \varphi)$  and a saved  $(\theta, \varphi)$  matrix is then plugged into equation 3.4 to solve for all points of the ball errors. The time requirement decreases from several hours down to less than 10 minutes for one RBT, which makes it possible to validate the application of the RBT. The details of the algorithm are shown in Appendix A.

The whole RBT simulation process consists of 5 steps as following:

1. Generate a field of view sized grid.
2. Randomly reorient the grid on the ball surface to obtain angular information  $(\theta, \varphi)$  of each point.
3. Solve spherical harmonics to generate a realistic patch on the ball,  $W_i$
4. Average the measurements:  $\langle W_i \rangle$
5. Check residual RMS  $(\langle W_i \rangle - W_{base})$  and to see if best fit radius of  $\langle W_i \rangle$  equals the nominal radius.

### 3.2 Ball Error Distribution Study

Our simulation shows that the RBT result does not always converge to the correct base radius. The symmetry of the ball's geometrical errors impacts the result - a ball that does not have a symmetric geometric error does not result in the correct best-fit sphere radius. The symmetry of the ball refers to the distribution of radial values. This distribution is not necessarily symmetric about the base radius. This is demonstrated in figure 27 where we show 2 examples of (very exaggerated) ball geometries. The geometry on the left is

symmetric while the geometry on the right is not. The symmetry is a result of the spherical harmonic functions used to represent the ball geometry.

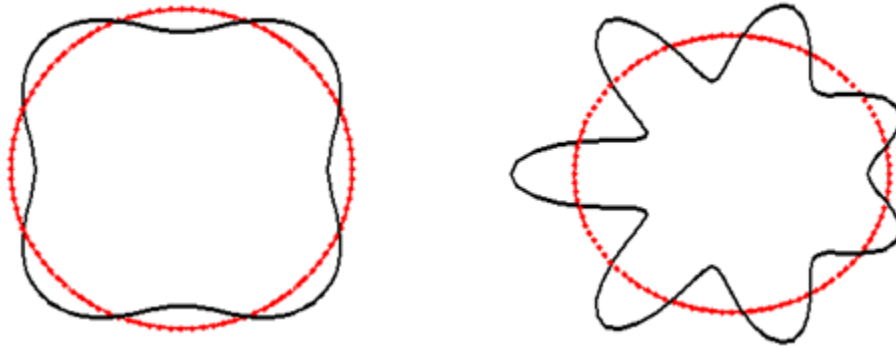


Figure 27: Simulated ball with a (exaggerated) symmetric ball error distribution (left). Simulated ball with an (exaggerated) asymmetric ball error distribution (right).

With a symmetric ball error distribution, the best fit radius converges to the correct base radius. An asymmetric ball error distribution does not, but the offset is quite small. This is shown in figure 28. The figure shows the size of this offset for a symmetric versus asymmetric ball as a function of the relative size of the measurement field of view (FoV). The RMS of the ball is 100 nm in both cases. The relative size of the FoV is the ratio of the FoV to the diameter of the ball. The offset can be positive or negative, depending on the sign of the ball asymmetry, and tends to zero when the FoV is very small. A symmetric ball always results in a correct best-fit radius.

When the ball is asymmetric, the radius offset is the largest when the spatial scale of the ball error (waviness) is close to the field of view (FoV). For a 100 nm RMS ball and a waviness that matches the experimental FoV, we find a worse-case offset in the best-fit radius value of 55 nm. This leads to a small sag artifact of  $\sim 3$  nm in the calibration over the FoV compared to the perfect base sphere. A 3 nm artifact in the calibration is negligible, as we will show, compared to the size of the instrument biases we find.

Although there has ways to measure the ball error over the whole surface [69], it is still difficult to know the extent of the ball asymmetry in an actual ball. Our analysis puts a reasonable bound on the size of this effect.

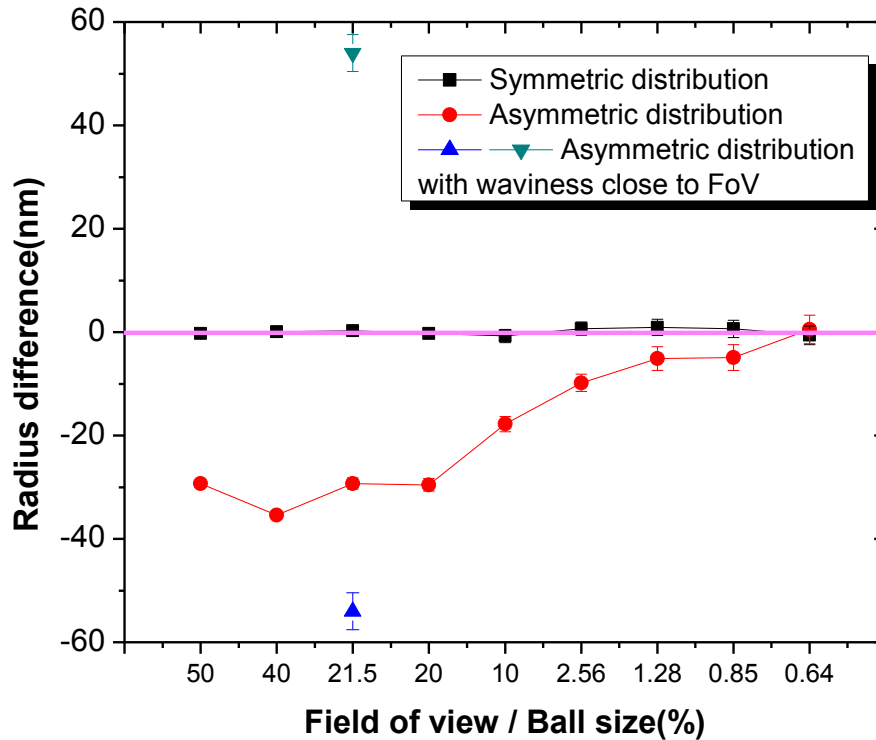


Figure 28: Difference between best fit and base radius as a function of ball size for three different ball error distributions. A FoV-to-diameter ratio of 21.5% matches the experimental conditions for the confocal calibration described below. The RBT with  $N=10,000$  is simulated 100 times at each ball size. The mean of the radius difference distribution for each ball size is plotted with error bars that are the statistical uncertainty in the mean (the standard deviation among the sample of 100 divided by the square root of 100).

We also investigated the dependence on the quality of the ball. This is shown in figure 29. Regardless of the RMS error of the ball, a symmetric ball leads to a best-fit radius that agrees with the base radius. As expected, the offset seen with an asymmetric ball gets larger as the quality of the ball goes down. For a ball with  $RMS = 500\text{nm}$ , the maximum radius offset increases to  $\sim 180\text{ nm}$ .

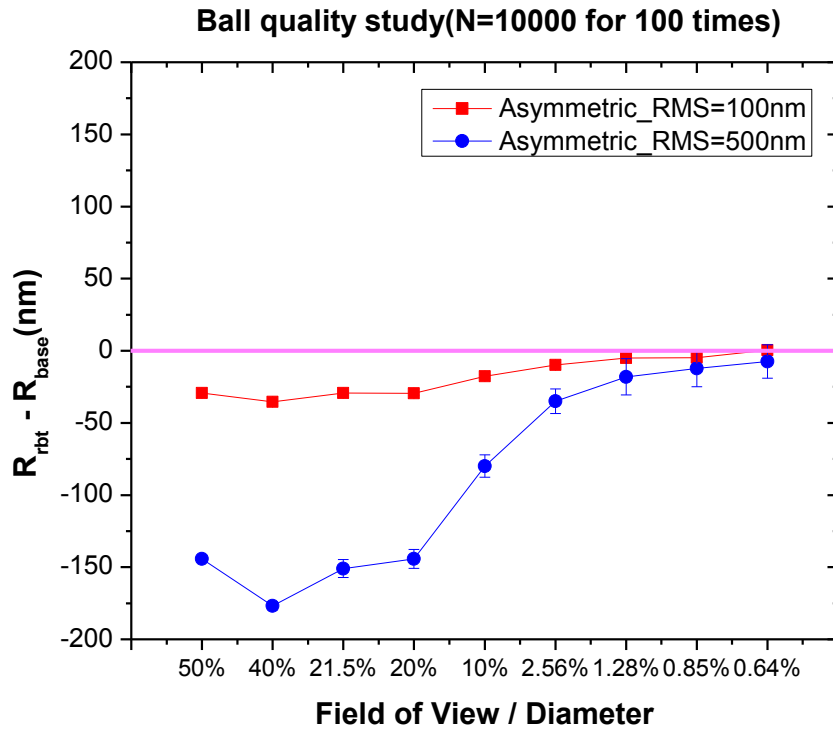


Figure 29: Ball quality study. Radius difference between best fit sphere and base sphere as a function of ball size for two different ball error RMS.

### 3.3 Number of Rotations Study

The rate at which the RBT result converges to a perfect sphere was also investigated.

This is studied by changing the number of measurements,  $N$ . The RBT with  $N = 10, 60, 100,$  and  $10000$  was carried out in simulation, respectively, with a ball RMS error  $\sigma_{\text{ball}} = 100 \text{ nm}$  and radius  $R = 2 \text{ mm}$ . Residual error is the difference between the random ball test result  $\langle W_i \rangle$  and a base sphere. As shown in figure 30, the convergence trend is clear - with large  $N$ , more ball imperfections are averaged out and the RMS residual is smaller.

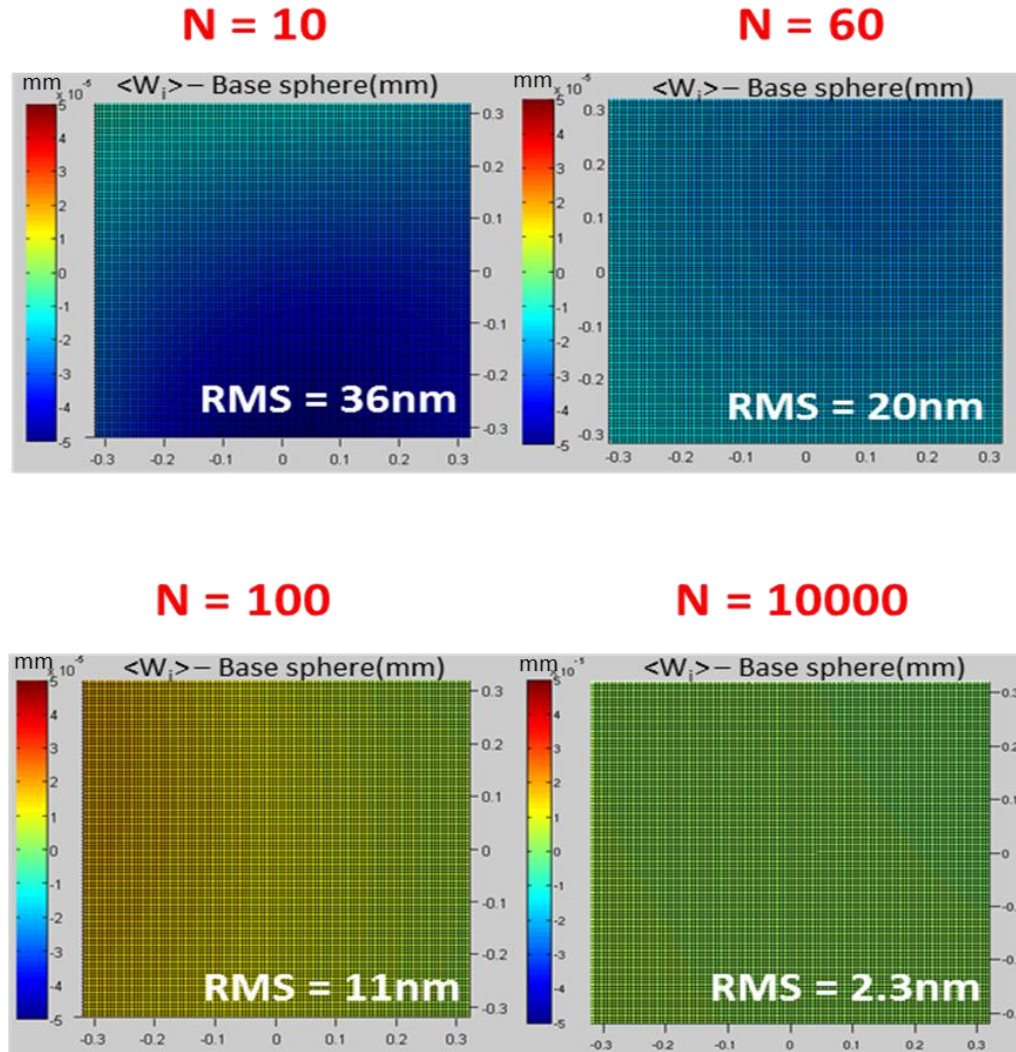


Figure 30: The residual ball error maps with different number of measurements,  $N$ . A realistic ball is simulated with error  $\text{RMS} = 100\text{nm}$  and  $R = 2\text{mm}$ . The field of view is  $0.64\text{ mm} \times 0.64\text{ mm}$ .

A repeatability test was carried out by simulating the RBT 1000 times at each value of  $N$ . Figure 31 shows the convergence of the residual RMS (RMS of difference between  $\langle W_i \rangle$  and  $W_{\text{base}}$ ) as a function of  $1/\sqrt{N}$ . A symmetric ball with RMS error  $\sigma_{\text{ball}} = 100\text{ nm}$  and  $R = 0.595\text{ mm}$  was used for this study. At  $N = 60$ , the residual RMS will be  $\sim 12\text{ nm}$  with uncertainty less than  $0.2\text{ nm}$ , which is negligible compared to other uncertainty sources during the experiment as discussed in Chapter 4.



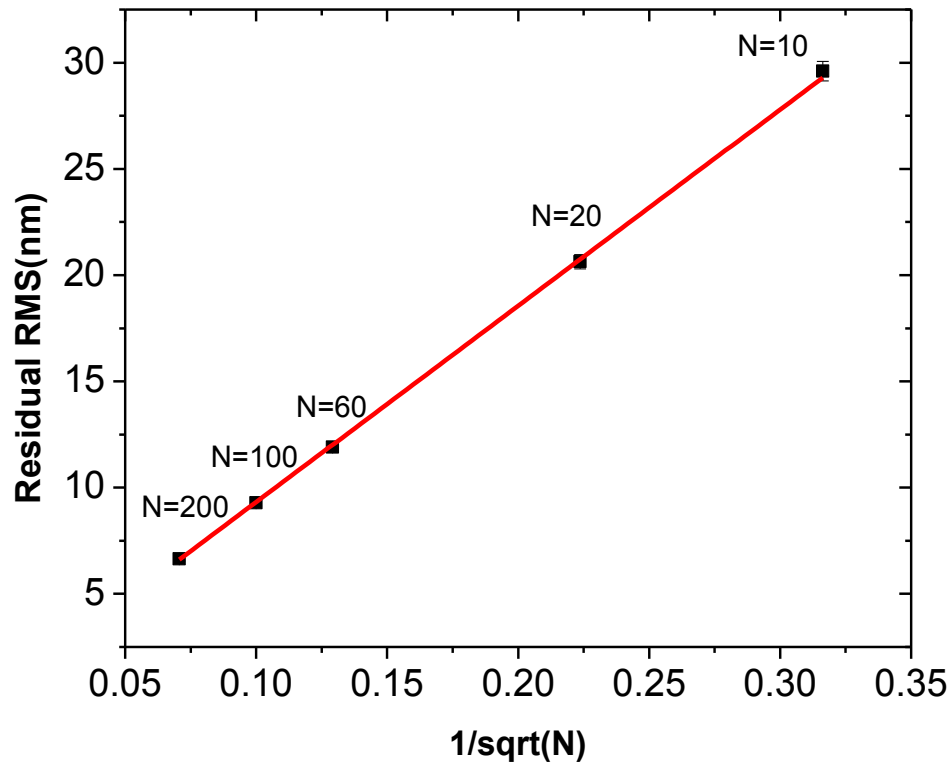


Figure 31: The residual RMS of the RBT as a function of  $1/\sqrt{N}$  where  $N$  is the number of measurements.

Another way to check the ball error convergence as a function of  $N$  is by comparing the best fit radius and base radius as discussed in 3.2. As was done for the residual error study, 1000 RBT were carried out for each  $N$ . With a large number of measurements, for example,  $N=400$ , the best fit radius converges to the base radius with a very small uncertainty, and vice versa, as shown in figure 32.

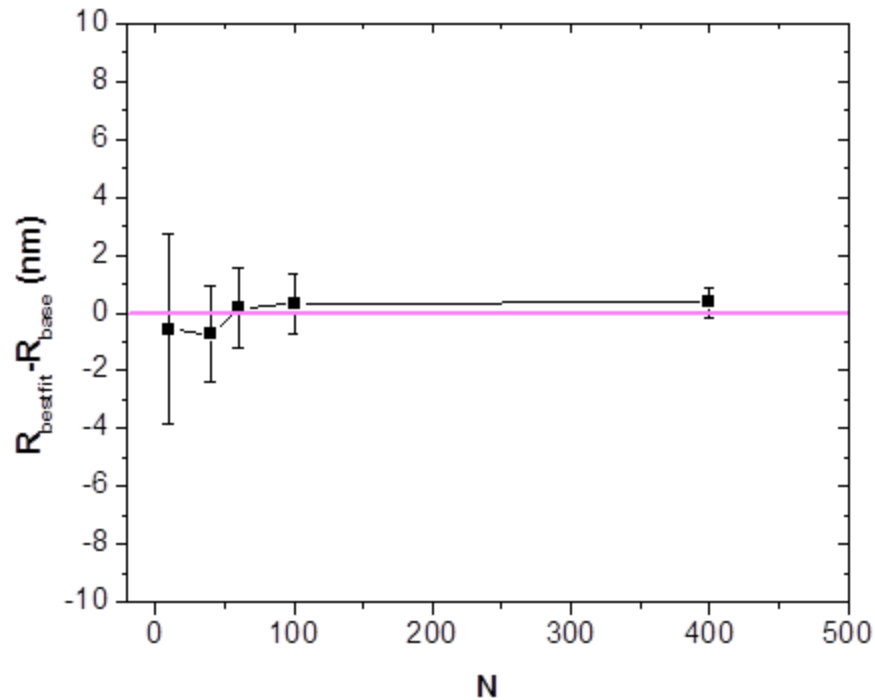


Figure 32: Radius difference between the best fit sphere and the base sphere as a function of  $N$ . The ball radius is  $R = 0.595\text{mm}$  and the ball error is  $\text{RMS} = 100\text{nm}$ .

The simulation results allow us to test the convergence speed of the RBT for profilometry calibration. As a guideline, a low uncertainty level will be reached with a small residual RMS error by averaging a relatively larger number of patches.

### 3.4 Ball Positioning Study

A ball has a natural range of slopes over the field of view. It is intuitive to take advantage of this to explore slope-dependent errors in a profilometer. Repetition of the RBT at multiple positions over the field of view provides this information, as shown in figure 33.

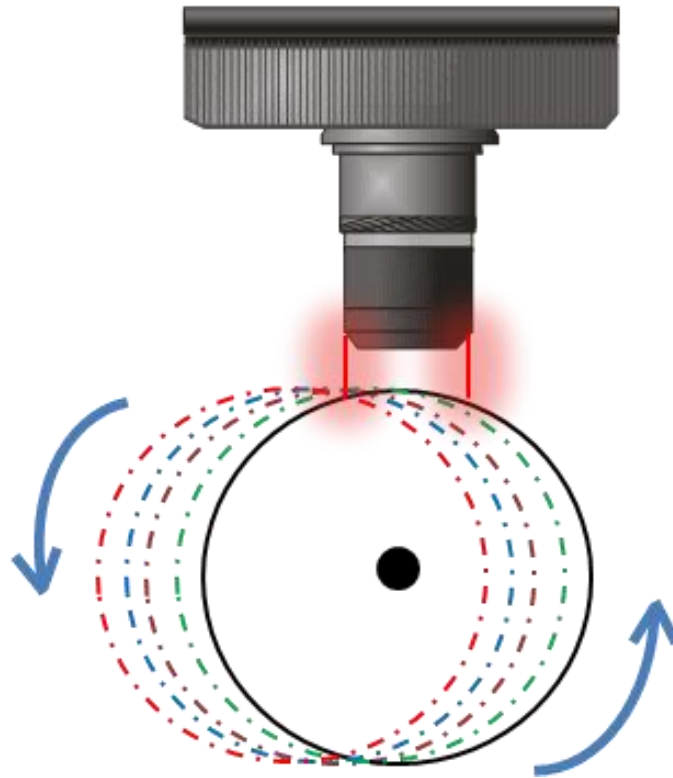


Figure 33: A schematic setup of RBT at different positions under the field of view for the ball off center study.

In the simulation, a realistic ball with  $\sigma_{\text{ball}} = 100 \text{ nm}$  and  $R = 0.595 \text{ mm}$  was placed at five different positions under a field of view equivalent to a 50X Olympus LSCM objective field of view (0.256mm by 0.256mm): 0  $\mu\text{m}$  (centered), 100  $\mu\text{m}$ , 200  $\mu\text{m}$ , 300  $\mu\text{m}$  and 400  $\mu\text{m}$  off center. Each ball patch profile is shown below in figure 34. Clearly, as the ball is moved further from the center of the field of view, a surface with large slope angles can be expected. For example, a 400  $\mu\text{m}$  off-center ball will bring the surface slope up to 57 degrees at the right edge of the field of view.

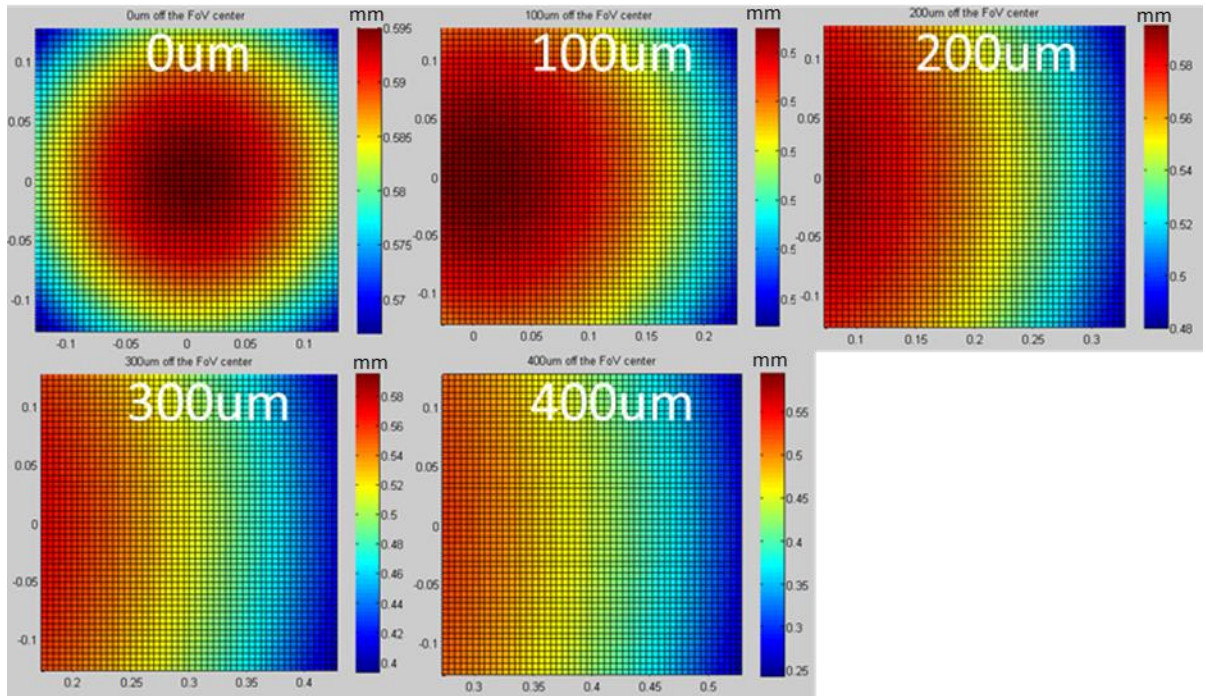


Figure 34: Ball patch profiles at different positions under an Olympus LSCM 50X objective with  $R = 0.595\text{mm}$ .

The RBT at each position was run 100 times, and each RBT contained  $N = 10000$  patch measurements. A comparison between best fit radius of  $\langle W_i \rangle$  and base radius is plotted in figure 35. The best fit radius converges to the base radius, and the ball errors average out. Thus, we conclude that the ball position under field of view does not impact the validity of the RBT result. Thus, repetition of the RBT over the field of view will provide adequate slope variation to allow us to explore slope-dependent biases in profilometry.

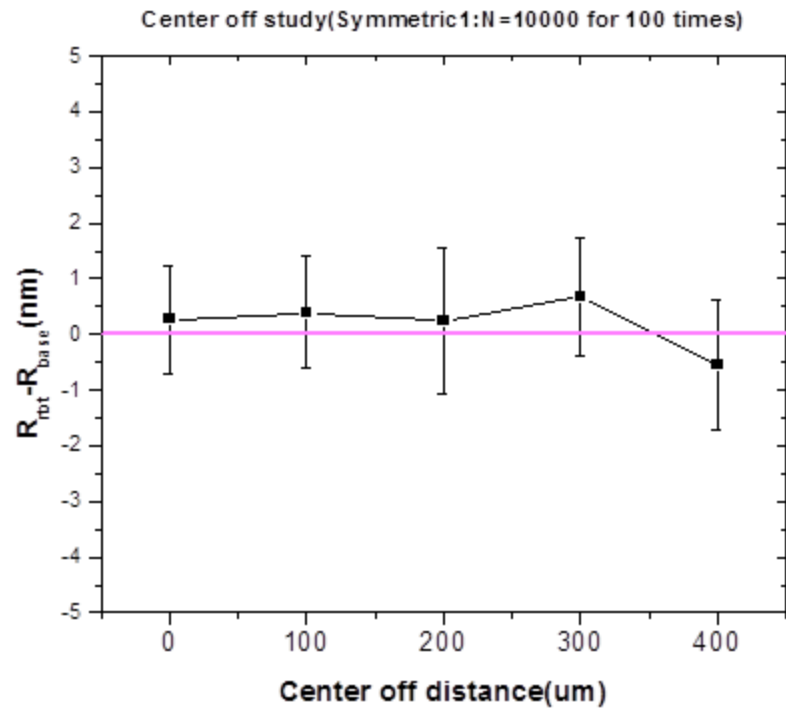


Figure 35: The difference in the best-fit radius to the RBT result compared to the base radius when placed ball at different positions under field of view.

### 3.5 Distortion Effect Study

In a perfect optical system, every point on a three dimensional object can be perfectly imaged at its corresponding conjugate point in image space. However, this is never satisfied for a real optical system with spherical optics like a traditional lens. The departure from an ideal imaging point is known as aberration. There are five basic types of monochromatic aberrations or called third order Seidel aberrations: spherical aberration, coma, astigmatism, field of curvature and distortion [70]. As shown in figure 36.

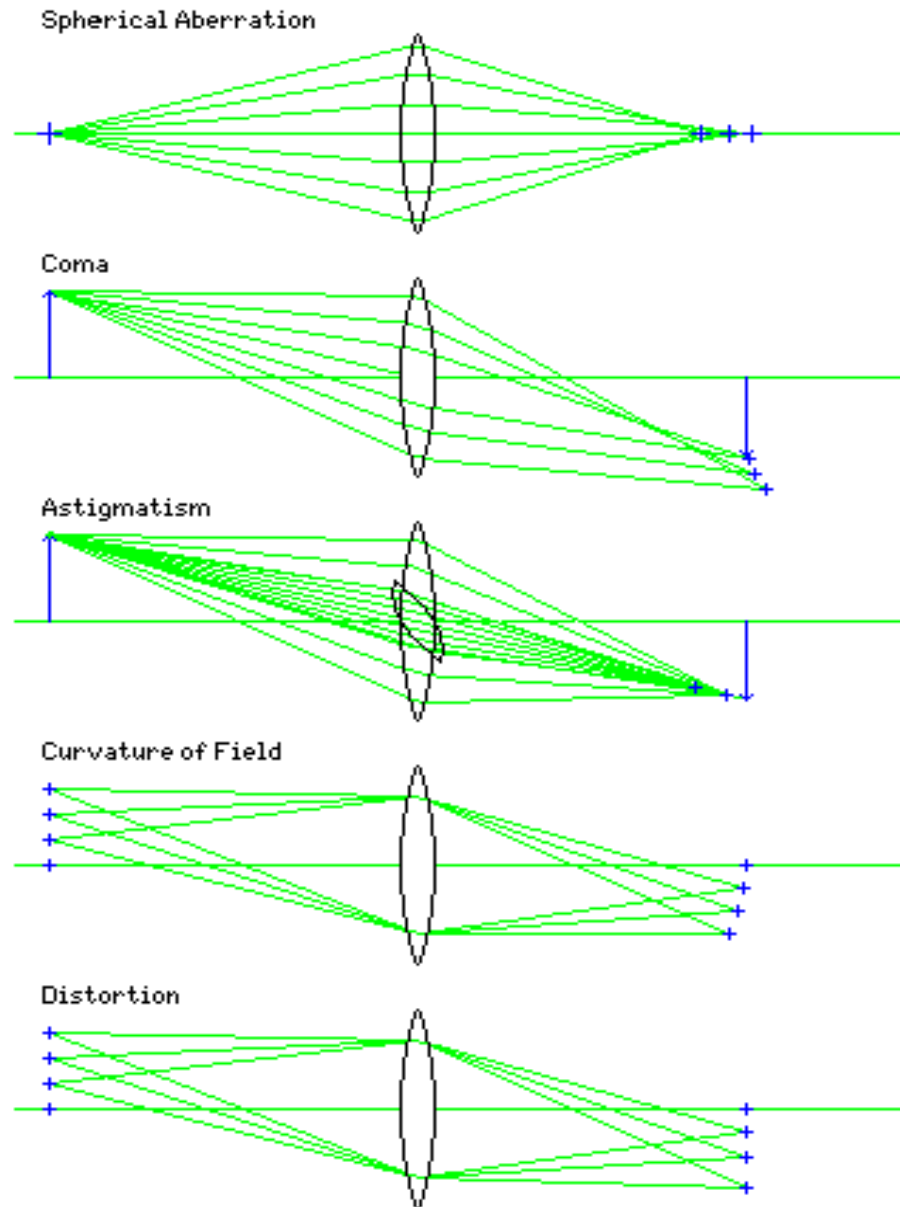


Figure 36: Ray tracing diagrams of five Seidel aberrations [67].

Spherical aberration is due to the relative increase (or decrease) in refraction of light rays when incoming light strikes a lens or reflected from a mirror near its edge. This produces a range of focal points along the optical axis which results in a blur image. A lens combination or an achromatic doublet is often used for correcting this aberration. Coma is generally encountered with off-axis light rays, and is the condition where the

rays are not quite converged at the focal plane and intersect an image plane, making a shape that looks like the profile of a comet. It can be reduced by limiting off axis rays or with the proper placement of an aperture stop and the proper multi-optic elements design. Astigmatism causes rays that propagate in two perpendicular planes to have different focal lengths. Astigmatism is minimized with the design of the optical system and appropriate lens shapes and indices of refraction [71]. Curvature of field aberration means that a flat object is not imaged at a flat image plane and is due to the curved surface geometries in the optical system. This aberration is often considered and corrected along with the correction of astigmatism. Distortion is because the transverse magnification is a function of the off-axis image distance. Distortion leads to a magnification change in the radial direction of the image plane. It is classified as positive (so-called pincushion distortion) or negative (so-called barrel distortion).

It has been reported that distortion can cause a systematic bias for a sloped surface measurement by a profilometer [72, 73]. For a 3D profilometry measurement, if distortion exists in the system, height errors will be introduced due to radial magnification change as shown in figure 37. The radial position variables  $r$  and  $r'$  are the object and image radial distance from the center field of view, respectively,  $\Delta Z$  is the deviation in terms of height difference. Therefore, distortion must be considered in the context of the RBT calibration. As will be discussed below, our calibration method in principle calibrates the errors caused by distortion with other slope-dependent errors. But, it can cause a bias in the calibration when the ball is off center and therefore needs to be considered carefully, as discussed below.

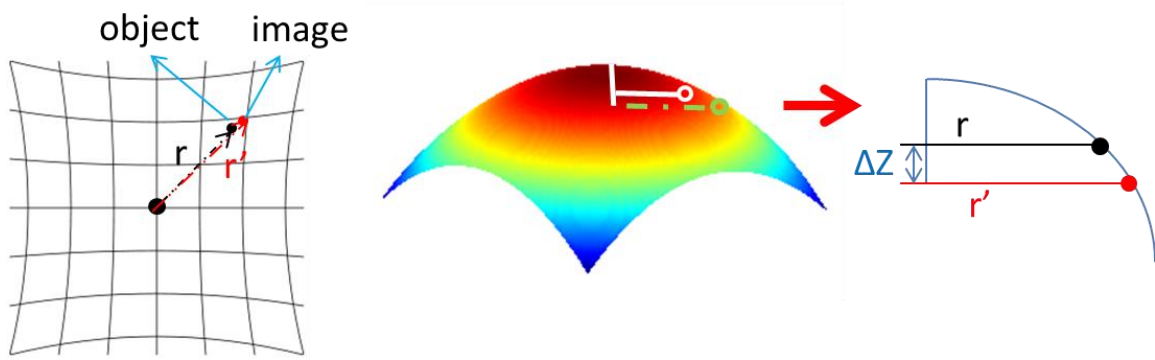


Figure 37: Optical distortion caused height error in a profilometry measurement: pincushion distortion(left); height error of surface profile due to distortion(right).

### 3.5.1 Distortion Detection

A cross grating artifact is often used for distortion calibration [74]. Distortion can be quantified by measuring the positions of the cross grating's squares, and the distorted image point then can be calculated by the equation [75-77]

$$r' = r + k_1 r^3 + k_2 r^5 + k_3 r^7 + \dots \quad (3.12)$$

where  $r'$  is the distorted radial distance from the center,  $r$  is the actual distance, and  $k = [k_1, k_2, k_3, \dots]$  is a vector of distortion coefficients.

For our calibration procedure, we need an estimate of the amount of distortion in the optical profilometer's imaging system. We estimated this for the system on which we demonstrated the calibration procedure by measuring such a cross grating artifact. We used a 10  $\mu\text{m}$  pitch and 100 nm heights cross-grating artifact for our distortion measurement and measured the surface with the Zygo Newview 5000 SWLI configured with a 50X Mirau objective. A 3D profile of the cross grating was taken, then a different region of the cross grating was captured by moving it under the field of view. During the moving process, a square is always positioned at the center by using a cross hair in order to keep a constant distortion at each square's location. In this way a collection of



measurements can be averaged to provide a better estimate of the amount of distortion.

The centroid of each square was calculated by Matlab, as shown in figure 38.

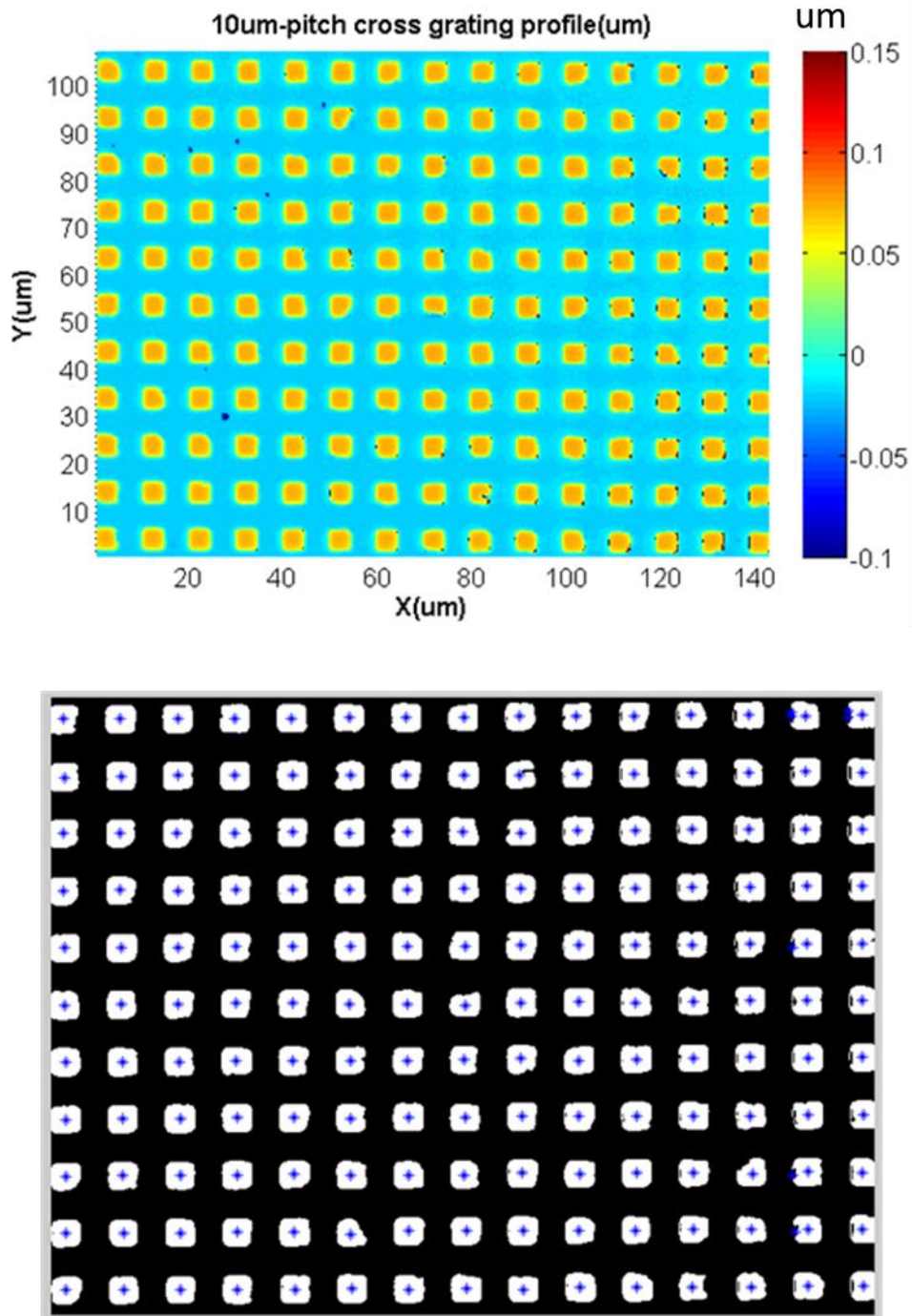


Figure 38: Distortion calibration on a the Zygo Newview 5000 with the 50X Mirau objective by using a cross grating. 3D profile of cross grating (above); centroid detection of the squares done in Matlab (below).

A quick estimate of the distortion coefficients following equation 3.12 is done by finding the distance from each centroid to the center field of view  $r'$ , as the actual distance  $r$  can be counted by the number of squares times the calibrated square spacing. Here we extracted the middle row and column to accomplish this task. Care should be taken when obtaining each centroid's coordinates since the imperfections of the artifact can create large unwanted errors in the centroid locations (as shown in figure 38, some ununiformed squares have multiple centroids detected). A separation distance between two adjacent squares as a function of each square's location is represented as a red bar distribution in figure 39. The error bar is the standard deviation of 10 separations from 10 different profile measurements. The X direction has more squares than the Y since the detector is a rectangular area. If there is obvious distortion, one could expect a "U" or flipped "U" shape to the top profile of the bars. For our calibration result, there is no clear distortion effect. The standard deviation in the middle row (X) is  $\sigma_x = 0.157$  pixels, and the standard deviation in the middle row (Y) is  $\sigma_y = 0.175$  pixels.

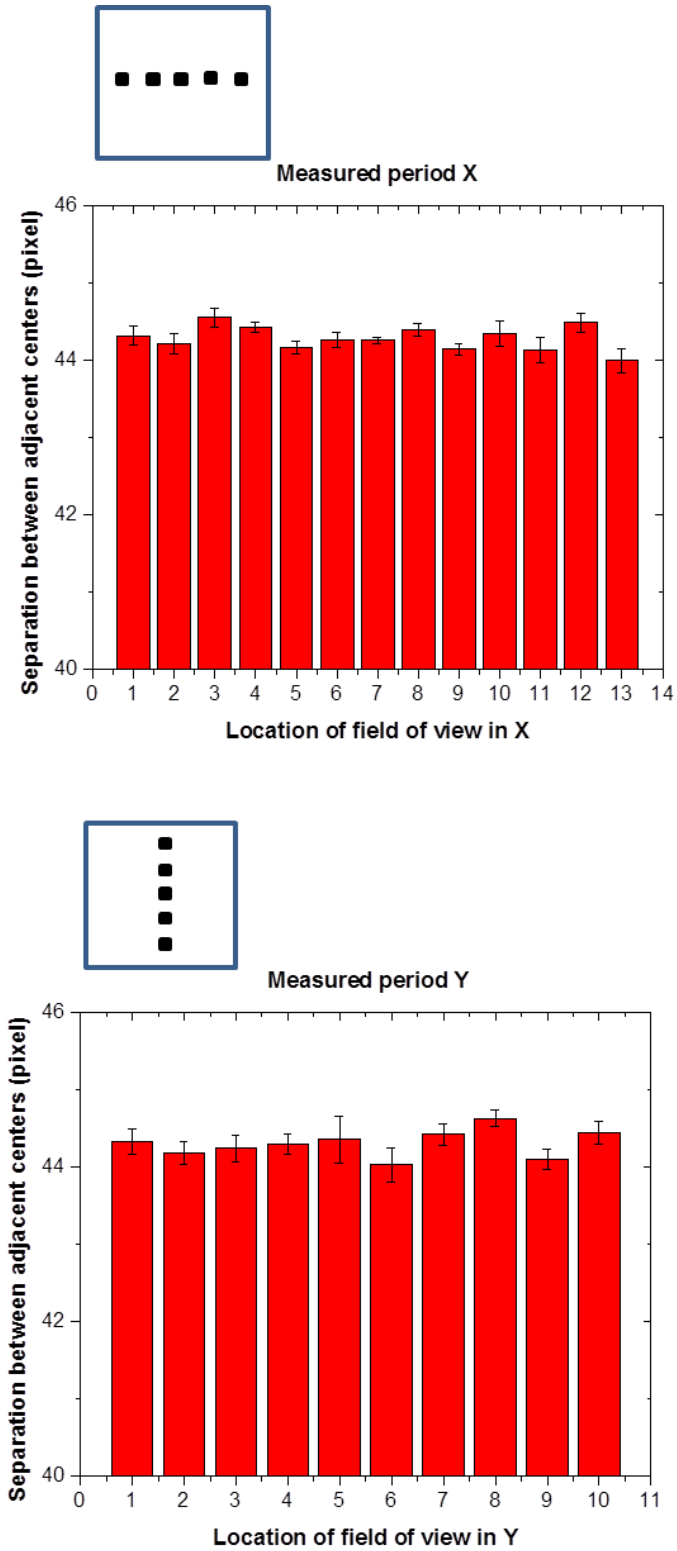


Figure 39: Distortion calibration result. The separation of adjacent squares from the cross grating in the middle row (X) and column (Y) was plotted as a function of the square's location.

### 3.5.2 Distortion Effect On RBT

Although no measurable distortion was found in the measurements carried out on a profilometer system discussed above, the uncertainty in the measurement provides a bound to explore in simulation to assess the impact of possible distortion on the calibration result. We begin with assuming the presence of 1 pixel of distortion and explore the impact on the RBT. As discussed in the previous section 3.5.1, distortion can be described by equation 3.12. To simplify the model, we only consider the first and the third order term with distortion coefficient  $k_1$  and neglect the higher order terms, thus the simplified distortion model becomes

$$r' = r + k_1 r^3 \quad (3.13)$$

For a 50X objective of LSCM, with field of view of 0.256 mm by 0.256 mm, the pixel size is 0.25  $\mu\text{m}$ , and 1 pixel distortion gives  $k_1 = 0.0596$ , which means 0.25  $\mu\text{m}$  distortion can be expected at the four corners. Including this amount of distortion, when a perfect ball with radius  $R = 0.595$  mm is centered, and no other error source was provided, after a RBT with  $N = 1000$ , distortion causes height error map is shown in figure 40. The center of the error map has a slope of zero, and the slope angle increases going out from the center. Distortion error is clear slope dependent bias with a PV = 113 nm. Thus, for the ball centered in the field of view, the RBT calibration procedure will correctly calibrate the slope dependent errors in the measurement. When the ball is off center in the field of view, distortion can cause an error in the calibration procedure and has to be considered with care. This is described below.

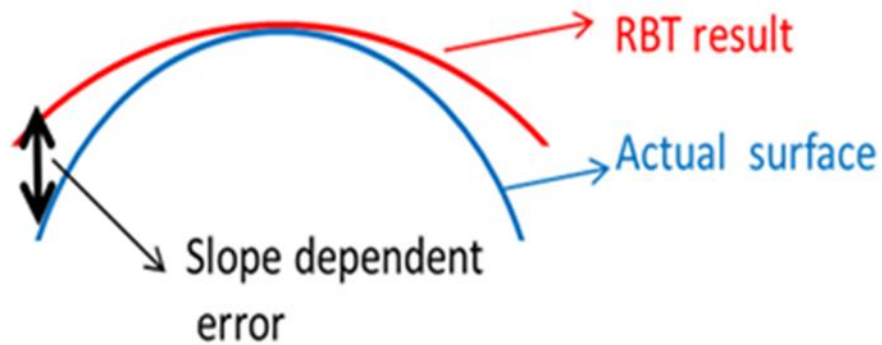
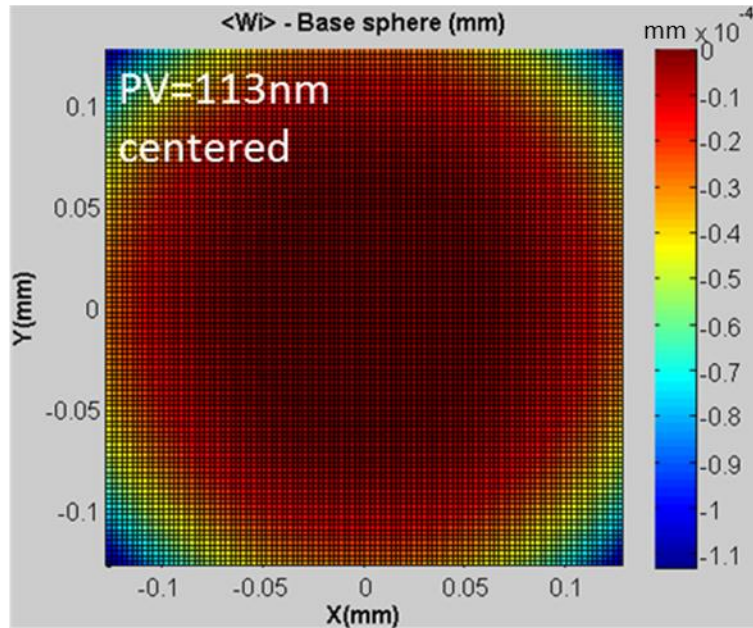


Figure 40: Slope-dependent distortion error observed when RBT is performed with  $N=1000$  centered under the field of view. A perfect ball with  $R=0.595\text{mm}$  is used for the RBT.

The position of base sphere in the field of view plays an important role for the RBT, especially when the RBT is performed off center. The calibration procedure relies on being able to subtract the nominal shape of a perfect ball from the averaged result. This means the position of the ball has to be estimated to position the nominal shape for the subtraction. There are two options we can use to determine the base sphere's position, one is the best fit center of the RBT result  $\langle W_i \rangle$ , by using the robust best fit algorithm as

described in section 3.1.3. The other option is to use the encoder readings of the stage position, if provided by the instrument. When the ball is centered, there is only a possible Z difference for the center of the base sphere, as distortion will not cause a lateral shift for the best fit center. However, if distortion exists in the system, it will break the geometric symmetry of the surface profile when the ball is positioned off center, and this will cause the best fit center to deviate in all three dimensions, x,y, and z. Therefore, it is critical to decide which position one should use for the base sphere subtraction. To study this effect, distortion error maps were generated by using two different base sphere positions, as shown in figure 41 and 42. Four positions of the RBT are shown here, 50  $\mu\text{m}$ , 100  $\mu\text{m}$ , 200  $\mu\text{m}$  and 250  $\mu\text{m}$  off center of the field of view. The base sphere has a radius of  $R = 0.595 \text{ mm}$ . Figure 41 uses the best fit center as the base sphere's position for the subtraction. On the other hand, figure 42 uses the known position of the center for the subtraction.



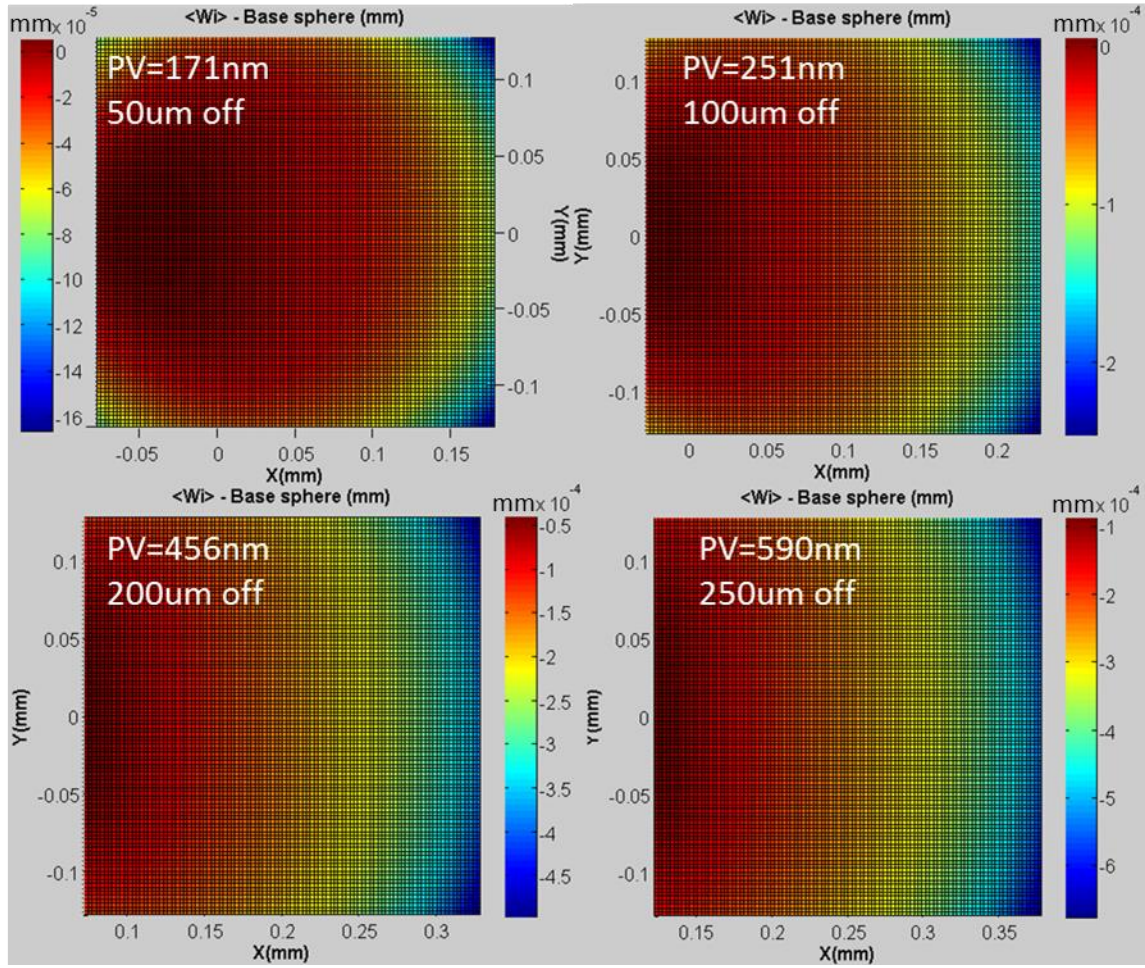


Figure 41: Error maps by using the best fit location for the base sphere subtraction with a distortion model having 1 pixel of distortion at the edge of the field of view. A ball with radius of 0.595 mm is placed at different positions over the field of view.

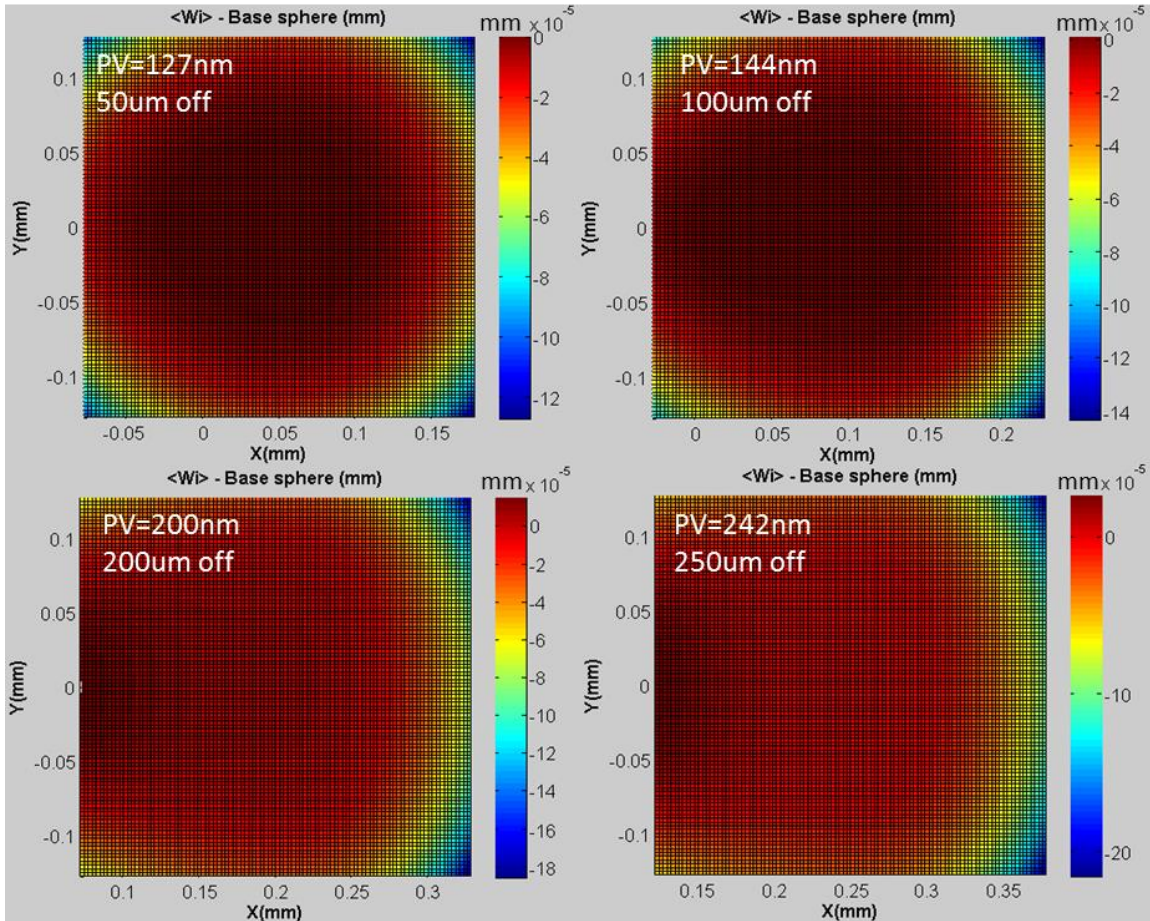


Figure 42: Error maps by using the known (exact) location for the base sphere subtraction with a distortion model having 1 pixel of distortion at the edge of the field of view. A ball with radius of 0.595 mm is placed at different positions over the field of view.

Comparing figure 41 and 42, a larger height error caused by distortion is observed when using the best-fit to determine the position for subtraction compared to the using the known position. All error maps show again that distortion leads to height errors that are slope dependent. One way to visualize this is to plot the height errors as a function of slope angle for different positions in the field of view. The data obtained from the RBTs carried out at the different locations can be regrouped to do this by taking advantage of the slope information over a ball patch at the different ball locations over the field of view. A series of RBTs was carried out with the ball positioned at 0  $\mu\text{m}$ , 50  $\mu\text{m}$ , 100  $\mu\text{m}$ , 150  $\mu\text{m}$ , 200  $\mu\text{m}$  and 250  $\mu\text{m}$ . As shown in figure 43, four fixed pixels over the field of



view were used and for each of the four pixel locations, the result of the 6 RBTs leads to a range of 6 surface slope values for which there is a height error. So, each fit line corresponds to six values for a fixed pixel, and represents height error variation due to slope angle change only (no field of view effect is taken into account).

One can see that, at each of the four locations, a surface slope of zero leads to zero height error and this is expected since a step height with zero slope is used for the profilometer calibration. The curves when the correct ball position is used for the subtraction have the expected behavior, that is the slope-dependent bias (the effects caused by distortion) are larger as the slope increases and the location in the field of view is larger (distortion increases with distance from the center of the field of view). When the best fit sphere is used to determine the ball position in the field of view, the predicted height errors are too large.

But notice that even though distortion leads to incorrect height errors when the best-fit sphere is used to determine the ball location, the scale of this is small. In the experiment carried out to estimate the distortion, no measurable distortion was found. If we take the standard deviation of the middle row (X) of  $\sigma_x = 0.157$  pixels, and the standard deviation of the middle row (Y) of  $\sigma_y = 0.175$  pixels, as an upper bound for the maximum distortion offset at the edge of the field of view, the simulation predicts that using the best-fit sphere to determine the sphere location leads to an error in the calibration of at most 4.3 nm at the edge of the field of view. This is much smaller than the systematic bias observed in the experiment and therefore can be ignored. This is good because knowing the location of the ball is important and having to rely on encoder readings and counting on low drift rates in the instrument would not be practical due to

the variation of drift from time to time. Using the best-fit sphere to determine the ball position is the easiest and most practical approach. The impact of instrument drift on the calibration process is discussed next.

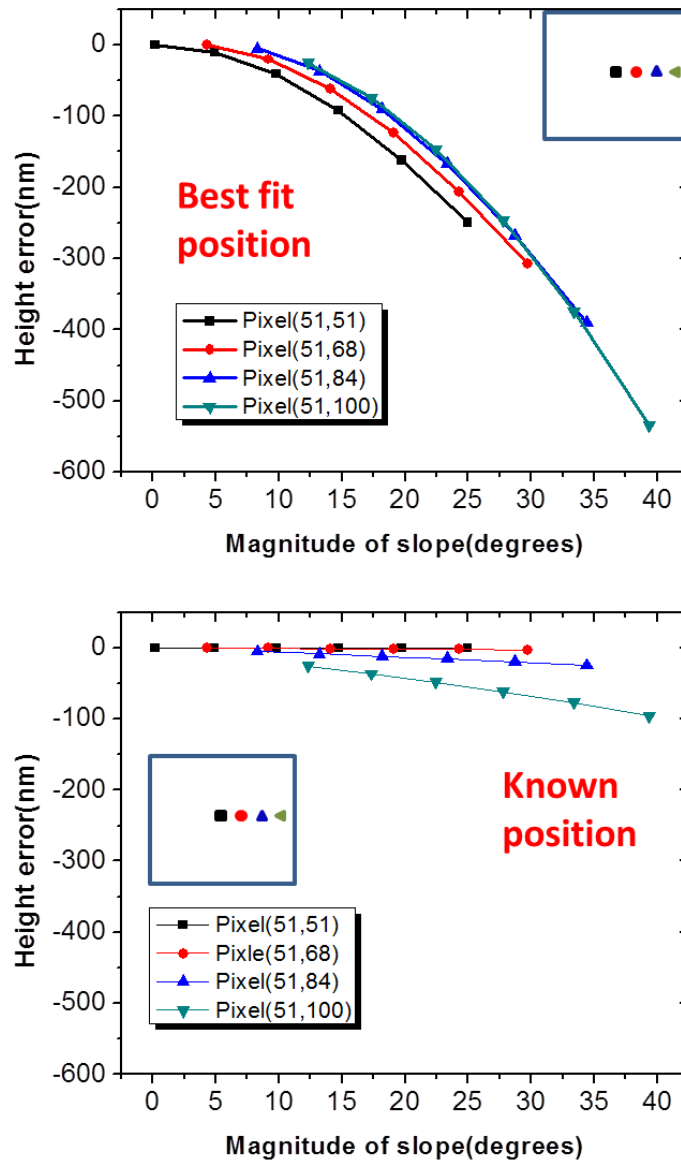


Figure 43: The apparent height error caused by distortion when using two different ways of determining the position of the ball: use of the best fit sphere to determine location (above); use of the exact (known) location (below).

### 3.6 Drift Effect Study

Drift is a common and inevitable error source in measurements. Stage drift during profilometry measurements causes errors in the height and x y mapping of the height data. Stage drift has long been a limiting factor in tracking micro features of surfaces during a scanning process [78]. For sequential frame data acquisition, drift will lead to a mismatch between subsequent measurements. Thus, drift consideration is important.

We use simulation to investigate the impact of drift on our calibration procedure. For this study, we simulate a perfect ball with a base radius of 0.595 mm, and add drift rates of  $d_x = -100$  nm/min in the X direction and  $d_y = 50$  nm/min in the Y direction. These are values that match what are observed (in section 4.3.2.3) in the confocal microscope used for this study. The ball starts at the center of the field of view. It is displaced after each simulated measurement using the above drift rates and a 1 minute time interval (to match experimental conditions). After a full RBT with  $N = 100$ , a ball error map is generated. Figure 44 is the resulting error map by using the best fit position for the base sphere subtraction (there is no distortion in this study). The error map is very small with a  $PV = \sim 1$  nm. In contrast, if we had used a fixed position at the center of the field of view for the base sphere subtraction, effectively not taking the drift into account, the height error map would have been extreme and very misleading with a PV up to 3  $\mu\text{m}$ . Therefore, drift must be considered in the calibration procedure and the impact is minimized by using the best fit center to position the base sphere for subtraction.

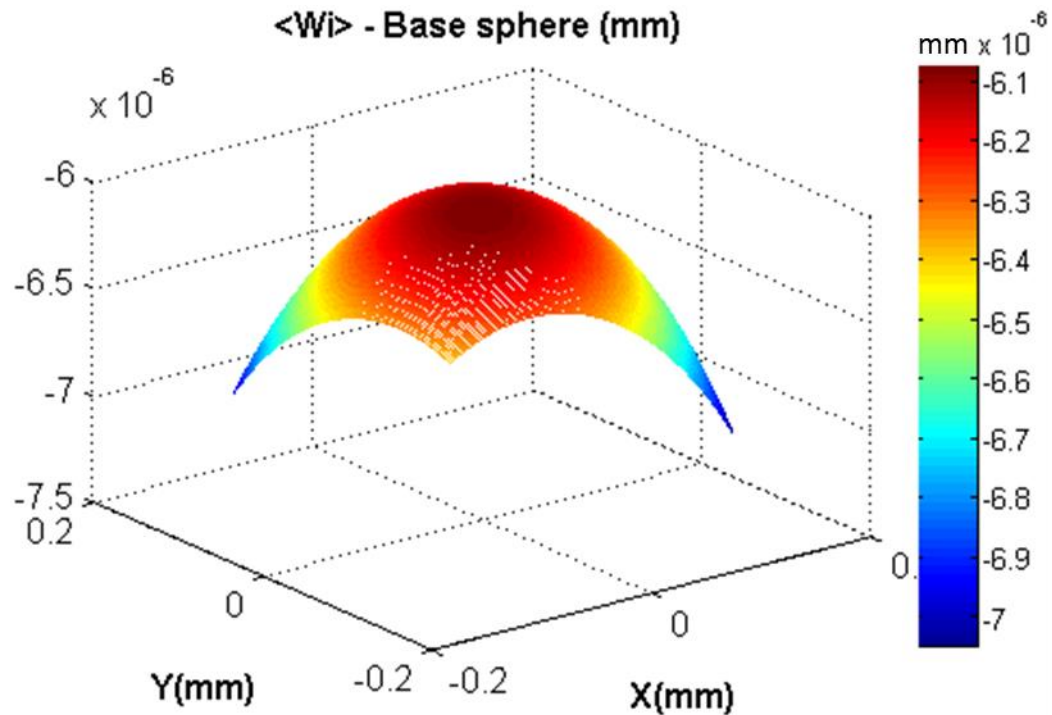


Figure 44: Height error map in the presence of drift when using a best fit center to determine the location of the base sphere for subtraction.

In the simulation there is no error source such as an instrument systematic bias, random noise, misalignment, etc., so it allows us to clearly test the fundamental validity of the approach. The simulation studies show that the only factor to consider is the asymmetry of the ball error distribution. It can lead to a best-fit radius error of the average that can be as large as 55 nm for a ball with an RMS geometrical error of 100 nm and a radius of 0.595 mm. But, this amount translates to a sag artifact in the calibration result of only 2.8 nm. This is very small compared the instrument biases we see in the calibration results discussed below. It is also very small compared to the repeatability of the calibration result [79]. We thus conclude that the RBT is a valid calibration technique when applied to typical optical profilometers such as the SWLI and the confocal

microscope. We have applied the RBT calibration to two commercial optical profilometer, and these results are presented in the next chapter.

## CHAPTER 4: RBT EXPERIMENTAL RESULTS

We applied the RBT to both a SWLI and a confocal microscope to demonstrate the effectiveness of the effectiveness of the approach and to assess the order of magnitude of slope-dependent errors one might expect for such instruments.

### 4.1 Setup for the Calibration

In a RBT calibration, reorienting the ball is critical. Different methods can be used to accomplish this task. For example, it can be implemented by setting the ball on a three point mount and rotating it manually after each measurement [26], however, contamination of the ball surface and possible reposition bias by one's hand would make the calibration susceptible to errors, not to mention the operator's tedium for a large number of measurements. A ball manipulator developed by NIST solves this manual problem and consists of two motion controllers and a radius matched spherical air bearing. The setup can reach a standard positioning uncertainty of 0.5 degrees for a 360 degree rotation [65]. A more elaborate motion control setup for ball rotation is described in the patent literature by Evans et al [80]. But, these testers are limited to a small size ball, e.g.  $R = 0.595$  mm. Therefore, we need a robust way to reposition the ball with low uncertainty as well as ease of use.

In our setup, the ball is positioned in the instrument on a sheet of shim stock that is sandwiched between two rings. There is an indentation in the middle of the shim, and this is where the ball settles. The indentation provides a reproducible position for the ball, as

shown in figure 45. The orientation of the ball is randomized between measurements with a puff of air that dislodges the ball. A repeatability test shows that the misalignment of the ball in all three directions due to the setup is less than  $10\ \mu\text{m}$



Figure 45: Ball holder for the RBT. Two big washers sandwich a sheet of shim, and an indentation is used for positioning the ball.

#### 4.2 Ball Radius Measurement

The properties of the calibration ball play an important role in reaching the desired calibration range and uncertainty. The slope range of interest for a given field of view sets the choice in ball radius. In some cases the working distance of the instrument should also be considered. For the calibration results presented below, we used a grade 3 440-steel ball with a radius of  $R = 0.595\ \text{mm} \pm 0.0005\ \text{mm}$ . The radius was

mechanically measured with an upgraded Mahr MFU7 form measuring machine in a standard metrology laboratory at UNC Charlotte. Since the ball is small, great care was taken to position it between the two gage planes, and a small force was set to stabilize the diameter reading. The measurement was repeated 10 times, the average taken as an estimate of the ball radius, and the standard deviation divided by the square root of 10 used as an estimate of the standard uncertainty which is  $\pm 0.5 \mu\text{m}$ . A mechanical measurement at this level is reasonable, and it is sufficient to allow for a meaningful RBT result. This uncertainty could likely be reduced, if needed, with a more detailed uncertainty analysis of a ball radius measurement following NIST guidelines. Material property, force level, as well as environmental impact are counted in the analysis [81].

This radius provides a slope of  $\sim 12^\circ$  at the edge of the field of view when the ball is centered using a 50X (NA = 0.95) objective. The manufacturer, Bal-tec<sup>TM</sup>, reports a geometric error for the ball of an RMS = 100 nm.

#### 4.3 Calibration For Confocal Using RBT

We applied the RBT to the calibration of a LCSM (Olympus LEXT OLS4000) configured with a 50X objective, resulting in a field of view of 0.256 mm by 0.256 mm. The working distance for this objective is very small (0.35 mm) so care was taken to lower the stage for re-positioning the ball and then re-centering for each measurement.

In the experiment,  $N = 60$  measurements are taken. The scanner characteristics and drift lead to an arbitrary height offset between every measurement, and this is removed by adjusting the height of each profile, so they all have the same best fit center  $z$  coordinate. We then calculate the average  $\langle W_i \rangle$ , and fit it to a sphere with the robust sphere fitting algorithm to determine the best-fit center coordinates. We then subtract the



base sphere following equation 3.3, using the mechanically determined radius of the ball, to arrive at our estimate of the instrument errors over the field of view. The instrument was previously calibrated with a flat step height artifact, therefore, we adjusted the offset so that the region of zero slope corresponds to zero instrument error.

#### 4.3.1 Calibration Results For The LSCM

Figure 46 shows the resulting calibration error map for the LSCM with the 50X objective. It shows a clear instrument error that varies over the field of view and is strongly slope dependent. The error is zero in the middle where the ball is centered, and the surface slope is zero. The slope of  $12.1^\circ$  at the edge of the field of view shows a height error of  $\sim 800$  nm. This value indicates that the measured height at the edge is smaller than the true height of the surface by  $\sim 800$  nm. One could then use this instrument error map to correct each of the individual ball measurements. Or, for example, it could be used to correct a microlens measurement centered in the middle of the FoV with a similar base radius of curvature.

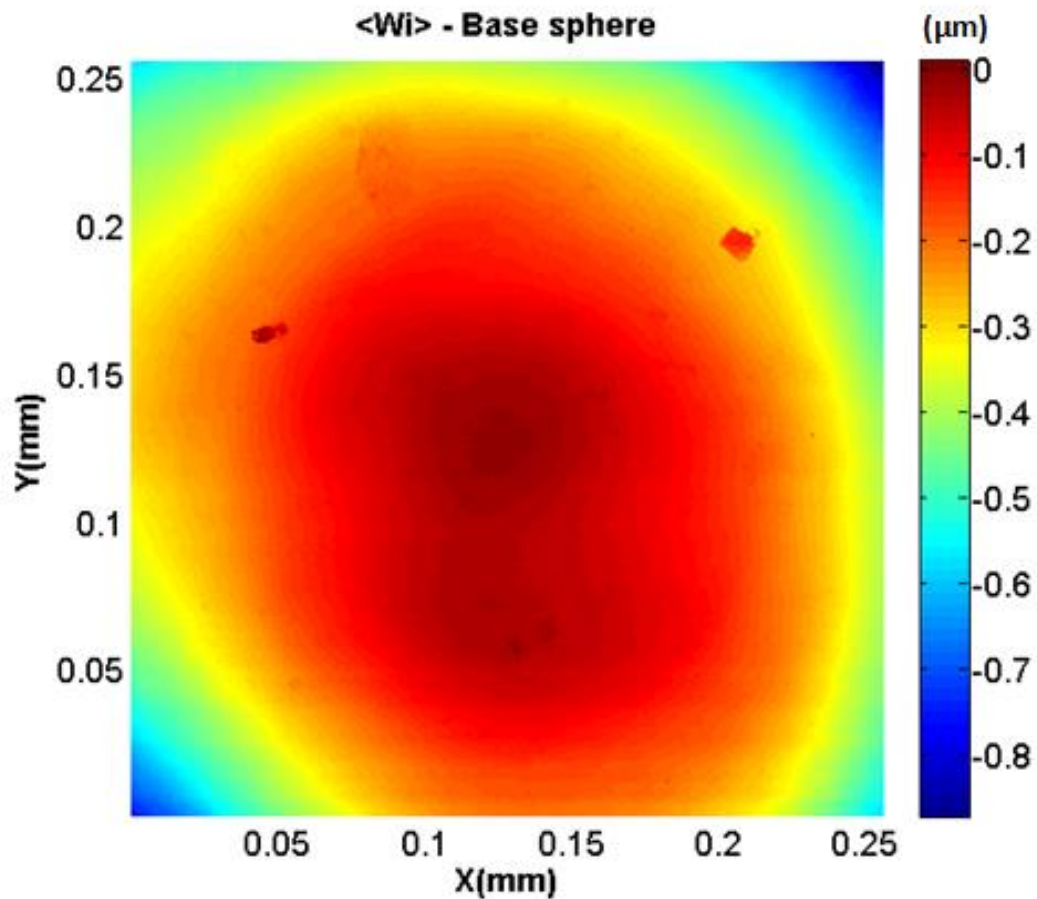


Figure 46: The RBT calibration result for a laser scanning confocal microscope configured with a 50X objective.

In order to explore a quantitative correlation between instrument error and slope as well as the field of view impact, five more positions in the horizontal direction were chosen for RBTs, at 100  $\mu\text{m}$ , 200  $\mu\text{m}$ , 300  $\mu\text{m}$ , 400  $\mu\text{m}$  and 500  $\mu\text{m}$  off center, respectively. However, when ball is placed at 500  $\mu\text{m}$  off center of the field of view, a region of strong noisy data is present at the edge, corresponding to region for which the surface slope of the ball is beyond the measurable slope range of the instrument, as shown in figure 47.

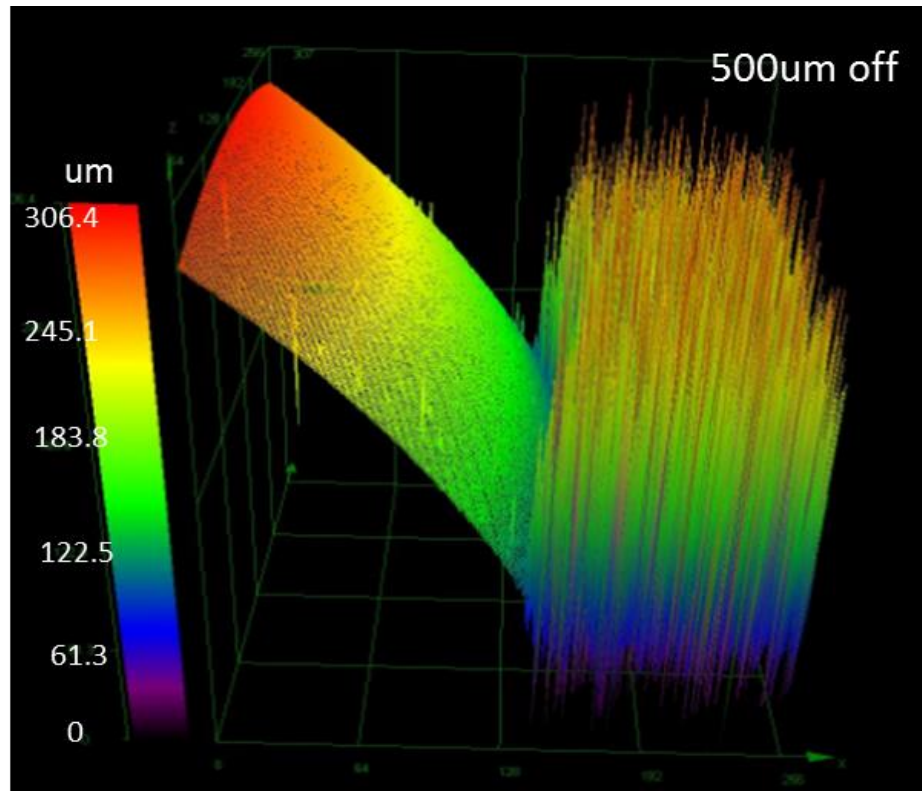


Figure 47: Surface profile of ball patch taken with the LSCM 50X when the ball is placed 500 um off center of the field of view. The noisy data appears beyond a surface slope angle of  $\sim 72$  degrees.

A calculation based on the ball surface geometry indicates that this slope angle is  $\sim 72$  degrees. Based on consideration of the NA of the objective and the surface slope maximum corresponding to an acceptable back reflection of the light cone, noisy data at this surface slope and beyond is expected. That is, a sloped surface at this angle is the boundary between specular reflection with mixed scattering and pure scattering, as illustrated in figure 48. The green dash line represents a slope angle of 72 degrees, and at this angle, the incident ray from the right edge of the objective will reflect back along the incident path, therefore, 72 degrees is the boundary for collection of the reflected rays. At this surface angle, the detector can receive a signal from scattered light but the surface angle is beyond the limit for a specularly reflected signal.

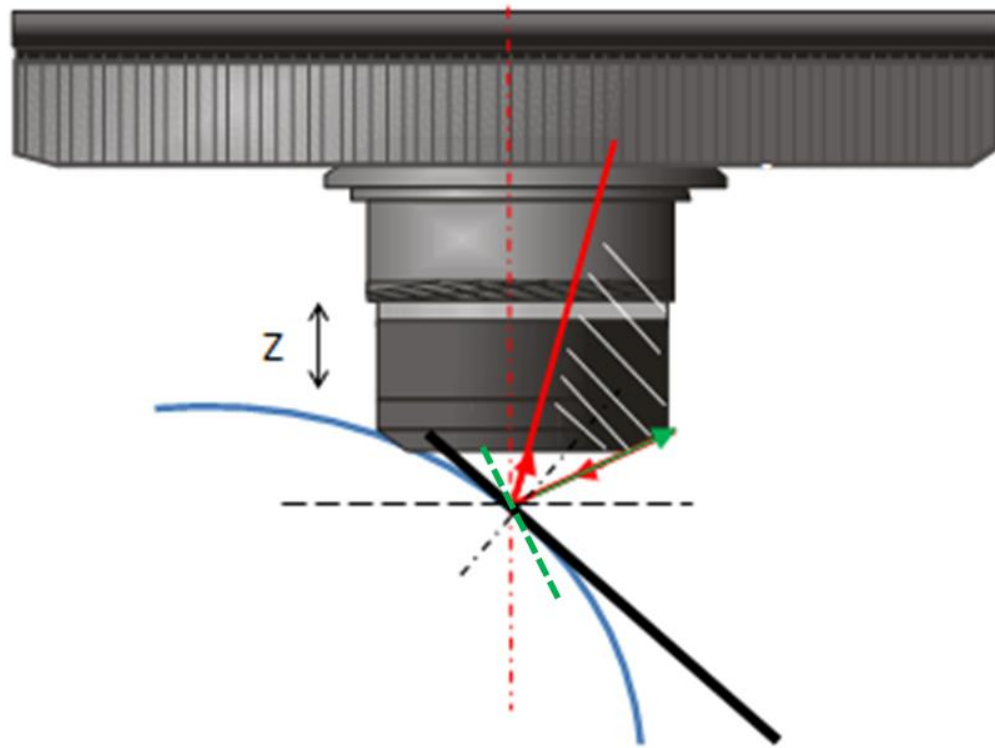


Figure 48: An illustration of specular reflection from a sloped surface.

Although one can obtain data if the surface slope is less than 72 degrees, reduced specular light and scattered light will bring noise to the detected signal. For a RBT, the geometry on every ball patch will be different as will the scattering properties, as a result, a large variation is expected. Figure 49 left is the surface profile when the ball is placed at 400  $\mu\text{m}$  off center of the field of view, and the right side of the figure is the standard deviation map of 60 ball patch measurements. One can see that the variation of 60 measurements at each pixel becomes noisy as the slope angle increases, and the biggest standard deviation is observed at the two corners of the map that correspond to the largest

slope angle.

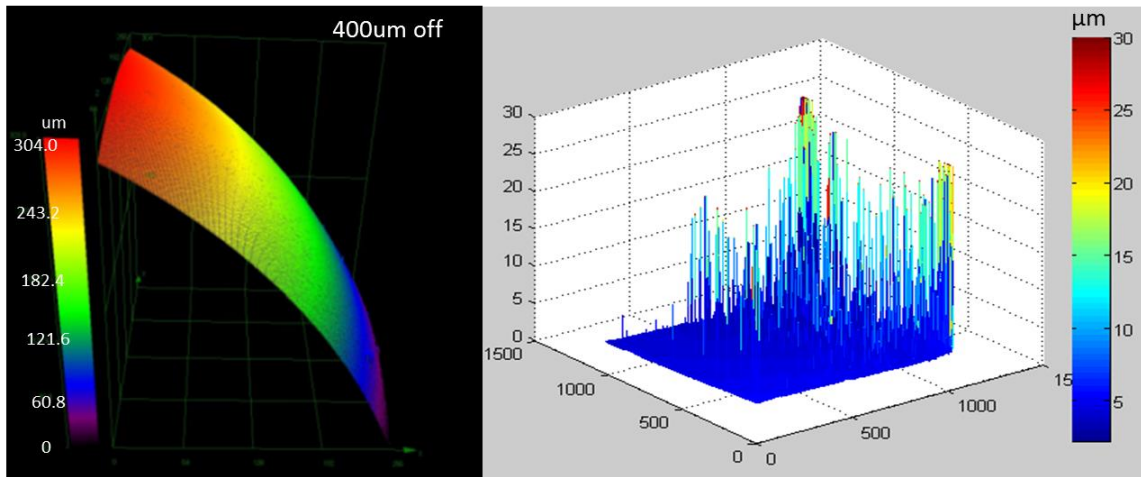


Figure 49: Surface profile of a ball patch at 400  $\mu\text{m}$  off center under a LSCM 50X objective (left). Standard deviation map of 60 measurements of the RBT when the ball is 400  $\mu\text{m}$  off center (right).

Therefore, the RBT result for the 400  $\mu\text{m}$  off center position and higher are not used for the calibration. Figure 50 shows the instrument error maps when the RBT was taken at 0  $\mu\text{m}$  (centered FoV), 100  $\mu\text{m}$ , 200  $\mu\text{m}$  and 300  $\mu\text{m}$  off center FoV in the horizontal direction. In order to reduce uncertainty, five circled regions consisting of  $\sim 30$  pixels are chosen to estimate the average magnitude of the systematic bias for each region. The centered pixel of each region is used to determine the magnitude of the surface slope angle by calculating slope angle between two adjacent pixels. The regions are 200 pixels apart.

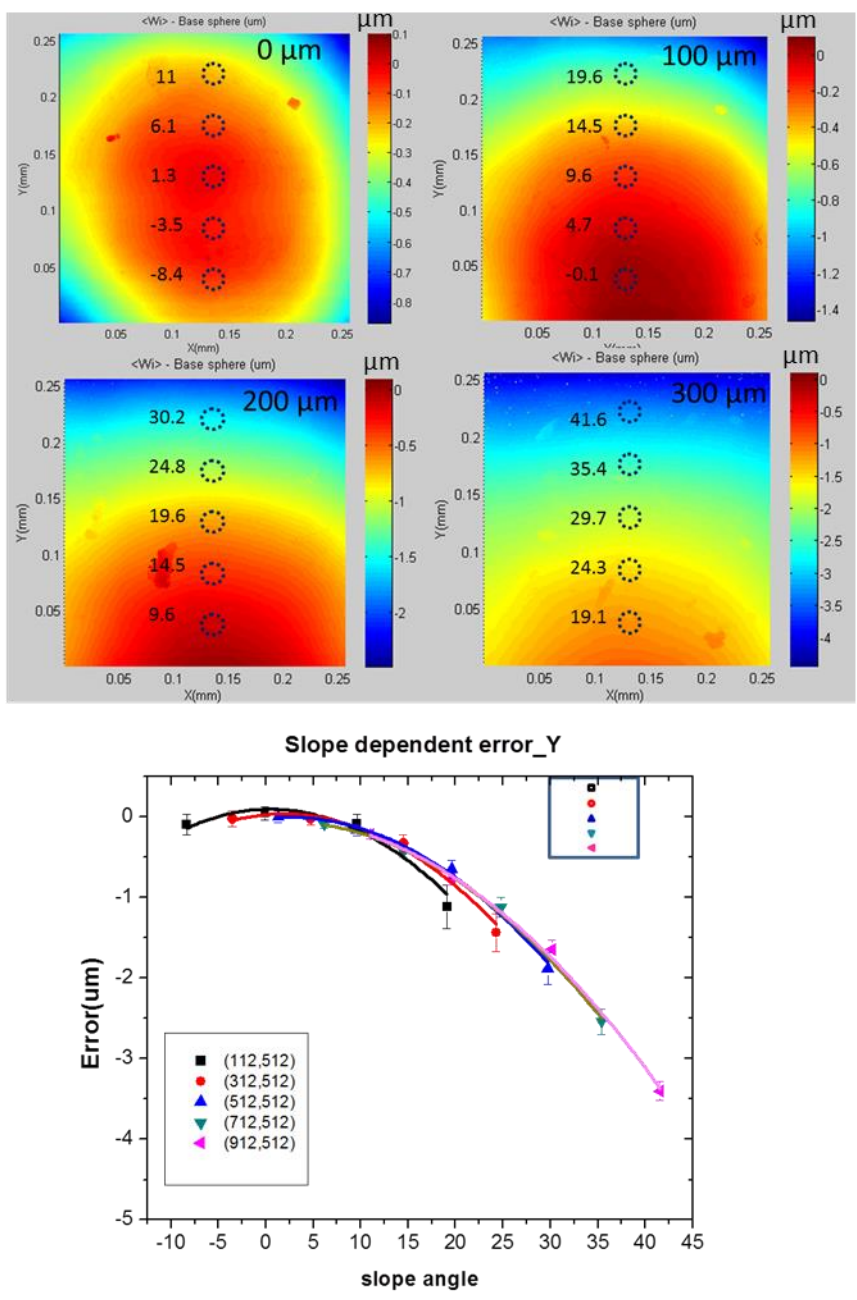


Figure 50: Error maps when the RBT was taken at four positions along the horizontal direction centered at field of view locations 0  $\mu\text{m}$ , 100  $\mu\text{m}$ , 200  $\mu\text{m}$  and 300  $\mu\text{m}$  off center. Each dashed circle (exaggerated) represents  $\sim 30$  pixels whose center was used for a slope angle estimation (number on top of each circle).

A FoV dependence on systematic bias is done by plotting 20 height error values (5x4) shown in figure 50 as a function of magnitude of slope angle. The result is shown in

figure 51, showing that the systematic error is clearly slope dependent and has a parabolic dependence on slope angle. Moreover, we see that there is little variation of the error over the field of view; that is, the bias is dominated by the magnitude of the slope angle, independent of location in the field of view. The error bar for each data point on the graph represents the standard deviation of 30 height error values within the circle, divided by the square root of 30.

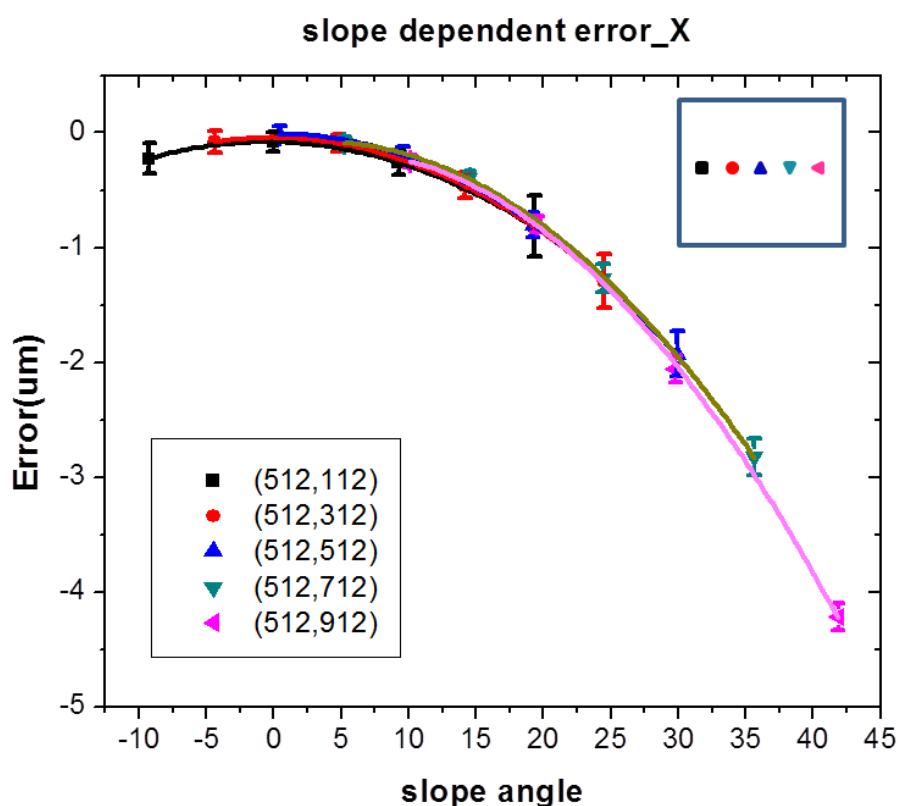


Figure 51: Systemic bias plotted as a function of slope angle for each error map in the horizontal direction.

To thoroughly explore the FoV dependence as well as the slope magnitude dependence, RBTs in the vertical direction (Y) were also carried out (similar to the horizontal (X) case). Four error maps are generated, and five circles are chosen to estimate the systematic error for this direction. Two adjacent pixels in the vertical

direction are used for determining slope angle. As shown in figure 52, slope angle is listed as the numbers on the left of each region. The height error is zero as long as the slope angle is zero. Positive and negative signs of the slope represent the different orientations of the slope. Again, the systematic error is plotted as a function of slope angle for each map, and the same conclusion can be drawn. Namely, the field of view location has little impact on the systematic bias, rather the bias depends on the magnitude of the surface slope angle.



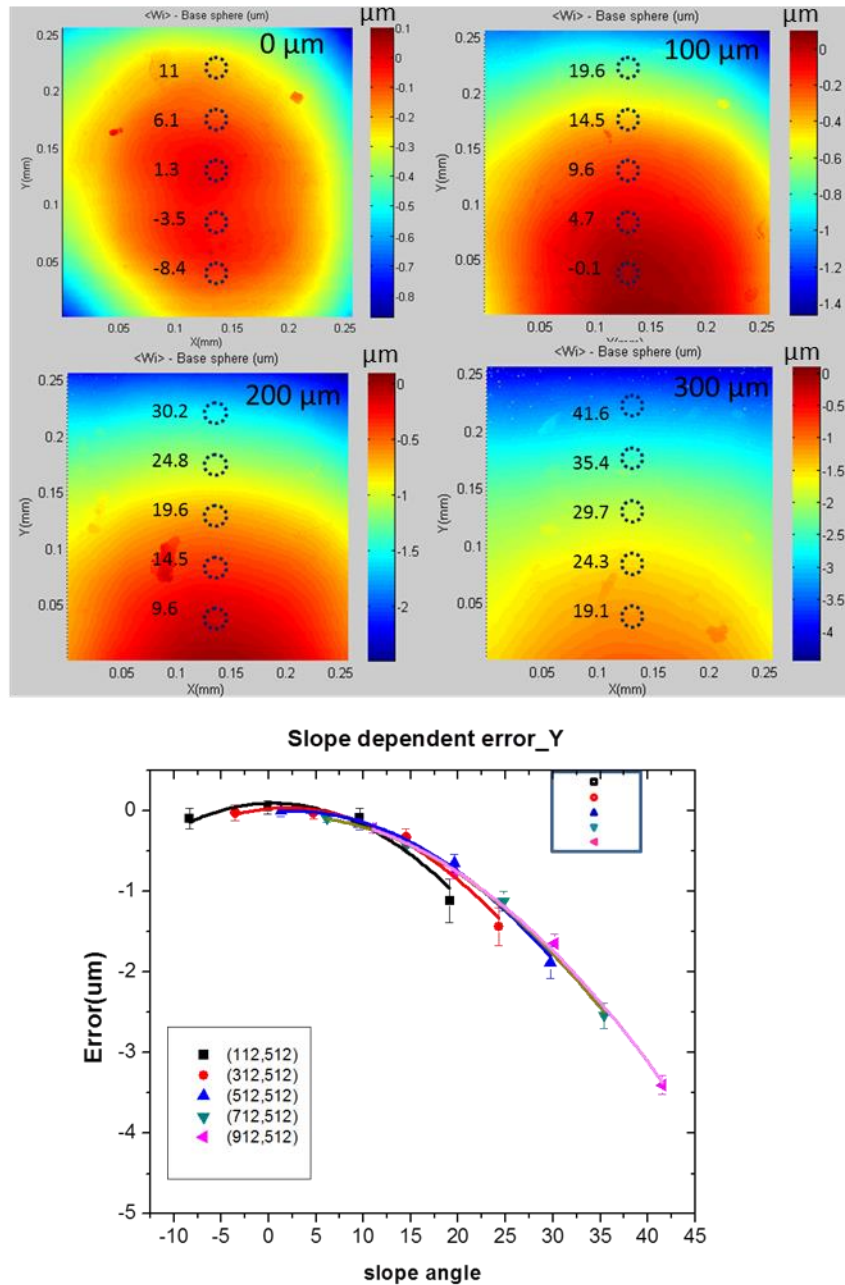


Figure 52: (Top) Error maps when the RBT is done at four positions in the vertical direction over the FoV: 0  $\mu\text{m}$ , 100  $\mu\text{m}$ , 200  $\mu\text{m}$  and 300  $\mu\text{m}$  off center, respectively. Each dashed circle (exaggerated) represents  $\sim 30$  pixels whose center was used for slope angle estimation (number on left of each circle). (Below) Systemic bias plotted as a function of slope angle for each error map shown above.

From the error maps in both the X and Y directions, one can notice that the slope orientation (positive or negative) has almost no impact on the system bias. Only the

magnitude of slope angle is significant. In other words, no matter what position of a sloped region of the surface in the field of view, the value of the height error bias will depend only the local slope of the surface. We can see this in the error maps by generating contours of constant surface slope (white dashed curves in figure 53) and seeing that these contours also approximately correspond to lines of constant height error in the maps.

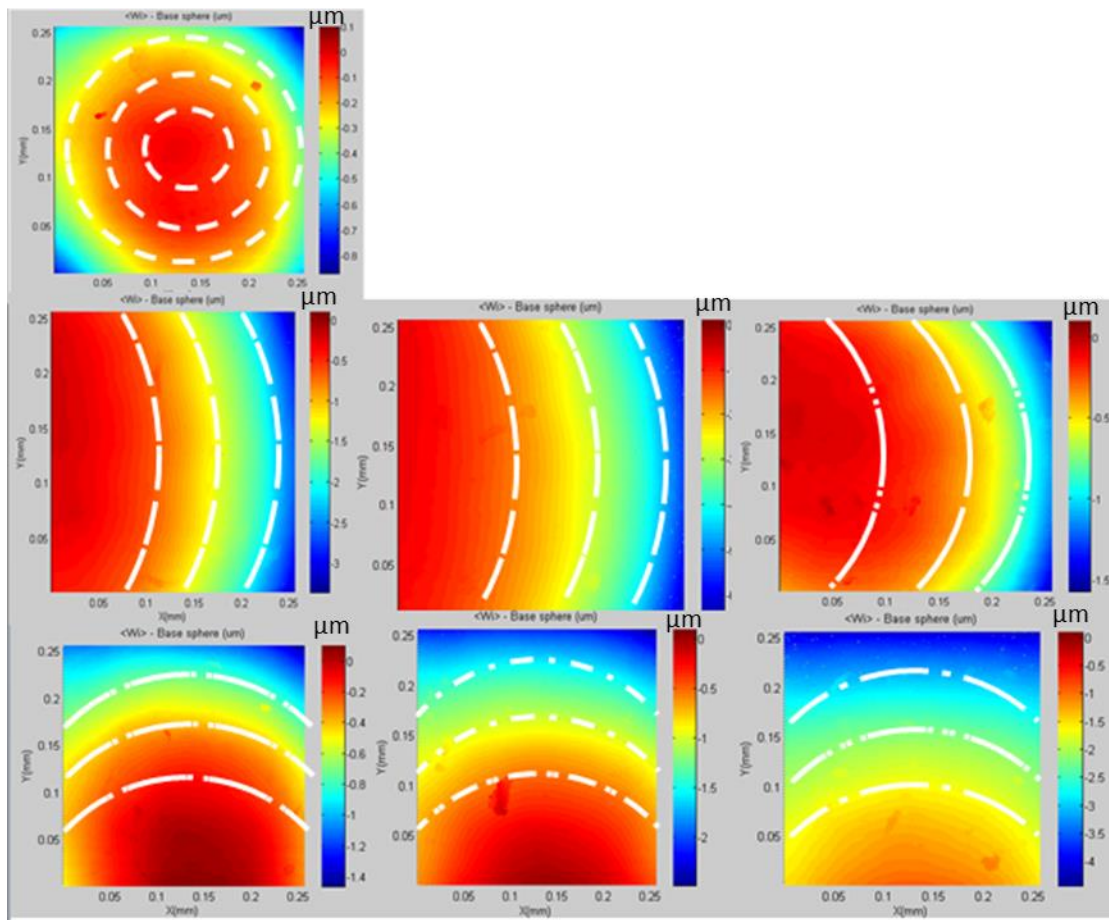


Figure 53: Contour lines of constant surface slope magnitude are shown as white dash curves superimposed on the error maps.

By using all the data points that share the same slope angle, the relationship between systematic error and magnitude of slope angle can be investigated more thoroughly.

Figure 54 plots 12 magnitudes of slope angles and their corresponding errors, where the

error is taken to be the average of all height errors from the maps for at all pixels with the same slope magnitude. The uncertainty is defined as the standard deviation of the height errors. The large uncertainty appears at large slope angle in part due to the stronger scattering impact to the measurement. Of course, the ball error, environmental factors, a weak FoV dependence and other possible factors also may be contributing, and are discussed in the next section.

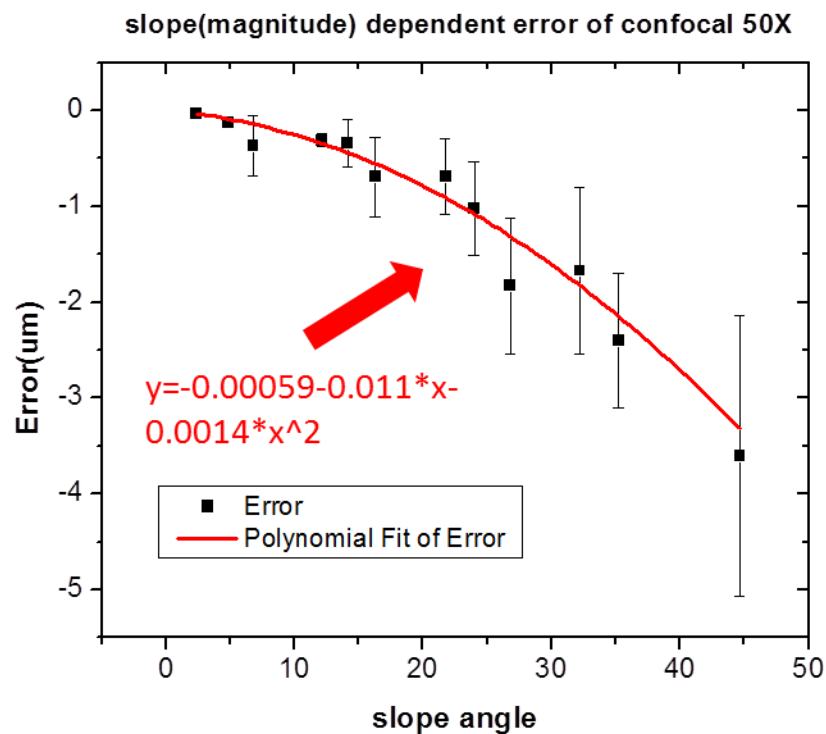


Figure 54: Systematic error of the Olympus LSCM 50X as a function of magnitude of surface slope angle. A parabolic relationship was generated by fitting the data.

#### 4.3.2 Uncertainty Analysis

As discussed in the simulation section, the ball error spatial distribution and its unknown symmetry potentially add an error to the calibration that is small and negligible on the scale of 800 nm. In addition to this factor, there are four major contributors to the

uncertainty to be considered, random noise in the measurement, distortion of the optical system, stage drift during data acquisition and base radius uncertainty.

#### 4.3.2.1 Random Noise

Random noise in the measurement is inevitable. This is the noise in each measurement that is zero on average. It is reduced by averaging and in this way behaves the same way as the errors on the surface of the ball. Consequently random noise contributions, like the ball errors, impact the convergence of the RBT. That is, the size of the ball errors, the size of the random noise, and the desired calibration uncertainty determine the number of measurements to be averaged.

The convergence rate can be quantified by taking a sample of random measurements, and averaging subsets of the data for a particular value of  $N$ . Since  $N$  is finite, each subset is not exactly the same because residual noise and ball error is present. Thus, differences between pairs represent the magnitude of the residual noise and ball error for each value of  $N$ . Specifically, we randomly divide our  $N = 60$  RBT measurements in different averaged groups for  $N = 2, 4, 6, 10 \dots$ . We then calculate differences between pairs with the same  $N$  and obtain an average of the residual noise difference for each value of  $N$ . We use the average RMS of the difference map, divided by  $\sqrt{2}$ , as a quantitative measure. This quantity converges to zero as  $N$  goes to infinity. The  $\sqrt{2}$  factor reduces the RMS to the expected value for a single measurement, rather than a difference [28].

Figure 55 shows the convergence for the confocal microscope calibration presented here. It follows a  $\sim 1/\sqrt{N}$  dependence as expected. For our ball error and random noise characteristics,  $N = 60$  leads to an estimated residual noise/error contribution to the

calibration result that is ~26 nm. This is smaller than the ~800 nm maximum slope-dependent error observed for the 50x LSCM calibration and an acceptable calibration uncertainty level.

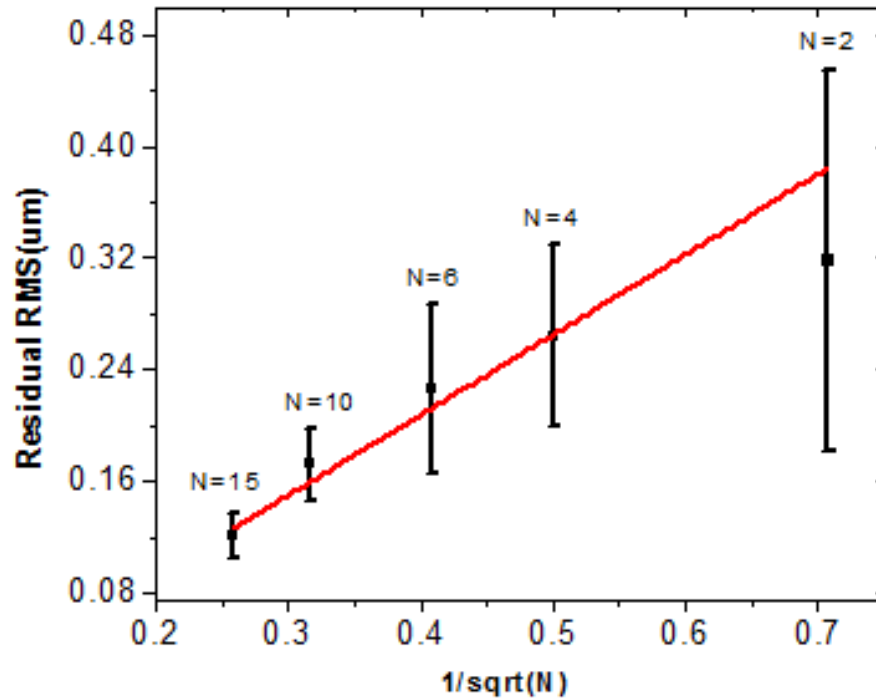


Figure 55: Residual RMS of the RBT as a function of  $1/\sqrt{N}$  where N is the number of measurements.

#### 4.3.2.2 Distortion

As discussed in Chapter 3, it is necessary to consider the impact of distortion on the calibration result. A 10  $\mu\text{m}$  pitch and 100 nm height cross grating artifact was used for the distortion measurement. The 3D profile of such an artifact under 50x objective is shown in figure 56.

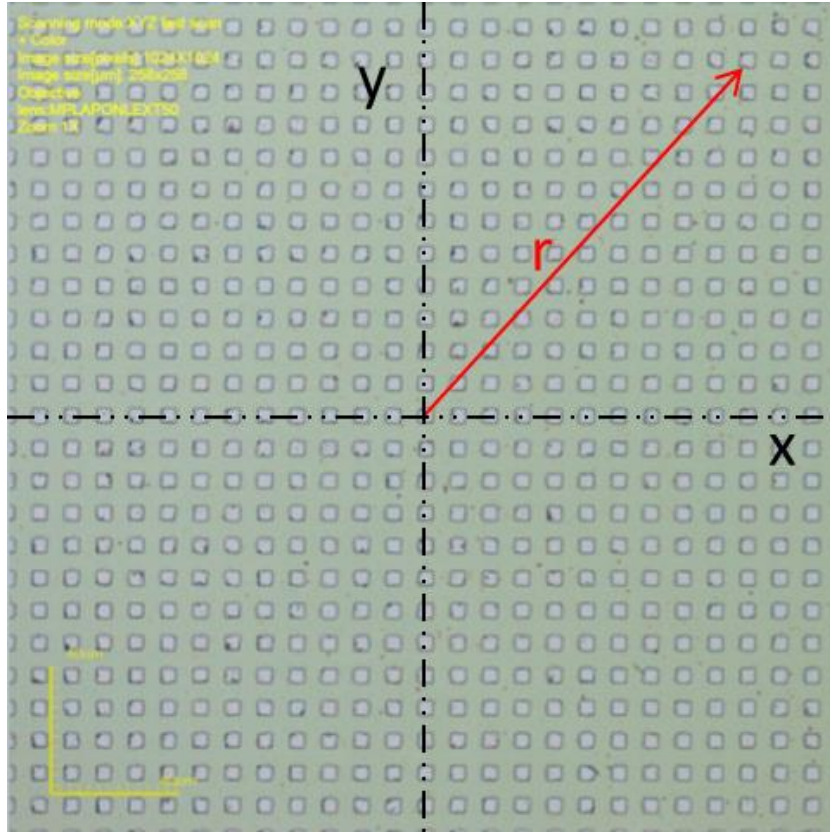


Figure 56: 3D profile of a 10  $\mu\text{m}$  pitch cross grating used for calibrating distortion of Olympus LEXT 4000 50x objective.

An estimation of the distortion coefficient is done by calculating the separation distance between two adjacent squares' centroids. Figure 57 shows the measured period in both the X and Y directions along the axis. Similar to the SWLI results discussed in 3.5.1, no clear “U” or reversed “U” trend is observed in the data. Based on a simplified distortion model described in equation 3.13,

$$r' = r + k_1 r^3,$$

a chi-square minimization [82] provides an estimate of the distortion coefficient of  $k_1 = -2.09 \times 10^{-6}$ . Plugging this into the distortion model used for the simulation without any other error source, we find that this level of distortion leads to an error in the calibration result of no more than  $PV = 0.0006 \text{ nm}$  when a RBT is carried out at the

center of the FoV with  $N = 60$ . Comparing this amount to the scale of the error maps measured, the impact of distortion on our calibration results is negligible.

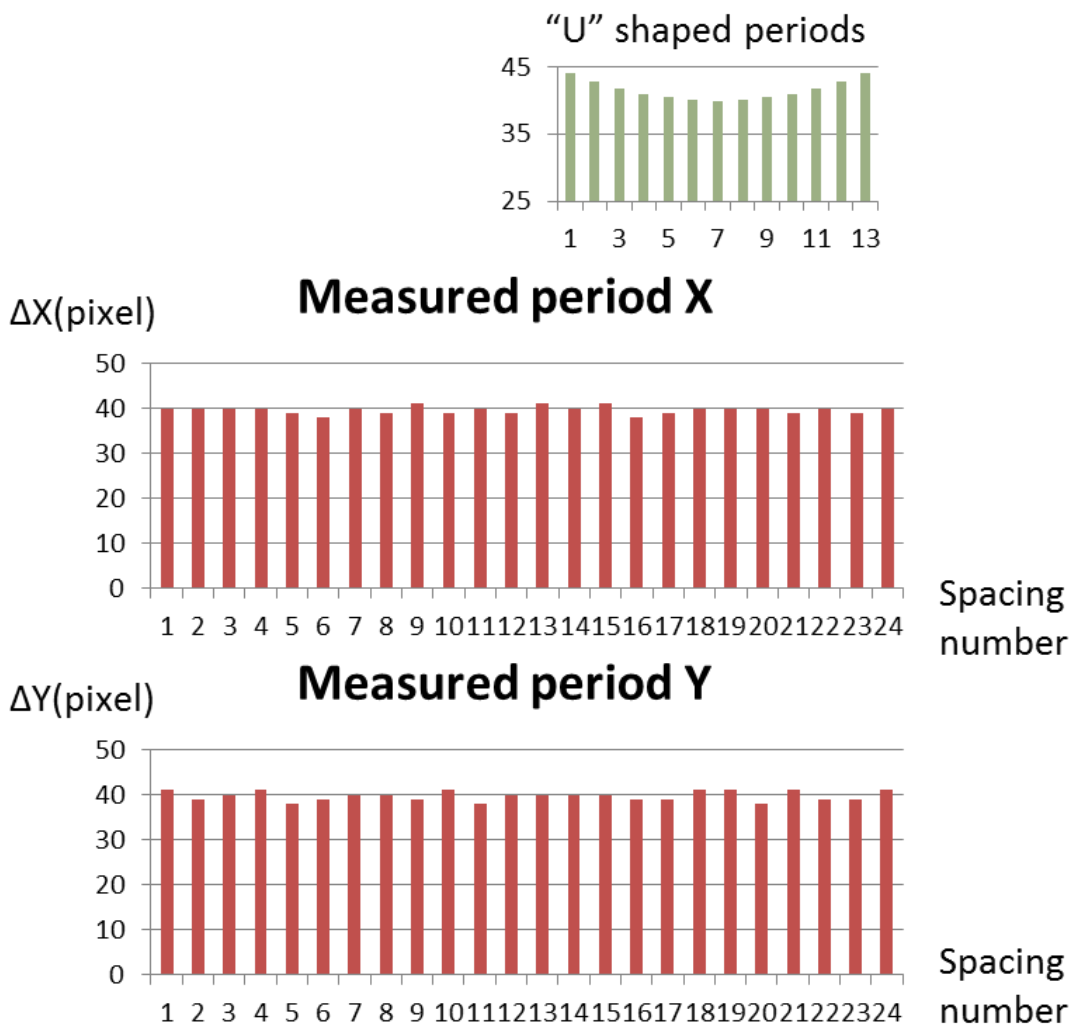


Figure 57: Distortion measurement result of the LSCM 50x. The separation of adjacent squares from the cross grating in the middle row (X) and column (Y) was plotted as a function of the square’s location. The “U” shaped trend above is sketched to show how the grating period would appear in the presence of clear distortion.

#### 4.3.2.3 Drift

Stage drift occurs over the duration of the measurements and consequently the ball center location drifts from measurement to measurement. This is (usually) thermally-

induced drift in the field of view that is not captured by the position encoder readings for the stage. Thus, characterization of drift is important for validating the RBT.

Several methods can be used to address instrument drift, and they can be roughly grouped into two categories: drift calibration with target tracking and active feedback systems. Tracking with a fiducial marker on top of the sample is a good example of target tracking. Resolution on the order of 1 nm in the horizontal X-Y plane and 5 nm in Z direction has been demonstrated in certain limits [83]. There are several approaches in the target tracking category [83-86], and this category has a long history, particularly for imaging in biology. The preparation of the marker and the setup are often complex, and this method is not always practical for surface metrology needs in precision engineering, especially when stage drift changes from day to day, maybe hour to hour. In addition, tracking the target's position is not an easy task as measurement noise can easily affect data processing and the identification of the target's location. Active feedback systems are another way to stabilize the stage. By using this method, Carter et al. demonstrated a system that can maintain the stability of 0.1 nm in three dimensions for 1 second [87]. In their setup, a marker was used to track displacement and a piezoelectric stage was used to correct drift. Setups are complicated in this category and usually costly. In our RBT application, a convenient and robust method for simply calibrating drift rates is sufficient [88].

Instead of tracking a visible spot (a fiducial) in the field of view (FOV) with time directly, we take subsequent height profile measurements of a cap on a spherical artifact whose diameter is larger than the field of view. Then we use a robust fitting



algorithm to find the center of the best-fit sphere to the data, and the center location provides the information on the drift properties, such as drift direction and drift rate. The method is simple and inexpensive and the measurement uncertainty can be relatively small since height data over the entire field of view is used for the analysis.

Choosing the best diameter for the spherical artifact is important. If the diameter is too large, a spherical fit becomes ill defined as the height profile becomes too flat over the FOV. If the diameter is too small, steep slopes at the edge of the FOV can lead to noisy data and/or data dropout, as shown in figure 58. Simulated measurements were carried out in Matlab to test the validity and limits of this proposed method.

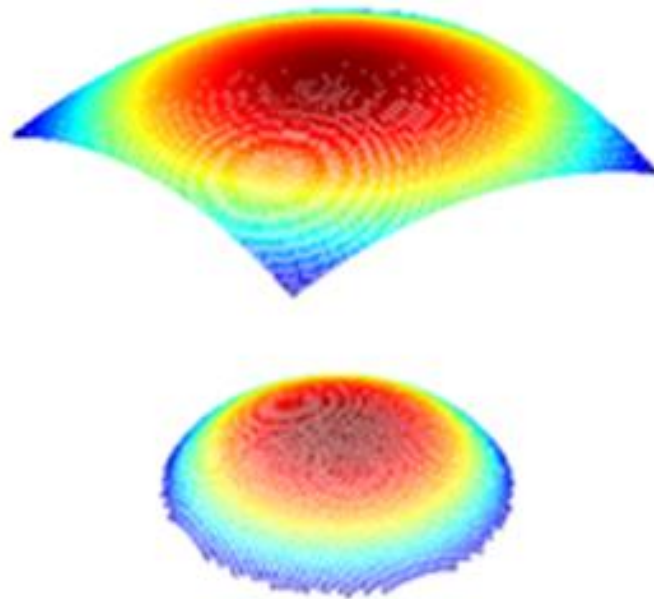


Figure 58: Schematic of a nearly flat ball profile when a very large radius artifact is used (top) and a highly curved profile when a very small radius artifact is used (below), showing data drop out at the edge due to slope limitations of the instrument.

For short periods of time, drift is usually linear [89]. Let  $x$  and  $y$  represent the coordinates in the plane of the part and  $z$  represent the orthogonal height axis. The drift model will be

$$x_c(t) = x_{co} + \mu_x t \quad (4.1)$$

and

$$y_c(t) = y_{co} + \mu_y t \quad (4.2)$$

where  $x_c$  and  $y_c$  are the center coordinates of the best fit sphere and  $x_{co}$  and  $y_{co}$  are the coordinates at the start of the drift test (approximately the middle of the field of view).

The linear drift rate can also be evaluated as

$$\mu_l = \sqrt{\mu_x^2 + \mu_y^2} \quad (4.3)$$

and the center coordinate tracked along a line as

$$l = \mu_l t \quad (4.4)$$

The drift rates are determined by taking a series of measurements of the surface of the spherical artifact, fitting each measurement to a sphere to determine the center coordinates, and plotting the center coordinates as a function of time. A linear fit to the data is then used to extract the slopes  $\mu_x$  and  $\mu_y$  for equations 4.3 and 4.4.

The simulation starts by defining a realistic ball geometry using a spherical harmonic basis set (as discussed in section 3.1.1) and then positioning the ball in a desired location in a defined field of view. The sag (height) values over the field of view are then taken as the simulated profilometer measurement. Drift can be applied to the ball location in the field of view and random noise can be added to each measurement. Each measurement is then processed in the same way as is done experimentally. That is, the robust algorithm

described in section 3.1.3 is used to find the best-fit sphere to each simulated cap measurement. The best-fit sphere center coordinates are then plotted versus time to extract the drift rates  $\mu_x$  and  $\mu_y$  (equations 4.3 and 4.4).

Random noise in each measurement will impact the drift rate measurement and the ball size choice. There are many causes of random noise, e.g. air turbulence and noise from the scanner, and each has a unique spatial frequency characteristic. Noise sources with low spatial frequency content are the most important to consider as these will have the largest impact on the center coordinates of a best-fit sphere to the height profile data. The magnitude and spatial character of the random noise should be evaluated to understand this impact on the drift rate measurement. This can be done with a repeatability test for the instrument where a sequence of ball profile measurements are taken without changing the ball position as quickly as possible (to minimize drift between measurements). The random noise can be assessed by calculating the difference between subsequent measurements and repeating this for many measurement pairs to obtain a statistical sample of the random noise characteristics. Each measurement  $W_i$  can be written as

$$W_i = W_{base} + Error_{ball} + Error_{system} + Error_{noise(i)}, \quad (4.5)$$

where  $W_{base}$  is the profile of a perfect ball,  $Error_{ball}$  is the ball error on the local patch,  $Error_{system}$  is the systematic error from the instrument itself, and  $Error_{noise(i)}$  is the random noise term. The first three terms on the right in equation 4.5 are constants (in the limit that measurements are taken quickly and drift is negligible). Pair-wise subtraction of adjacent measurements indicates the random noise contributions only

$$Error_{noise(i)} - Error_{noise(i+1)} = ErrorDiff_{noise} \quad (4.6)$$

Since only randomly varying noise remains in the difference, the size scale of the random noise on a single measurement is approximately a factor of  $\frac{1}{\sqrt{2}}$  smaller than what is statistically observed in the difference[28] We are most interested in low-order spatial frequency noise, so the set of low-order Zernike polynomials are useful for the analysis. The first 36 lowest order Zernike polynomials can be fit to each noise difference map, and then the statistical distribution of the coefficients extracted. The mean coefficient for each Zernike polynomial is approximately zero and the standard deviation of the coefficients (multiplied by the factor of  $\frac{1}{\sqrt{2}}$ ) represents the statistical nature of the noise. The standard deviation for each coefficient can be used in a simulation to randomly generate noise to then add to each simulated measurement (assuming a Gaussian probability distribution).

We carried out this noise evaluation for a confocal microscope with a 50x objective. Twenty measurements were taken and 10 noise difference maps were generated by subtracting every pair of subsequent measurements. We then decomposed each difference map into low and high-order spatial frequency components by fitting with the first 36 Zernike polynomials. We found that the random noise consists of a low frequency and a high frequency component, as shown in figure 59. The ring structure in the high frequency noise map is likely noise from the scanner during the data acquisition process. And low frequency noise is likely from environmental effects such as air turbulence. From the spatial signature of the two noise contributions, it is clear that the low-frequency noise will have the largest impact on the spherical best-fit analysis.

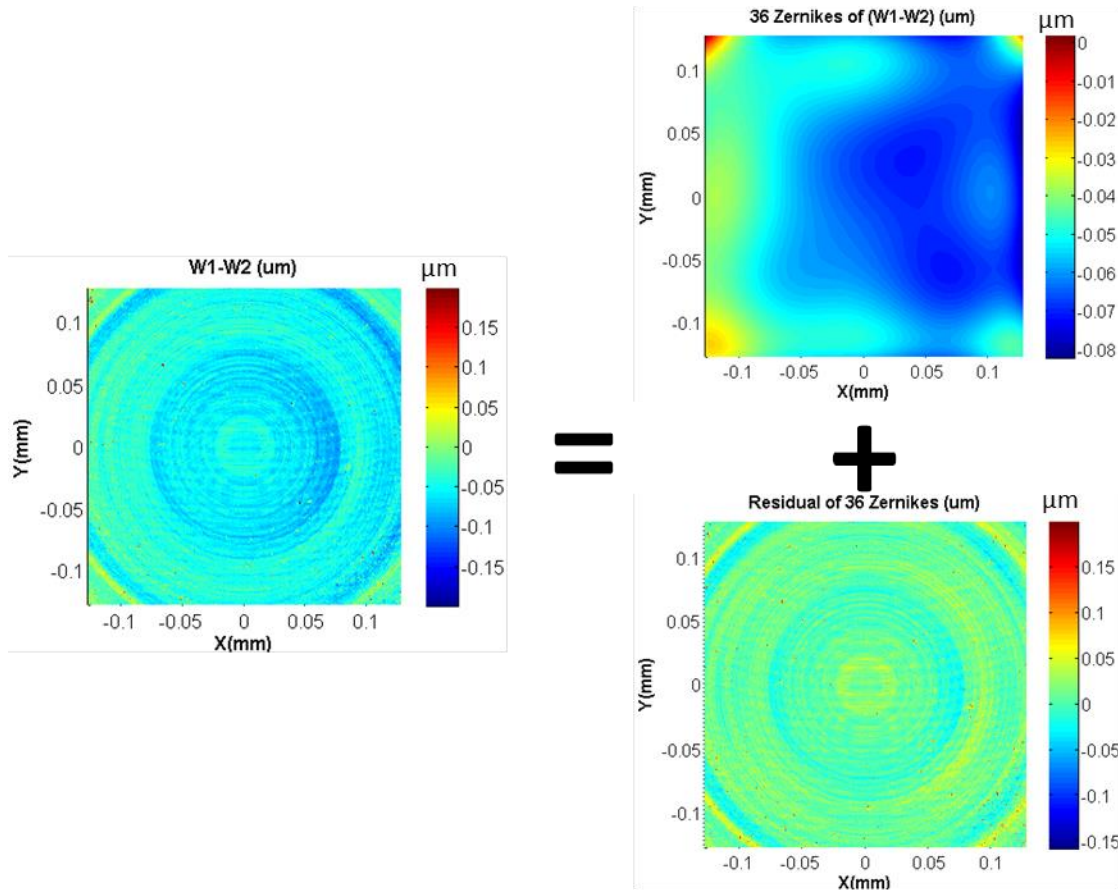


Figure 59: Example of the decomposition of a noise difference map which is the difference between two subsequent ball profile measurements. Low frequency noise, e.g. environmental sources (top right) and high frequency noise, e.g. scanner noise (below right).

In the simulation, we generated a ball with an RMS ball error of 100 nm and a base radius of 0.595mm, to model the ball used in the experiment. We explored a range of drift rates and focused on rates of  $d_x = -100$  nm/min in the X direction and  $d_y = 50$  nm/min in the Y direction. These values are representative of published drift rates and of the drift rates observed in the confocal microscope measurements presented here [89]. In the simulation, a new measurement is generated every 1 minute where the simulated ball center is shifted by the amount defined by equations 4.1 and 4.2. Randomly chosen Zernike coefficients are used to generate a noise map for every

measurement which is then added to the height profile to represent the random noise effects. The best fit algorithm described in 3.1.3 was then used find the center coordinates.

In the simulation, the drift test was set to 100 minutes with one measurement per minute. The trace of ball center's coordinates as a function of time therefore would determine the drift property. The uncertainty of the drift rate was determined by the standard deviation of the drift values (slope of ball center's coordinates as a function of time). The simulation shows that, with  $R = 0.595$  mm using the 50X objective whose field of view is 0.256 mm by 0.256 mm, the uncertainty of the drift rate measurement  $\delta_{\mu}$  in both the X and Y directions is on the order of 0.5 nm/min, as shown in figure 60.

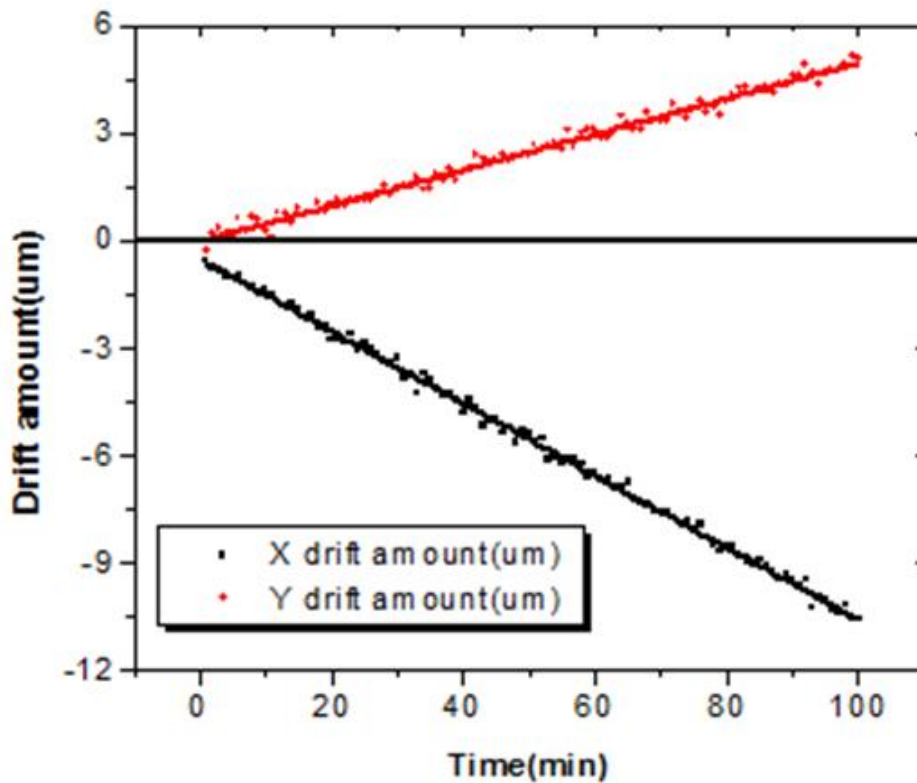


Figure 60: Simulation result of a realistic ball's best fit center movement with a rate of -100nm/min in X direction and 50 nm/min in Y direction. The uncertainty is up to 0.5 nm/min.

As mentioned before, the ratio of the ball diameter to the field of view will impact the noise in the best fit sphere center coordinates. If the radius of the ball is too large, the field of view is small compared to the ball, and there is little spherical sag over the field of view. If the low spatial frequency measurement noise is comparable to the sag, the noise will strongly influence the spherical fit and the center coordinates will be noisy. We explored this in simulation by fixing the field of view (corresponding to the 50X objective condition), fixing the magnitude of the random noise, and varying the radius of the simulated ball. The drift test was set to 100 minutes with one measurement per minute. The same procedure discussed above was followed to estimate a drift rate uncertainty for each ball radius considered. The results summarized in figure 61 are  $\delta_{\mu}$  for both X and Y. The results show that the uncertainty of the drift rate measurement can be smaller than 12 nm/min if the ball radius is under 10 mm. As the ball radius is reduced, data is dropped out of the simulated measurements when the slope becomes larger than the reported measurement limit for the confocal microscope. Thus the measurable slope limitation becomes important in the small ball limit and the uncertainty will again rise. But, this effect is smaller and becomes significant only for very small balls that are no longer practical to work with for the measurement.

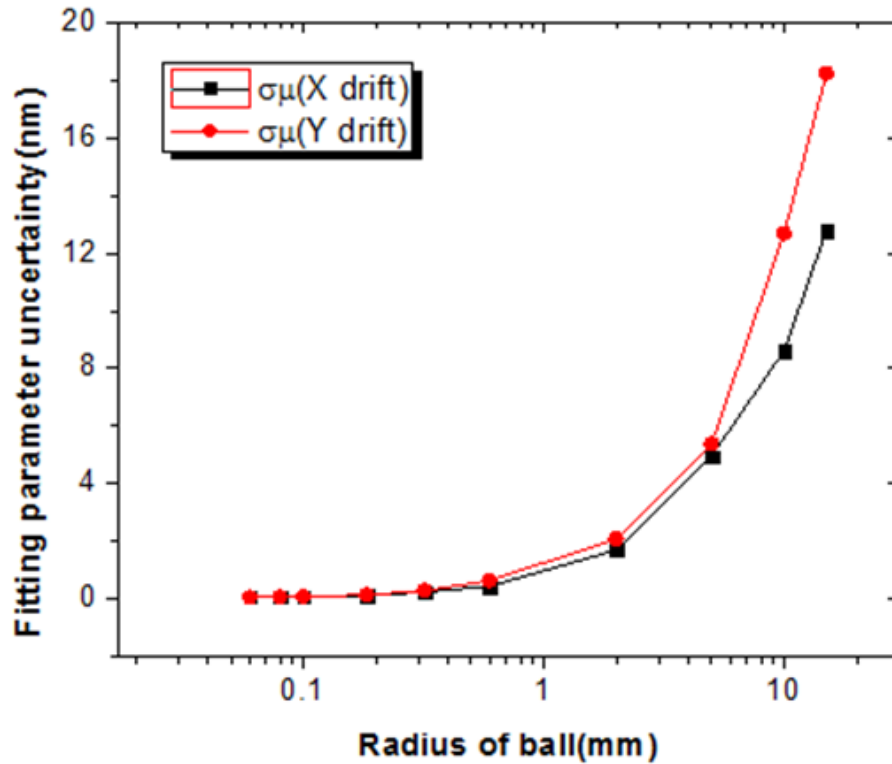


Figure 61: Drift calibration uncertainty for a confocal microscope as a function of ball size. A drift uncertainty below 12nm/min can be obtained once the ball radius is smaller than 10mm. Data drop out will increase the uncertainty but the impact is smaller than that of ball size.

In summary, the simulation shows that a reasonable ball size with reasonable quality can be used to measure drift rates with reasonable measurement uncertainties. With a ball with radius  $R=0.595$  mm a drift test over 100 minutes with one measurement per minute results in drift rate uncertainties of  $\sim 0.8$  nm/min.

In the experiment, a commercial confocal microscope (Olympus LEXT OLS4000) placed in clean room was used to demonstrate the procedure. A grade 3 steel ball with  $R=0.595$  mm was chosen for the measurement. A simple fixture was used to allow the ball to be stabilized, consisting of a brass sheet with a center indentation sandwiched between two large washers. The ball rests at the indentation of fixture that is placed on the microscope stage. It is approximately centered in the field of view at the start of the drift



test. Using the 50x objective, 14 sequential measurements were taken and each measurement took approximately 1 minute to acquire. The time interval between measurements and the duration of the drift test will vary and depend on the application. Each measurement is processed as described above to extract the center coordinates of the best fit sphere. The center coordinates are plotted versus time, as shown in figure 62 and fit to a line to estimate the drift rate. The uncertainty of drift rate was determined by the standard deviation of the fitted slope values.

In our test, the X drift rate is 75 nm/min with uncertainty  $\delta_{\mu_x} = 4$  nm/min and the Y drift rate is -54 nm/min with  $\delta_{\mu_y} = 8$  nm/min. The drift is approximately linear over this time scale in the confocal microscope. Due to the shorter time intervals taken in the experimental drift test (14 mins) compared to the time intervals used for the simulation (100 mins), a smaller uncertainty with longer time drift test is to be expected.

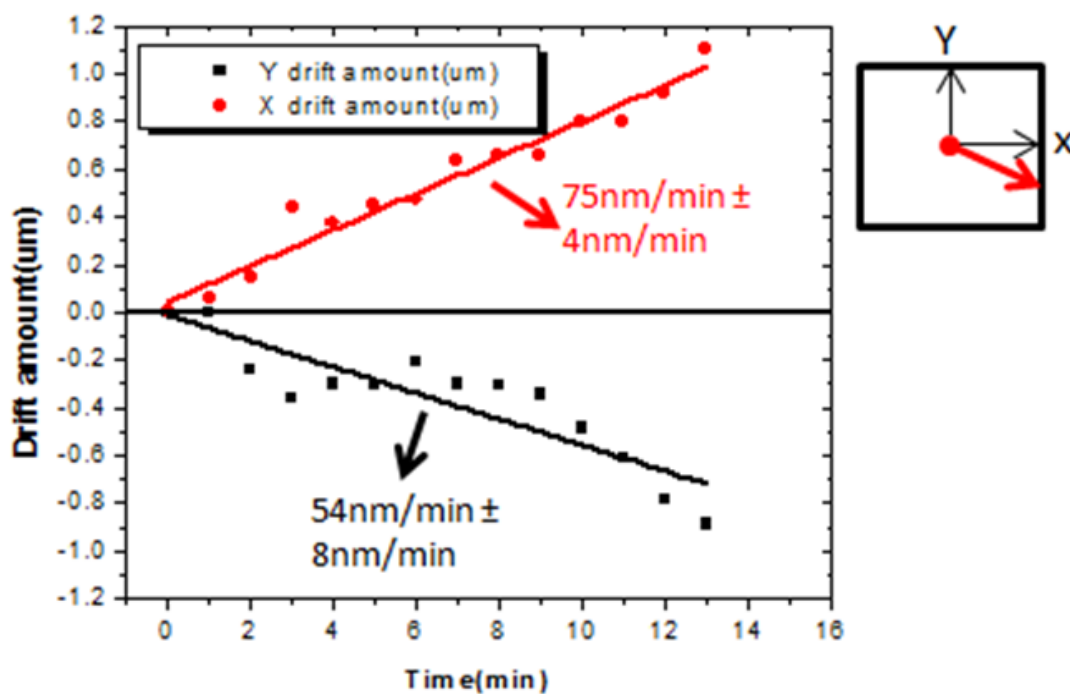


Figure 62: Experimental results of a confocal microscope drift measurement by using a 0.595 mm radius grade 3 realistic ball under a 50X objective (left). A coordinate diagram illustrates the confocal's drift property (right).

After the drift rate calibration, as discussed in section 3.6, the simulation shows this can cause a height error in the calibration, but at most on the order of  $\sim 1$  nm peak to valley. This is negligible comparing with systematic bias which is  $\sim 800$  nm at a slope angle of 12 degrees and can be safely ignored.

#### 4.3.2.4 Base Radius

An estimate of the base radius of the ball used for the calibration is critical since a base sphere must be subtracted from the average of the measurements. The ball radius was mechanically measured with a Mahr MFU714, the measurement procedure was introduced in section 4.2. The uncertainty of radius measurement is  $\pm 0.5$   $\mu\text{m}$ . A ball radius uncertainty at this level translates to a sag difference at the edge of the field of view of  $\sim 25$  nm for the nominal radius of  $R=0.595$  mm. This is small on the scale of the

calibration error map which shows a maximum error of ~800 nm at the edge of the field of view.

All the uncertainties discussed above have negligible impact compared to the magnitude of the systematic error as shown in figure 54. Thus, we could conclude that the error we captured is from the system itself rather than other sources.

### 4.3.3 RBT with Different Ball Sizes

In order to test the validity of the RBT in the experiments, two independent RBTs with different size balls were carried out. Two different balls were used with radii 2.778 mm and 1.983 mm, and both had ball error RMS = 100 nm. We apply these two balls to the calibration of the Olympus LSCM with the 50x objective as we did with the 0.595 mm radius ball. The resulting error maps are shown in figure 63.

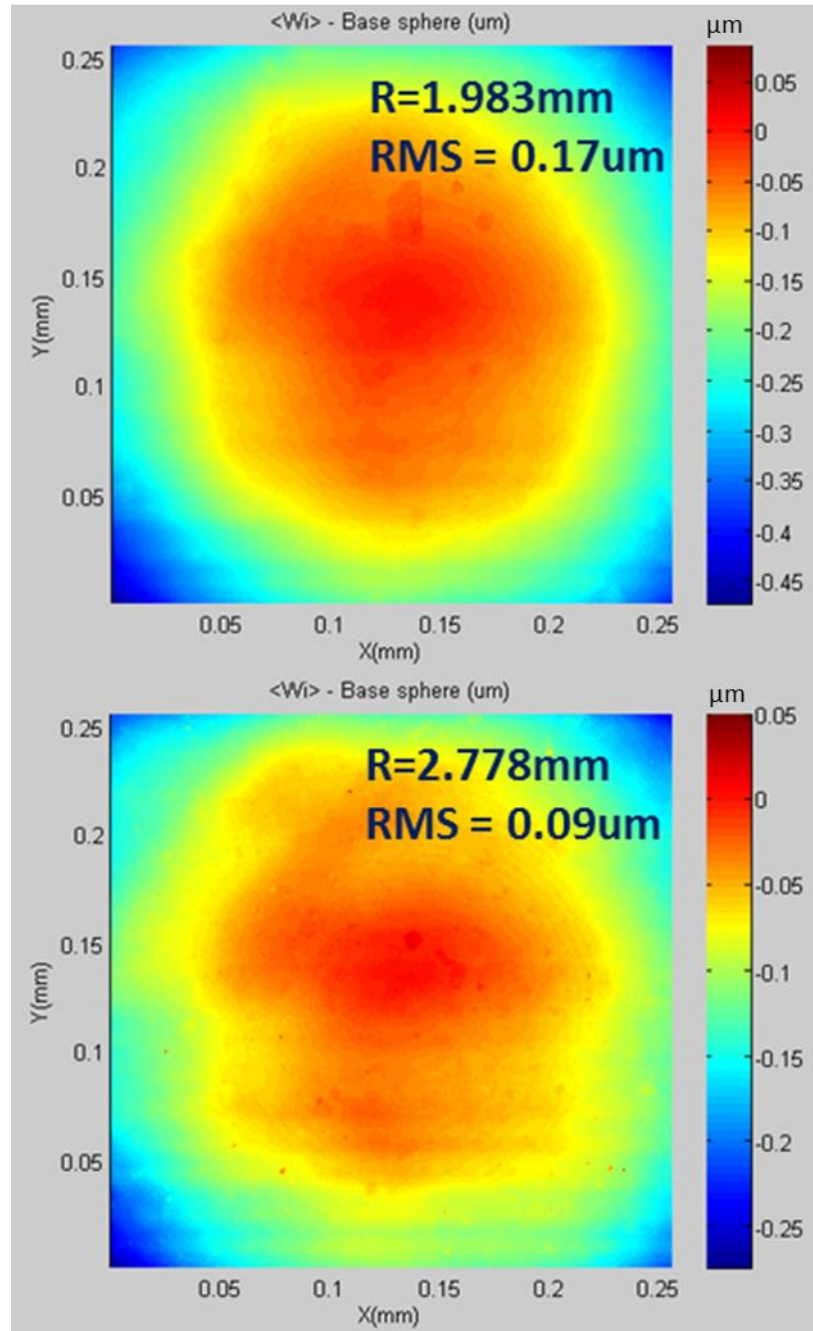


Figure 63: The RBT calibration results with two different ball sizes for a laser scanning confocal microscope configured with a 50X objective.

By plotting the errors as a function of slope angle, we choose a line profile from the center up to the middle edge of the FoV. A smaller ball (red curve shown in figure 64) has larger slope range and vice versa for the larger ball (blue curve in figure 64). These

two curves falls onto the same trend as discussed in section 4.3.1. The system error depends on the magnitude of the surface slope. Thus, the calibrated instrument slope-dependent bias does not depend on the ball size used for the calibration, as postulated in the theory. As long as the working distance allows rotation of the ball for the RBT at different positions, the size of a ball will not matter.

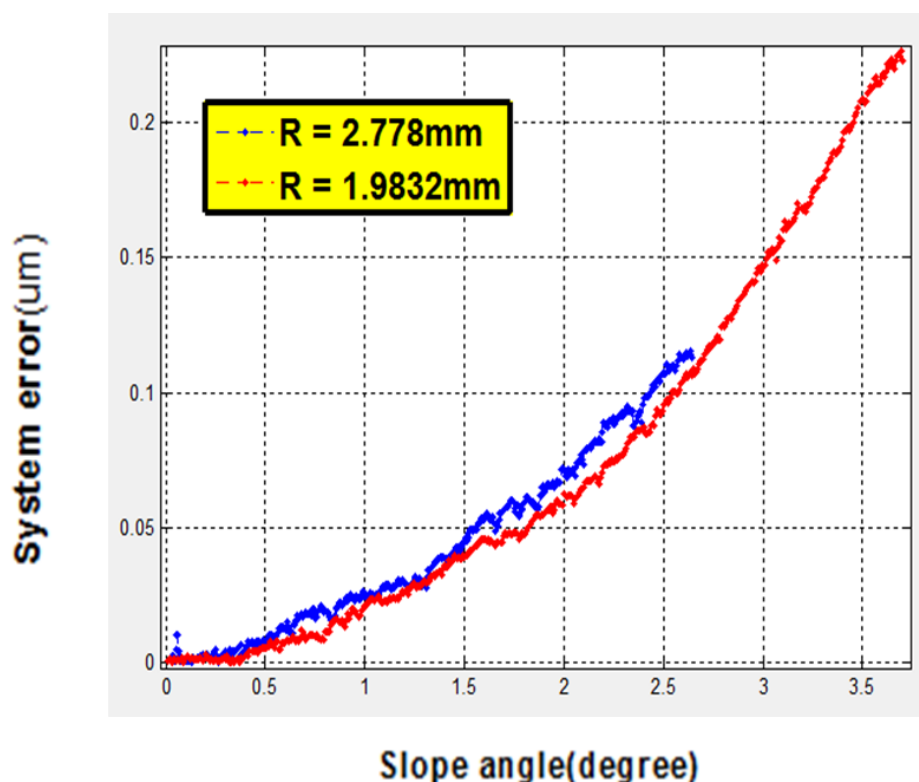


Figure 64: Systematic error for the Olympus LSCM 50X generated by two independent RBTs that are implemented with two different ball sizes.

#### 4.4 Calibration of The SWLI Using The RBT

Similar to the LSCM calibration, RBTs were carried out on a SWLI to assess the order of magnitude of slope-dependent errors for this instrument. For SWLI measurements, the instrument errors will depend on the correlogram analysis method used. As shown in table 3 below, we compared three algorithm options available on the Zygo available on

the UNC Charlotte campus, ‘High’, ‘Normal’ and ‘Low’. Detailed descriptions of each method are discussed in section 2.2.2.

Table 3 Correlogram analysis options in a commercial Zygo Newview 5000 SWLI[90].

FDA Res	Technique	Vert. Res.	Conditions of use
<i>High</i>	Centroid detection of envelope peak, uses least squares slope result and phase offset, with FFT. Equivalent to phase shifting interferometry without $2\pi$ phase ambiguity.	~0.1 nm	Maximum vertical resolution.
<i>Normal</i>	Centroid detection of envelope peak, uses least squares slope result, with FFT.	~3 nm	Rough surfaces, typically > 75 nm Ra
<i>Low</i>	Fast centroid detection of envelope peak, without FFT.	~20 nm	Extended scan option, Scan Length control set to Extended.
<i>Phase 1</i>	Hybrid approach, combines vertical scanning interferometry and phase shifting interferometry techniques in a single measurement. Data is acquired at optimal focus.	~0.1 nm	NewView 5022/5032 only, 80 nm bandwidth filter required, general purpose for scans <150 nm. The Scan Type control must be set to Phase.
<i>Phase 2</i>	Hybrid approach, combines vertical scanning interferometry and phase shifting interferometry techniques in a single measurement. Data is almost instantaneously acquired at optimal focus.	~0.1 nm	NewView 5022/5032 only, 40 nm bandwidth filter required, for step heights from 0 – 5 $\mu\text{m}$ and low magnification objectives. The Scan Type control must be set to Phase.

We used a ball for the SWLI calibration with a radius of  $R = 0.5950 \text{ mm} \pm 0.0005$  mm and ball error  $\text{RMS} = 100 \text{ nm}$ . The result for the SWLI 50x objective calibration is shown in figure 65.

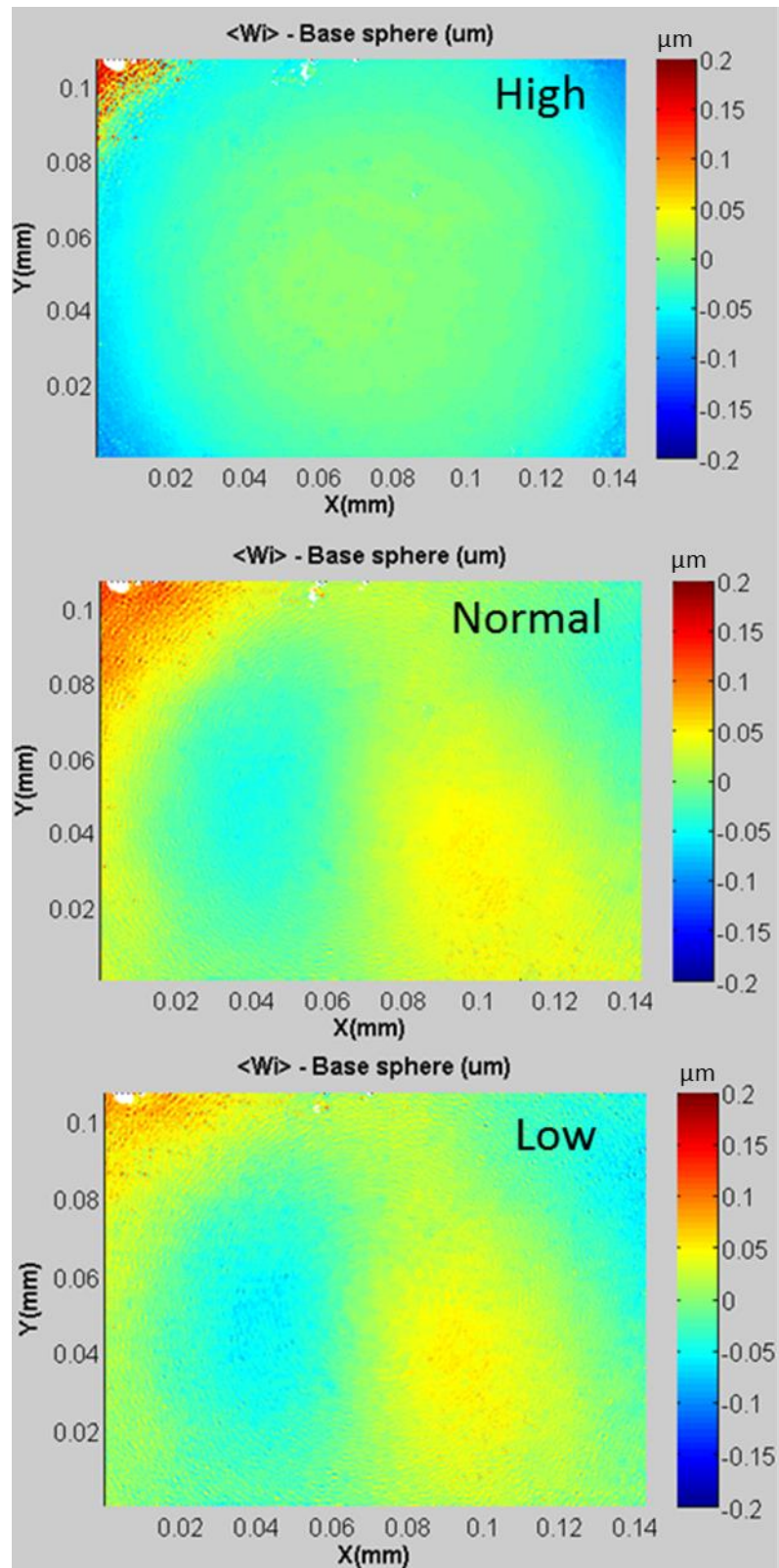


Figure 65: The RBT calibration result for a scanning white light interferometer configured with a 50X objective by using three different correlogram analysis methods.



The calibration shows a clear instrument systematic error that varies over the field of view. The error is zero in the middle on each error map where the ball was centered, and the surface slope is zero. For the “High” algorithm, similar to the LSCM calibration results, the error clearly depends on the magnitude of the slope, with the largest error at the edge (as large as ~50 nm) where the slope is the largest. A value of -50 nm at the FoV edge indicates that the measured height here is too low by ~50 nm. On the other hand, for “Normal” and “Low” algorithms, a coma shaped error appears in both error maps, indicating that a field of view dependence is playing a role here. An extended study was done with multiple positions of the RBT, and the results suggest that, under the “Low” and “Normal” peak detection algorithms, errors are complicated and depend not only on the magnitude of the slope, but also other factors such as the field of view location, and the slope orientation, making the error map very complicated.

Since the “High” algorithm offers the best resolution in the vertical direction (~0.1 nm), we expand the calibration for a large range of slope angles by placing the ball at different FoV locations as we did for the LSCM calibration. Seven error maps were generated, as shown in figure 66, at seven positions for the RBT. One can see that the measurement becomes noisy at a lower slope threshold in the X direction than the Y direction; therefore there are only two error maps chosen in X compared to four error maps in Y. White dashed curves on every map represent contours of constant surface slope magnitude. The same conclusion as drawn for the LSCM calibration is can be drawn for the SWLI “High” algorithm calibration, that is the errors primarily depend only

on the magnitude of the surface slope.

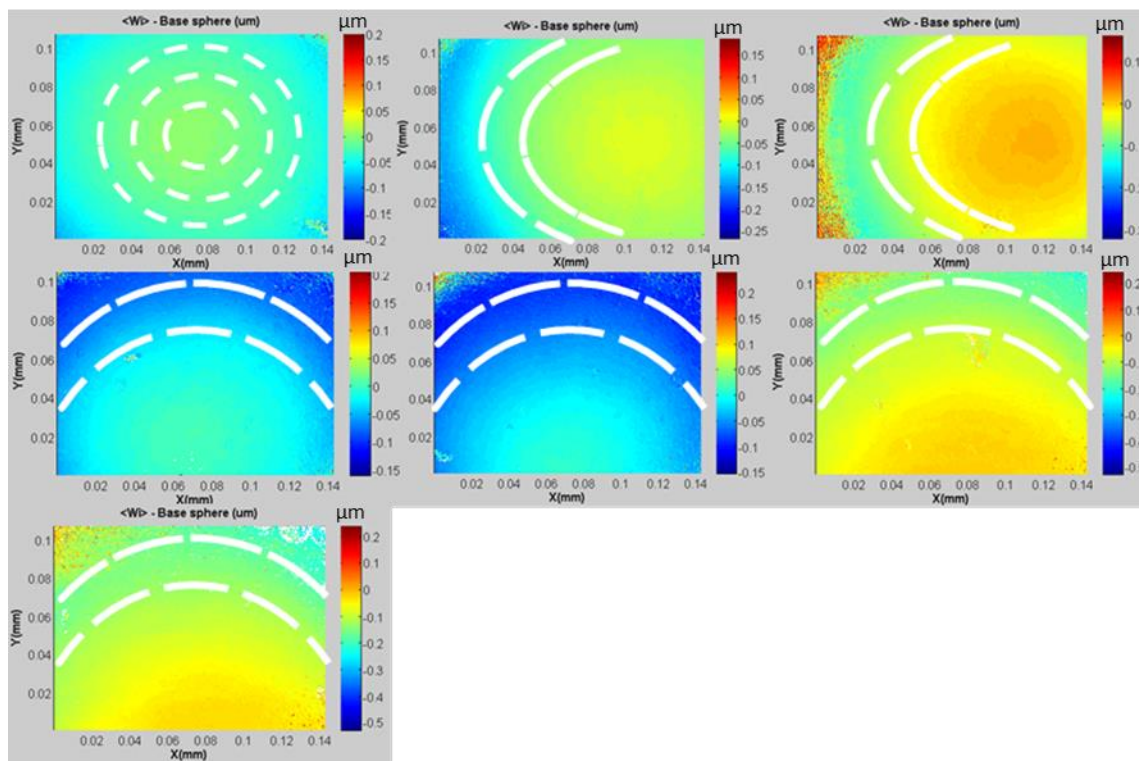


Figure 66: Contour lines of constant surface slope magnitude are drawn on the calibration error maps.

Figure 67 shows a plot of the error as a function of surface slope magnitude. The error is the average of all pixels having the same slope and the error bar is the standard deviation of the height errors. The systematic error in the SWLI is smaller than in the LSCM. A slope of 12 degrees will cause the error of only  $\sim 120$  nm in the SWLI.

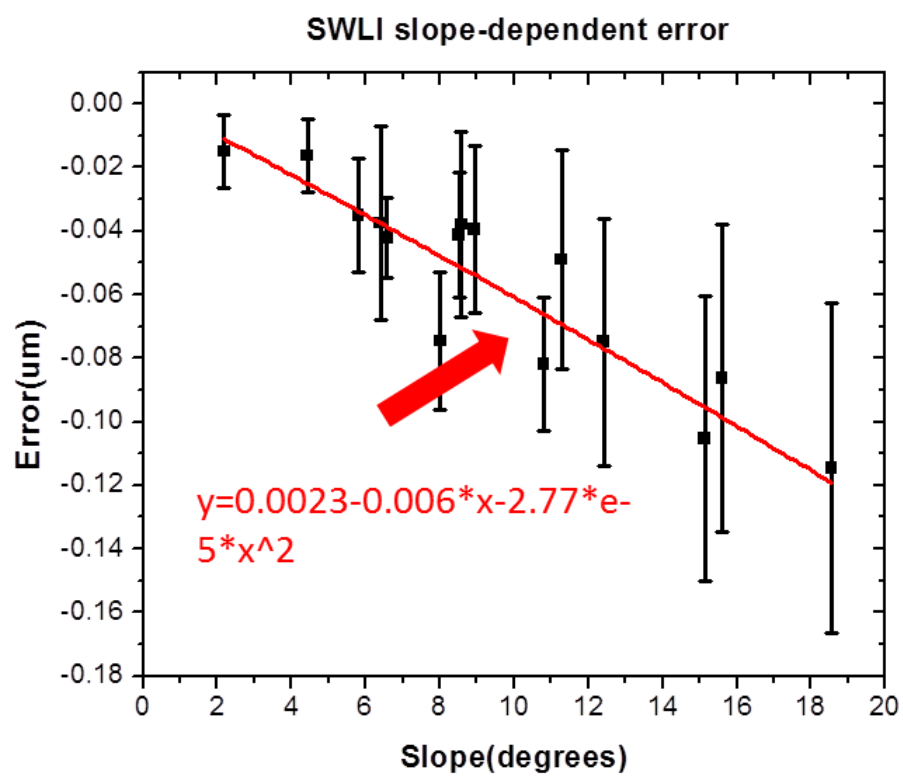


Figure 67: Systematic error of the Zygo Newview 5000 SWLI with the 50X objective as a function of magnitude of surface slope.

## CHAPTER 5: CONCLUSION

Profilometry, as a surface metrology technique, is widely used in many fields such as data storage, automotive, MEMS, electronics, micro-optics, and bio-medical for the inspection of surface topography. Laser scanning confocal microscopy and scanning white light interferometer are the two most common optical profilometers. These techniques are capable of high-speed surface measurements with nanometer-scale repeatability. However, these tools add a systematic bias to the measurement that can be the same order of magnitude as features to be measured. Further, the biases are not easily calculated from first principles because they depend in detail on unknown proprietary details of the instrument. In general they can be quite complicated and depend on parameters such as the location in the field of view, the local surface slope, the data analysis algorithms involved, and the configuration of the instrument. High quality calibration artifacts are simply not available to quantify and ultimately correct all possible combinations. A rigorous, convenient and effective calibration method is needed. By experimentally measuring the bias, one can incorporate this information into the data analysis for error compensation in future measurements.

The RBT is a well-defined self calibration technique for characterizing transmission spheres in phase shifting interferometry (PSI) [26, 27, 65]. However, profilometry measurements are dimensional measurements in the vertical/height direction unlike PSI measurements which are dimensional measurements in the radial direction. In our work,

Matlab has been used to simulate the RBT for a profilometry configuration, and the simulation along with a theoretical study shows that the RBT is valid under reasonable conditions. For example with a realistic ball, the simulation shows that a ball with a symmetric ball error distribution will result in a RBT result that converges to a perfect sphere. On the other hand, an asymmetric ball error distribution results in residual ball error contribution to the RBT result. The magnitude of this residual depends on the proportion of the ball error waviness over by field of view. By exploring the limit of this residual, we find that the magnitude of the residual is small compared to expected and observed magnitudes of system biases in typical instruments. Other factors are also studied in the simulation, such as the convergence rate with the number of measurements averaged, the role of misalignment between measurements, the role of instrument drift, the role of distortion, and the ability to carry out the RBT at different locations in the field of view. All results show that RBT is valid and a useful tool for the calibration.

In the real experiment, there are four major uncertainty sources that will impact the calibration, distortion, stage drift, random noise and base radius uncertainty. Each needs further study through simulation and experiment to understand the impact and quantitatively estimate the contribution to a combined uncertainty. The strategy is to estimate the magnitude of each contribution (such as typical experimental values for the drift), then put these into the simulation to see the magnitude of the effect. Finally, with random ball tests carried out at different positions over the field of view, the slope-dependence as well as the field-of-view dependence of the system bias can be explored. The ultimate goal is a generalized bias correction algorithm. This is demonstrated for a confocal microscope as well as a scanning white light interferometer where the RBT over

the field of view shows a dominate system bias that depends quadratically with the magnitude of the slope and is approximately independent of the field of view location.

In summary, we deliver a proven self-calibration technique for a profilometer with both simulation and experiments. An example of a profilometer system bias correction algorithm is generated. The calibrated error map can be used for compensating future low frequency form measurements, such as form measurements of microlenses with a similar slope range. We also proposed and demonstrated a non-traditional way to characterize the drift in an instrument that is based on tracking the center of the best fit sphere to measurements of the surface of a ball artifact. Simulation shows that choosing a ball with a suitable ratio of field of view to ball size is important and that the method can be effective in terms of low uncertainty.

For a realistic RBT calibration of a profilometer, a list of steps should be followed:

1. Choose a ball with suitable ratio of field of view to ball size in order to have enough working distance at large slope. An independent measurement of the ball radius is needed (e.g. mechanical measurement).
2. Choose a ball with a good surface quality so as few measurements as possible are needed.
3. Carry out the RBT by measuring random ball patches  $N$  times (e.g.  $N = 60$ ).
4. During the data processing, before averaging the measurements, the arbitrary height offset between every measurement due to scanner drift is removed by adjusting the height of each profile so they all have the same best fit center in  $z$  coordinate.
5. Average  $N$  measurements to obtain  $\langle W_i \rangle$ .

6. Best fit  $\langle W_i \rangle$  to determine the center of the base sphere  $(x,y,z)$ .
7. Subtract a base sphere  $W_{\text{base}}$  with the independently measured ball radius  $R$  and centered at  $(x,y,z)$  to generate the error map.
8. Calculate the surface slope magnitude based on height difference between two pixels.
9. Repeat 1-8 at different locations over the field of view to generate a calibrated slope dependent error curve.

In the future research, we anticipate the need to study on systems where bias depends on slope magnitude, slope direction and field of view location, for example, we already revealed that, choosing a “normal” or “low” algorithm in a commercial Zygo SWLI, slope-dependent biases can depend on all these factors. RBT as a self calibration technique, it can also be applied to any surface profile measurement systems, such as deflectometry, to calibrate the slope dependent errors.

Overall, we developed a way for quantifying slope-dependent errors of optical profilometry. A calibrated error map can be used for compensating future low frequency form measurements, such as form measurements of microlenses with a similar slope range. Moreover, a slope-dependent error lookup curve can be used for compensating any continuous sloped surface measurement. In the meanwhile, an effective way for detection drift is proposed. Both of these can increase the accuracy of a profilometry measurement.

## REFERENCES

1. Hocken, R.J., N. Chakraborty, and C. Brown, *Optical metrology of surfaces*. Cirp Annals-Manufacturing Technology, 2005. **54**(2): p. 705-719.
2. Leach, R.K., *Optical measurement of surface topography*. 2011, Berlin: Springer.
3. Harasaki, A. and J.C. Wyant, - *Fringe modulation skewing effect in white-light vertical scanning interferometry*. Applied Optics, Vol. 39, Issue 13, pp. 2101-2106 (2000).
4. Gao, F., et al., *Surface measurement errors using commercial scanning white light interferometers*. Meas. Sci. Technol. 2008,19(1).
5. Mykura, H. and G.E. Rhead, *Errors in Surface Topography Measurements with High Aperture Interference Microscopes*. Journal of Scientific Instruments, 1963. **40**(6).
6. Dowell, M.B., C.A. Hultman, and G.M. Rosenblatt, *Determination of Slopes of Microscopic Surface Features by Nomarski Polarization Interferometry*. Review of Scientific Instruments, 1977. **48**(11): p. 1491-1497.
7. Gates, J.W., *Fringe Spacing in Interference Microscopes*. Journal of Scientific Instruments, 1956. **33**(12): p. 507-507.
8. Ingelstam, E., *Problems related to the accurate interpretation of microinterferograms*, in National Physical Laboratory Symposium No. 11 1960. p. 141 -163.
9. Schulz, G., *Über Interferenzen Gleicher Dicke Und Langenmessung Mit Lichtwellen*. Annalen Der Physik, 1954. **14**(3-5): p. 177-187.
10. Tolmon, F.R. and J.G. Wood, *Fringe Spacing in Interference Microscopes*. Journal of Scientific Instruments, 1956. **33**(6): p. 236-238.
11. Creath, K., *Calibration of Numerical Aperture Effects in Interferometric Microscope Objectives*. Applied Optics, 1989. **28**(16): p. 3333-3338.
12. Schulz, G. and K.E. Elssner, *Errors in Phase-Measurement Interferometry with High Numerical Apertures*. Applied Optics, 1991. **30**(31): p. 4500-4506.



13. Schmit, J., P. Unruh, and D.-S. Wan, *Fringe spacing in white-light interferometry*. Proc. SPIE 5531, Interferometry XII: Techniques and Analysis, 2004: p. 228-235.
14. Pfortner, A. and J. Schwider, *Dispersion error in white-light Linnik interferometers and its implications for evaluation procedures*. Applied Optics, 2001. **40**(34): p. 6223-6228.
15. Harasaki, A., J. Schmit, and J.C. Wyant, *Improved Vertical-Scanning Interferometry*. Appl. Opt., 2000. **39**(13): p. 2107-2115.
16. Lehmann, P., *Systematic effects in coherence peak and phase evaluation of signals obtained with a vertical scanning white-light Mirau interferometer*. Proceedings of SPIE, 2006(1): p. 618811.
17. Niehues, J., P. Lehmann, and K. Bobey, - *Dual-wavelength vertical scanning low-coherence interferometric microscope*. 2007. **46**(29).
18. Berger, R., T. Sure, and W. Osten, *Measurement errors of mirrorlike, tilted objects in white light interferometry*. Proceedings of SPIE, 2007(1): p. 66162E.
19. Ghim, Y.S. and A. Davies, *Complete fringe order determination in scanning white-light interferometry using a Fourier-based technique*. Applied Optics, Vol. 51, Issue 12, pp. 1922-1928 (2012).
20. Deck, L.L. and C. Evans, *High performance Fizeau and scanning white-light interferometers for mid-spatial frequency optical testing of free-form optics*. 2005: p. 59210A-59210A.
21. Olympus LEXT OLS4000 3D Confocal Laser Microscope Manual.
22. Leach, R.K., C.L. Giusca, and J.M. Coupland, *Advances in calibration methods for micro- and nanoscale surfaces*. Optical Micro- and Nanometrology Iv, 2012. 8430.
23. Mandal, R., et al., *Application of linear systems theory to characterize coherence scanning interferometry*. Optical Micro- and Nanometrology Iv, 2012. 8430.
24. de Groot, P. and X.C. de Lega, *Interpreting interferometric height measurements using the instrument transfer function*. Fringe 2005, 2006: p. 30-37.
25. Vorburger, T.V., et al., *Measurements of stylus radii*. Wear, 1979. **57**(1): p. 39-49.

26. R. E. Parks, C.J.Evans., L. Shao. *Calibration of interferometer transmission spheres*. in *Optical Fabrication and Measurement Workshop OSA Technical Digest Series*. 1998.
27. Gardner, N., *Precision geometric metrology of refractive micro-lenses*. Doctorate Dissertation, UNC Charlotte 2007.
28. Creath, K. and J.C. Wyant, *Absolute Measurement of Surface-Roughness*. *Applied Optics*, 1990. **29**(26): p. 3823-3827.
29. Whitehouse, D.J., *Surface metrology*. *Measurement Science & Technology*, 1997. **8**(9): p. 955-972.
30. Lehmann, P. *Optical versus tactile geometry measurement: alternatives or counterparts*. *Proc. SPIE 5144, Optical Measurement Systems for Industrial Inspection III*(2003).
31. Hansen, H.N., et al., *Dimensional Micro and Nano Metrology*. *CIRP Annals - Manufacturing Technology*, 2006. **55**(2): p. 721-743.
32. Savio, E., L. De Chiffre, and R. Schmitt, *Metrology of freeform shaped parts*. *CIRP Annals - Manufacturing Technology*, 2007. **56**(2): p. 810-835.
33. SPM tutorial: [http://virtual.itg.uiuc.edu/training/AFM\\_tutorial/](http://virtual.itg.uiuc.edu/training/AFM_tutorial/).
34. Faber, C., et al. *Deflectometry challenges interferometry: the competition gets tougher!* *Proc. SPIE 8493, Interferometry XVI: Techniques and Analysis*, 2012.
35. Osten, W. *Active metrology by digital holography*. *Proc. SPIE 4933, Speckle Metrology* 2003.
36. Schubert, M., et al., *Determination of the height of a microstructure sample by a SEM with a conventional and a digital photogrammetric method*. *Ultramicroscopy*, 1996. **63**(1): p. 57-64.
37. Reich, C., R. Ritter, and J. Thesing, *3-D shape measurement of complex objects by combining photogrammetry and fringe projection*. *Optical Engineering*, 2000. **39**(1): p. 224-231.
38. Knauer, M.C., J. Kaminski, and G. Hausler. *Phase measuring deflectometry: a new approach to measure specular free-form surfaces*. *Proceedings of the SPIE, Volume 5457*, pp. 366-376 (2004).

39. Evans, C.J., R.J. Hocken, and W.T. Estler, *Self-Calibration: Reversal, Redundancy, Error Separation, and 'Absolute Testing'*. CIRP Annals - Manufacturing Technology, 1996. **45**(2): p. 617-634.
40. Griesmann, U., *Three-flat test solutions based on simple mirror symmetry*. Applied Optics, 2006. **45**(23): p. 5856-5865.
41. ISO, *ISO 10110 Optics and photonics -- Preparation of drawings for optical elements and systems -- Part 8: Surface texture; roughness and waviness*, 2010. p. 19.
42. Deck, L.L. and C. Evans. *High performance Fizeau and scanning white-light interferometers for mid-spatial frequency optical testing of free-form optics*. Proc. SPIE 5921, Advances in Metrology for X-Ray and EUV Optics, 2005.
43. Jiang, X.J. and D.J. Whitehouse, *Technological shifts in surface metrology*. CIRP Annals - Manufacturing Technology, 2012. **61**(2): p. 815-836.
44. Youngworth, R.N., B.B. Gallagher, and B.L. Stamper. *An overview of power spectral density (PSD) calculations*. 2005.
45. He, L., C.J. Evans, and A. Davies, *Two-quadrant area structure function analysis for optical surface characterization*. Optics Express, 2012. **20**(21): p. 23275-23280.
46. He, L., C.J. Evans, and A. Davies, *Optical surface characterization with the area structure function*. CIRP Annals - Manufacturing Technology, 2013. **62**(1): p. 539-542.
47. Wikipedia, [http://en.wikipedia.org/wiki/White\\_light\\_interferometry](http://en.wikipedia.org/wiki/White_light_interferometry).
48. Chen, S., et al., *Digital Signal-Processing Techniques for Electronically Scanned Optical-Fiber White-Light Interferometry*. Applied Optics, 1992. **31**(28): p. 6003-6010.
49. Deck, L. and P. de Groot, *High-speed noncontact profiler based on scanning white-light interferometry*. Applied Optics, 1994. **33**(31): p. 7334-7338.
50. de Groot, P. and L. Deck, *Three-dimensional imaging by sub-Nyquist sampling of white-light interferograms*. Optics Letters, 1993. **18**(17): p. 1462-1464.

51. Sandoz, P., R. Devillers, and A. Plata, *Unambiguous profilometry by fringe-order identification in white-light phase-shifting interferometry*. Journal of Modern Optics, 1997. **44**(3): p. 519-534.
52. de Groot, P., *Method and apparatus for surface topography measurement by spatial-frequency analysis of interferograms*, Patent US5398113, 1995.
53. de Groot, P., et al., *Determination of Fringe Order in White-Light Interference Microscopy*. Applied Optics, 2002. **41**(22): p. 4571-4578.
54. Ghim, Y.-S. and A. Davies, *Complete fringe order determination in scanning white-light interferometry using a Fourier-based technique*. Applied Optics, 2012. **51**(12): p. 1922-1928.
55. Dresel, T., G. Häusler, and H. Venzke, *Three-dimensional sensing of rough surfaces by coherence radar*. Applied Optics, 1992. **31**(7): p. 919-925.
56. Zygo Newview 8000 SWLI manual.
57. Vorburger, T.V., et al., *Comparison of optical and stylus methods for measurement of surface texture*. The International Journal of Advanced Manufacturing Technology, 2007. **33**(1-2): p. 110-118.
58. Berger, R., T. Sure, and W. Osten. *Measurement errors of mirrorlike, tilted objects in white light interferometry*. Proc. SPIE 6616, Optical Measurement Systems for Industrial Inspection V, 2007.
59. Gao, F.C., J. M. Petzing, J., *V-groove measurement with white light interferometry*, in *Photon06: Manchester.2006*
60. Coupland, J.M. and J. Lobera, *Measurement of Steep Surfaces Using White Light Interferometry*. Strain, 2010. **46**(1): p. 69-78.
61. **Zhou, Y.**, et al., *Application of the random ball test for calibrating slope-dependent errors in profilometry measurements*. Applied Optics, 2013. **52**(24): p. 5925-5931.
62. Sheppard, C., D. Shotton, and C. Sheppard, *Confocal laser scanning microscopy*. 1997: BIOS Scientific Publishers Oxford.
63. Brakenhoff, G.J., P. Blom, and P. Barends, *Confocal scanning light microscopy with high aperture immersion lenses*. Journal of Microscopy, 1979. **117**(2): p. 219-232.

64. *Confocal Light Microscopy*. Annals of the New York Academy of Sciences, 1986. **483**(1 Recent Advanc): p. 416.
65. Griesmann, U., Q. Wang, J. Soons and R. Carakos. *A simple ball averager for reference sphere calibrations*. Proc. SPIE 5869, Optical Manufacturing and Testing VI, 2005.
66. Gardner, N. and A. Davies, *Self-calibration for microrefractive lens measurements*. Optical Engineering, 2006. **45**(3): p. 033603-033603-5.
67. Available from: [http://en.wikipedia.org/wiki/Euler\\_angles](http://en.wikipedia.org/wiki/Euler_angles).
68. Forbs, A.B., *Robust circle and sphere fitting by least squares*, in National Physics Laboratory technical report, 1989.
69. Griesmann, U., et al., *Measuring Form and Radius of Spheres with Interferometry*. CIRP Annals - Manufacturing Technology, 2004. **53**(1): p. 451-454.
70. Hecht, E., *Optics*. 2002: Wesley.
71. Olympus microscopy resource center, Available from: <http://www.olympusmicro.com/primer/lightandcolor/opticalaberrations.html>.
72. Mandal, R., K. Palodhi, J. Coupland, R. Leach and D. Mansfield. *Application of linear systems theory to characterize coherence scanning interferometry*. Proc. SPIE 8430, Optical Micro- and Nanometrology IV, 2012.
73. Coupland, J., R. Mandal, K. Palodhi, and R. Leach, *Coherence scanning interferometry: linear theory of surface measurement*. Applied Optics, 2013. **52**(16): p. 3662-3670.
74. Leach, R.K., C.L. Giusca, and K. Naoi, *Development and characterization of a new instrument for the traceable measurement of areal surface texture*. Measurement Science & Technology, 2009. **20**(12).
75. Weng, J.Y., P. Cohen, and M. Herniou, *Camera Calibration with Distortion Models and Accuracy Evaluation*. Ieee Transactions on Pattern Analysis and Machine Intelligence, 1992. **14**(10): p. 965-980.
76. Lili Ma, Y.C., Kevin L. Moore, *A Family of Simplified Geometric Distortion Models for Camera Calibration*, 2003.

77. Ricolfe-Viala, C. and A.J. Sanchez-Salmeron, *Lens distortion models evaluation*. Applied Optics, 2010. **49**(30): p. 5914-5928.
78. Adler, J. and S.N. Pagakis, *Reducing image distortions due to temperature-related microscope stage drift*. Journal of Microscopy-Oxford, 2003. **210**: p. 131-137.
79. Zhou, P. and J.H. Burge. *Limits for interferometer calibration using the random ball test*. Proc. SPIE 7426, Optical Manufacturing and Testing VIII, 2009.
80. Evans, C.J., M. Küchel, and C.A. Zanoni, *Apparatus and method for calibrating an interferometer using a selectively rotatable sphere*, Patent US6816267, 2004.
81. NIST metrology toolbox. Available from: <http://emtoolbox.nist.gov/Elastic/Case3.asp>.
82. Philip R. Bevington, D.K.R., *Data Reduction and Error Analysis for the Physical Sciences*. 2003: McGraw-Hill.
83. Lee, S.H., et al., *Using fixed fiduciary markers for stage drift correction*. Optics Express, 2012. **20**(11): p. 12177-12183.
84. Gelles, J., B.J. Schnapp, and M.P. Sheetz, *Tracking kinesin-driven movements with nanometre-scale precision*. Nature, 1988. **331**(6155): p. 450-453.
85. Betzig, E., et al., *Imaging Intracellular Fluorescent Proteins at Nanometer Resolution*. Science, 2006. **313**(5793): p. 1642-1645.
86. Dangaria, J.H., S. Yang, and P.J. Butler, *Improved nanometer-scale particle tracking in optical microscopy using microfabricated fiduciary posts*. Biotechniques, 2007. **42**(4).
87. Carter, A.R., et al., *Stabilization of an optical microscope to 0.1 nm in three dimensions*. Applied Optics, 2007. **46**(3): p. 421-427.
88. **Zhou, Y.**, A.P. Fard, and A. Davies, *Characterization of instrument drift using a spherical artifact*. Precision Engineering, 2014. **38**(2): p. 443-447.
89. Kreft, M., et al., *Lateral drift correction in time-laps images by the particle-tracking algorithm*. European Biophysics Journal with Biophysics Letters, 2008. **37**(7): p. 1119-1125.
90. Zygo Newview 5000 SWLI manual

## APPENDIX A: MATLAB CODE FOR RBT SIMULATION

```

tic
clc;
clear all;

% Define constants
sg = 101; % number of pixel in X or Y of cap
rr = 100; % times of RBT
nn = 100; % times of rotations (caps)
M = 0; % Multiplier for ball error control
R = 0.595; % Base radius of the ball(mm)

% define a perfect cap with grid (50X FoV: 0.256x0.256 mm)
delta = 0.256/(sg-1);
x = -0.128 + offset_x : delta : 0.128 + offset_x;
y = -0.128 + offset_y : delta : 0.128 + offset_y;
[X,Y] = meshgrid(x,y);
rho = zeros(size(X))+ R;
Z = sqrt(rho.^2 - X.^2 - Y.^2);

% Ball's position
offset_x = 0;
offset_y = 0;

% spherical harmonic functions coefficients for generating a realistic
ball
degree1 = 3;
order1 = 1;
degree2 = 4;
order2 = 3;
degree3 = 6;
order3 = 1;
degree4 = 1;
order4 = 1;
degree5 = 2;
order5 = 1;

for mm = 1:rr %outer loop for "rr" RBTs
for k = 1:nn %inner loop for one RBT with "nn" measurements

alpha = rand*2*pi; % rotation angle of the cap along x axis
beta = rand*pi; % rotation angle of the cap along y axis
gamma =rand*2*pi; % rotation angle of the cap along z axis

a = [cos(alpha)*cos(beta)*cos(gamma)-sin(alpha)*sin(gamma) -
cos(alpha)*cos(beta)*sin(gamma)-sin(alpha)*sin(gamma)
cos(alpha)*sin(beta);sin(alpha)*cos(beta)*cos(gamma)+cos(alpha)*sin(gam
ma) -sin(alpha)*cos(beta)*sin(gamma)+cos(alpha)*cos(gamma)
sin(alpha)*sin(beta); -sin(beta)*cos(gamma) sin(beta)*sin(gamma)
cos(beta)]; % Rotation matrix.

% new coordinates for the cap.
X1 = a(1,1).*X + a(1,2).*Y + a(1,3).*Z;

```

```

Y1 = a(2,1).*X + a(2,2).*Y + a(2,3).*Z;
Z1 = a(3,1).*X + a(3,2).*Y + a(3,3).*Z;

%   figure(1),surf(X1,Y1,Z1),axis([-2 2 -2 2 -2 2])

% Coordinate transformation: find out each pixel's corresponding
theta and phi range after rotation
cos_theta = Z1./rho;

X11 = reshape(X1,sg*sg,1);
Y11 = reshape(Y1,sg*sg,1);
oo = length(X11);

for i = 1:oo
if (X11(i) > 0) & (Y11(i) >= 0);
    phi = atan(Y11(i)./X11(i));
elseif (X11(i) <= 0) & (Y11(i) > 0);
    phi = atan(Y11(i)./X11(i))+pi;
elseif (X11(i)<0) & (Y11(i)<=0);
    phi = atan(Y11(i)./X11(i))+pi;
elseif (X11(i)>=0) & (Y11(i)<0);
    phi = atan(Y11(i)./X11(i))+2*pi;
elseif (X11(i)==0) & (Y11(i)==0);
    phi = 3*pi;
end,phil(i)=phi;
end
phil = reshape(phil,sg,sg);
peak = find(phil==3*pi);

% save each cap's angular information
cos_thetan(:, :, k, mm)=cos_theta;
phin(:, :, k)=phil(:, :);

% use different sphericial harmonics to generate ball error
Ymn1 = legendre(degree1,cos_theta);
yy1 = squeeze(Ymn1(order1+1, :, :));
yy_1 = (-1).^order1*(factorial(degree1-
order1)./factorial(degree1+order1))*yy1; % order = -m
yy1 = yy1.*cos(order1*phil);
yy1(peak)=0;
yy_1 = yy_1.*cos(-1.*order1*phil);
norm1 = max(max(abs(yy1)));

Ymn2 = legendre(degree2,cos_theta);
yy2 = squeeze(Ymn2(order2+1, :, :));
yy_2 = (-1).^order2*(factorial(degree2-
order2)./factorial(degree2+order2))*yy2;
yy2 = yy2.*cos(order2*phil);
yy2(peak)=0;
yy_2 = yy_2.*cos(-1.*order2*phil);
norm2 = max(max(abs(yy2)));

Ymn3 = legendre(degree3,cos_theta);
yy3 = squeeze(Ymn3(order3+1, :, :));
yy_3 = (-1).^order3*(factorial(degree3-
```



```

order3)./factorial(degree3+order3))*yy3;
yy3 = yy3.*cos(order3*phi1);
yy3(peak)=0;
yy_3 = yy_3.*cos(-1.*order3*phi1);
norm3 = max(max(abs(yy3)));

Ymn4 = legendre(degree4,cos_theta);
yy4 = squeeze(Ymn4(order4+1, :, :));
yy_4 = (-1).^order4*(factorial(degree4-
order4)./factorial(degree4+order4))*yy4;
yy4 = yy4.*cos(order4*phi1);
yy4(peak)=0;
yy_4 = yy_4.*cos(-1.*order4*phi1);
norm4 = max(max(abs(yy4)));

Ymn5 = legendre(degree5,cos_theta);
yy5 = squeeze(Ymn5(order5+1, :, :));
yy_5 = (-1).^order5*(factorial(degree5-
order5)./factorial(degree5+order5))*yy5;
yy5 = yy5.*cos(order5*phi1);
yy5(peak)=0;
yy_5 = yy_5.*cos(-1.*order5*phi1);
norm5 = max(max(abs(yy5)));

yy=(yy1+0.05*yy2+0.2*yy3+2.5*yy4+(-0.5)*yy5+0.05*yy6+(-
0.1)*yy7+0.0005*yy8+0.1*yy9+yy10); % ball error generated by the
combination of a set of low order SHs.

rho1 = R+ M*yy; % realistic rho value for each point of a ball.

%%%%%%%%%%%%%%%%%%%%%%%%%%%%%%%%%%%%%%%%%%%%%%%%%%%%%%%%%%%%%%%%%%%%%%%%add distortion effect into RBT%%%%%%%%%%%%%%%%%%%%%%%%%%%%%%%%%%%%%%%%%%%%%%%%%%%%%%%%%%%%%%%%%%%%%%%%
Z11 = sqrt(rho1.^2 - (r+0.0596*r.^3).^2);%centered position with
lpixel distortion

%%%%%%%%%%%%%%%%%%%%%%%%%%%%%%%%%%%%%%%%%%%%%%%%%%%%%%%%%%%%%%%%%%%%%%%%add stage drift into RBT%%%%%%%%%%%%%%%%%%%%%%%%%%%%%%%%%%%%%%%%%%%%%%%%%%%%%%%%%%%%%%%%%%%%%%%%
Z11 = sqrt(rho1.^2 - (X+0.00007562.*k).^2-(Y-
0.00005436.*k).^2); %center posion drift model for confocal 50x

%%%%%%%%%%%%%%%%%%%%%%%%%%%%%%%%%%%%%%%%%%%%%%%%%%%%%%%%%%%%%%%%%%%%%%%%

%%%%%%%%%%%%%%%%%%%%%%%%%%%%%%%%%%%%%%%%%%%%%%%%%%%%%%%%%%%%%%%%%%%%%%%%add misalignment into RBT %%%%%%%%%%%%%%%%%%%%%%%%%%%%%%%%%%%%%%%%%%%%%%%%%%%%%%%%%%%%%%%%%%%%%%%%%
Z11 = sqrt(rho1.^2 - (X+normrnd(0,deltax)).^2 -
(Y+normrnd(0,deltay)).^2)+normrnd(0,deltaz);
%%%%%%%%%%%%%%%%%%%%%%%%%%%%%%%%%%%%%%%%%%%%%%%%%%%%%%%%%%%%%%%%%%%%%%%%

Z0 = sqrt(R.^2-(X).^2-(Y).^2); %base sphere

%Calculate slope magnitude
for i=1:sg-1
for j=1:sg-1
deltaz1 = abs((Z11(i,j+1)-Z11(i,j)));
deltaz2 = abs((Z11(i+1,j)-Z11(i,j)));
x_spacing = 0.256./(sg-1);
y_spacing = 0.256./(sg-1);

```

```

slopeX(i,j) = atan(deltaz1./x_spacing).*180./pi;
slopeY(i,j) = atan(deltaz2./y_spacing).*180./pi;
slope(i,j) = sqrt(slopeX(i,j)^2+slopeY(i,j)^2);
end
end

Zn(:,:,k,mm)=Z11; % save all z values of caps during RBT
rhon(:,:,k,mm) = rho1;

end

X_avg = X;
Y_avg = Y;
Z_avg = squeeze(mean(Zn,3));
rho_avg = squeeze(mean(rhon,3));

%%%%%%%%%%%%%%%%%%%%%%%%%%%%%%%%%%%%%%%%%%%%%%%%%%%%%%%%%%%%%%%%%%%%%%%%%find best fit sphere of RBT %%%%%%%%%%%%%%
% find best fit plane
i = find(~isnan(X));
% i = find(Z_avg>0);
xx = X(i);
yy = Y(i);
zz = Z_avg(i);

fit=[xx yy ones(size(xx))];
A=fit\zz; % coefficients of the best fit plane

bestfit=ones(size(X));
bestfit=X.*A(1)+Y.*A(2)+bestfit.*A(3); % generate best fit plane

Bo = A(1,1);
Co = A(2,1);
Eo = A(3,1);
Do = 1;

% find approximate centroid (xo,yo,zo)
XO = meshgrid(X,sg*sg,1);
YO = meshgrid(Y,sg*sg,1);
Z_avgo = meshgrid(Z_avg(:,:,mm),sg*sg,1);
xo = mean(XO);
yo = mean(YO);
zo = mean(Z_avgo);

xp2 = XO - xo;
yp2 = YO - yo;
zp2 = Z_avgo - zo;

% rotate the plane so that it is parallel to X-Y plane
Xrotate = atan(Co);
Yrotate = atan(Bo);

```

```

% rotate about x-axis
yp3 = yp2.*cos(Xrotate) - zp2.*sin(Xrotate);
zp3 = yp2.*sin(Xrotate) + zp2.*cos(Xrotate);

% rotate about y-axis
xp3 = xp2.*cos(Yrotate) - zp3.*sin(Yrotate);
zp3 = xp2.*sin(Yrotate) + zp3.*cos(Yrotate);

% define O and Z matrix
O = zeros(length(xp3),4);
ZZ = zeros(length(xp3),4);

O(:,1) = xp3'.^2 + yp3'.^2 + zp3'.^2;
O(:,2) = xp3';
O(:,3) = yp3';
O(:,4) = ones(size(xp3'));
ZZ(:,1) = zp3';

ABCE = O\ -ZZ;

% rotation matrix
U = [cos(Yrotate) -sin(Xrotate).*sin(Yrotate) -
cos(Xrotate).*sin(Yrotate);0 cos(Xrotate) sin(Xrotate);sin(Yrotate)
sin(Xrotate).*cos(Yrotate) cos(Xrotate).*cos(Yrotate)];
Parameters = U'*[ABCE(2);ABCE(3);1];

% solve parameters
A = ABCE(1);
Bo = Parameters(1);
Co = Parameters(2);
Do = Parameters(3);
E = ABCE(4);

B = Bo - 2.*A.*xo;
C = Co - 2.*A.*yo;
D = Do - 2.*A.*zo;
E = A.*(xo.^2+yo.^2+zo.^2)-Bo.*xo - Co.*yo -Do.*zo +E;

Xo = -B./(2*A);
Yo = -C./(2*A);
Zo = -D./(2*A);
Ro = ((B.^2+C.^2+D.^2-4*A*E).^0.5)./(2*abs(A));

center = [Xo;Yo;Zo;Ro]; % best fit center

R1(mm,1)=center(4);
Z_bestfit = sqrt(center(4).^2-(X-center(1)).^2-(Y-
center(2)).^2)+center(3);

end

Z00 = sqrt(R.^2-(X-center(1)).^2-(Y-center(2)).^2); % base sphere
syserror(:, :, mm) = Z_avg(:, :, mm) - Z00; % error map
figure(2), surf(X,Y,syserror), axis equal

```

```
colorbar('fontsize',12);set(gca,'fontsize',12);  
xlabel('X(mm)','fontsize',12,'fontweight','b'),ylabel('Y(mm)','font  
size',12,'fontweight','b'),title('<math>W_i</math> - Base sphere  
(mm)','fontsize',12,'fontweight','b')
```

toc

## APPENDIX B: MATLAB CODE FOR DATA PROCESSING OF RBT CALIBRATION

```

clc;
clear all;

a=importdata('a.mat'); % import <wi>: average of RBT
[X,Y]=meshgrid(1:1:639,1:1:480);% define a grid of cap
X=X.*0.00022375; % pixel size is 0.00022375mm for SWLI 50x
Y=Y.*0.00022375;

a = a(:,2:640);
a = a./1000; % unit: um to mm
deltaX = 0; % displacement of ball center on X direction,mm

% remove tilt
j = find(~isnan(a));
xx = X(j);
yy = Y(j);
zz = a(j);

fit=[xx yy ones(size(xx))];
A=fit\zz; % coefficients of the best fit plane

Bo = A(1,1);
Co = A(2,1);
Eo = A(3,1);
Do = 1;

% find approximate centroid (xo,yo,zo)
X0 = meshgrid(xx,length(j),1);
Y0 = meshgrid(yy,length(j),1);
Z_avgo = meshgrid(zz,length(j),1);
xo = mean(X0);
yo = mean(Y0);
zo = mean(Z_avgo);

xp2 = X0 - xo;
yp2 = Y0 - yo;
zp2 = Z_avgo - zo;

% rotate the plane so that it is parallel to X-Y plane
Xrotate = atan(Co);
Yrotate = atan(Bo);

% rotate about x-axis
yp3 = yp2.*cos(Xrotate) - zp2.*sin(Xrotate);
zp3 = yp2.*sin(Xrotate) + zp2.*cos(Xrotate);

% rotate about y-axis
xp3 = xp2.*cos(Yrotate) - zp3.*sin(Yrotate);
zp3 = xp2.*sin(Yrotate) + zp3.*cos(Yrotate);

% define O and Z matrix

```

```

O = zeros(length(xp3),4);
ZZ = zeros(length(xp3),4);

O(:,1) = xp3'.^2 + yp3'.^2 + zp3'.^2;
O(:,2) = xp3';
O(:,3) = yp3';
O(:,4) = ones(size(xp3'));
ZZ(:,1) = zp3';

ABCE = O\ -ZZ;

% rotation matrix
U = [cos(Yrotate) -sin(Xrotate).*sin(Yrotate) -
cos(Xrotate).*sin(Yrotate);0 cos(Xrotate) sin(Xrotate);sin(Yrotate)
sin(Xrotate).*cos(Yrotate) cos(Xrotate).*cos(Yrotate)];
Parameters = U'*[ABCE(2);ABCE(3);1];

% solve parameters
A = ABCE(1);
Bo = Parameters(1);
Co = Parameters(2);
Do = Parameters(3);
E = ABCE(4);

B = Bo - 2.*A.*xo;
C = Co - 2.*A.*yo;
D = Do - 2.*A.*zo;
E = A.*(xo.^2+yo.^2+zo.^2)-Bo.*xo - Co.*yo -Do.*zo +E;

Xo = -B./(2*A);
Yo = -C./(2*A);
Zo = -D./(2*A);
Ro = ((B.^2+C.^2+D.^2-4*A*E).^0.5)./(2*abs(A));

center = [Xo;Yo;Zo;Ro];

Z0 = sqrt(0.595.^2-(X-center(1)).^2-(Y-
center(2)).^2)+center(3); %base sphere

for i=1:479
    for j=1:638
        deltaz1 = abs((Z0(i,j+1)-Z0(i,j))).*1000;
        deltaz2 = abs((Z0(i+1,j)-Z0(i,j))).*1000;
        deltax = 0.22375;
        deltay = 0.22375;

        slopeX(i,j) = atan(deltaz1./deltax).*180./pi;
        slopeY(i,j) = atan(deltaz2./deltay).*180./pi;
        slope(i,j) = sqrt(slopeX(i,j)^2+slopeY(i,j)^2);

        deltaz11 = abs((a(i,j+1)-a(i,j))).*1000;
        deltaz22 = abs((a(i+1,j)-a(i,j))).*1000;

        slopeXX(i,j) = atan(deltaz11./deltax).*180./pi;

```

```
slopeYY(i,j) = atan(deltaz22./deltay).*180./pi;  
slope1(i,j) = sqrt(slopeXX(i,j)^2+slopeYY(i,j)^2);  
  
end  
  
end  
  
% error map: remove offset at slope = 0  
Instrument_error = ((a-Z0)-(center(4)-0.595))*1000;
```